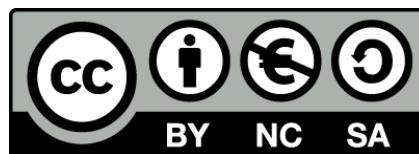




UNIVERSITAT DE
BARCELONA

Development of a Nano-Illumination Microscope

Nil Franch Masdeu



Aquesta tesi doctoral està subjecta a la llicència **Reconeixement- NoComercial – Compartir Igual 4.0. Espanya de Creative Commons.**

Esta tesis doctoral está sujeta a la licencia **Reconocimiento - NoComercial – Compartir Igual 4.0. España de Creative Commons.**

This doctoral thesis is licensed under the **Creative Commons Attribution-NonCommercial-ShareAlike 4.0. Spain License.**

Development of a Nano-Illumination Microscope

Nil Franch Masdeu



UNIVERSITAT DE
BARCELONA



UNIVERSITAT DE
BARCELONA

Development of a Nano-Illumination Microscope

Programa de Doctorat en Enginyeria i Ciències Aplicades

Departament d'Enginyeria Electrònica i Biomèdica

Barcelona, Març 2022

Autor:
Nil Franch Masdeu

Director i Tutor:
Dr. Ángel Diéguez Barrientos

Acknowledgements

I want to begin by thanking Dr. Ángel Diéguez for his supervision and inspiration in working towards completing this thesis during all these years, as well as by the opportunity to do creative work in a laboratory or designing chips. His guidance made it possible to be a part of inventing a new microscope and then putting it into these pages.

These pages wouldn't be here without the efforts made by Dr. Joan Canals: his contributions and experience are everywhere in the project and his expertise has been a lifesaver many times, as well as a source of learning.

Victor Moro and Sergio Moreno are part of this project as well, and their contributions to the chips, to the driving circuits and in the long and difficult experiments with the different setups have been vital for this thesis: thank you!

I want to thank the entire family in the lab: Dr. Oscar Alonso was always there to offer his experience for help. Juan Luís, Silvina and the rest too, for sharing their knowledge and time.

I am deeply grateful to the entirety of the Electronics department for their support, but I want to mention Dr. Anna Vilà for her help in the cleanroom and for revising the papers.

I want to extend my gratitude to Dr. Mauricio Moreno for his help with the cleanroom. Thanks also to Dr. Julià López, Dr. Sergi Hernández and Dr. Blas Garrido for their time and for letting us use their electro-optical bench to characterize the SPADs. Special thanks also for Dr. Albert Romano-Rodríguez for using his EBL machine to fabricate the test patterns.

Thanks also to the staff at the prototyping lab, specially Andres Romero who made the bondings in all the chips.

My gratitude goes also for everyone involved in the ChipScope European project: it has been quite an inspiring experience to work with such great professionals of different fields to push into creating the new microscope presented here.

Last but not least, none of this would have been possible without my life partner Mireia. She has always been there, supporting me, helping me through problems that sometimes had me absolutely absorbed. My friends have also been there with that support, in many different forms and occasions these strange times! I couldn't forget about my family, always there offering their care: thanks for it, and for always nurturing my curiosity!

Barcelona, February 2022

Contents

List of Figures	ix
List of Tables	xi
Acronyms	xiii
1 Introduction to Microscopy	1
1.1 A short story of optics	2
1.1.1 The resolving power of the microscope	4
1.2 Microscopy techniques	9
1.2.1 Optical Microscopy	9
1.2.2 Electron Microscopy	12
1.2.3 Scanning Probe Microscopy	13
1.2.4 Optical Super-resolution Microscopy	14
1.2.5 Lensless Microscopy	18
1.3 Thesis motivation	21
1.4 Conclusions	23
References	24
2 Components of the Nano Illumination Microscope	31
2.1 Introduction	31
2.2 SPAD sensors	32
2.2.1 Figures of merit of SPADs	35
2.3 SPAD camera design	38
2.3.1 Design overview	38
2.3.2 SPAD and readout circuit design	42
2.3.3 Matrix structure	45
2.3.4 Counter Matrix	46
2.3.5 Internal control signal generation	47
2.4 Camera Characterization	48
2.4.1 Dark count rate	49
2.4.2 Photon Detection Probability	49
2.4.3 Afterpulsing	51
2.4.4 SPAD response calibration	52
2.5 LED arrays	53
2.5.1 Introduction to display technologies	53
2.5.2 Towards nanoLEDs arrays for NIM microscopy	56

2.6	Conclusions.	60
	References	62
3	Nano Illumination Microscopy	71
3.1	Introduction	71
3.2	NIM Operation principle	71
3.2.1	Operation of the microscope	72
3.3	NIM design guidelines	76
3.4	Setup overview	79
3.4.1	FPGA based system controller	79
3.4.2	Software	82
3.5	The first microscope prototype	85
3.5.1	Design	85
3.6	Results of the first prototype	90
3.6.1	Results.	91
3.7	Conclusions.	94
	References	94
4	Pursuing the Limits of NIM with LED arrays	97
4.1	Reducing the light beam	98
4.1.1	Setup for light spot downscaling	98
4.1.2	Measurements	100
4.2	Reducing the size of the LEDs	105
4.2.1	Microscope Setup	106
4.2.2	Measurements	115
4.3	Light spot shape	115
4.4	Discussion of super-resolution capabilities	119
4.5	Conclusions.	121
	References	122
5	Conclusions and Future outlook of the NIM technique	125
5.1	Conclusions.	125
5.2	Microscope improvements	128
5.2.1	Applications.	129
	References	130
A	Resum	131
A.1	Introducció a la Microscopia	131
A.2	Components del Microscopi de Nano Il·luminació	135
A.3	Microscopia de Nano Il·luminació	138
A.4	Perseguint els límits de la MNI amb matrius de LEDs	144
A.5	Conclusions.	148

B List of Publications	151
Publications	151
Conferences	153

List of Figures

1.1	Human eye	2
1.2	Abbe's explanation of image formation	6
1.3	Rayleigh's resolving criterion	7
1.4	EM spectrum and observable objects	8
1.5	Fluorescence phenomenon	11
1.6	STED PSFs	16
1.7	Lensless microscope	20
1.8	Schematic of the basic NIM distribution	21
2.1	Schematic of the basic NIM distribution	32
2.2	Usage of a SPAD array for sample localization	34
2.3	Schematic of the structure of a SPAD and operation region	35
2.4	Schematics of active and passive quenching circuits	36
2.5	Photography of the SPAD camera chip	39
2.6	Schematic of the SPAD camera architecture	41
2.7	Timing diagrams of the control signals of the camera	42
2.8	Waveforms of the SPAD control signals	43
2.9	Schematic of the SPAD, control and readout circuits	45
2.10	Layout and picture of the SPAD and readout	46
2.11	Schematic of a camera row	46
2.12	Schematic of RST signal generator	47
2.13	Experimental setup for the characterisation of the SPAD camera	49
2.14	Dark count rate statistical distribution	50
2.15	Dark count rate distribution	50
2.16	Photon Detection Probability and polymide effect	51
2.17	Afterpulsing as a function of TOFF	52
2.18	Calibration of the SPAD camera	53
2.19	Diagram of OLED layers	55
2.20	LED chips developed during Chipscope project	56
2.21	Matrix LED addressing	57
2.22	First Micro-LED array structure and fabrication	58
2.23	Picture of the realized 8×8 , $5 \mu\text{m}$ GaN LED chip.	59
2.24	SEM pictures of the advanced LED arrays	59
2.25	Angular radiant intensity distribution of microLEDs	60
2.26	Fast optical response of the LEDs	61

3.1	Operation principle of the NIM microscope	72
3.2	Results of microscope ray tracing simulations	73
3.3	Schematic of the shadow cone projected by an object smaller than the LEDs	74
3.4	Schematic showing the reason for the degradation of contrast with the distance between LEDs and sample	75
3.5	Contrast as a function of the distance between sample and sensor	76
3.6	General schematics of the NIM microscope	78
3.7	Schematic for obtaining the size of the detector	78
3.8	General schematics of the setup of the NIM microscopes	80
3.9	PCB level schematic of the architecture of the NIM system	80
3.10	Simplified block diagram of the System Controller Implemented in the SoC.	83
3.11	Algorithm for the construction of a NIM image	83
3.12	GUI interface for the microscope software	84
3.13	LED calibration process	85
3.14	Picture of the daughter PCB board	86
3.15	Picture of the definitive version of the first NIM microscope setup	87
3.16	3D-printed sample holders for the first prototype	88
3.17	Schematic of the direct addressing LED driver circuit	88
3.18	Picture of the implemented PCB with the LED driving circuit	89
3.19	Picture of the μ LEDs being driven	89
3.20	Pictures and drawings of the PCBs designed for testing the SPAD camera	90
3.21	Picture of the EBL test patterns	91
4.1	Light spot downscaling setup	98
4.2	Picture of the CMOS camera module and sensitivity	99
4.3	Images of the wing of a fly obtained with the light spot downscaling setup	102
4.4	Picture of human lung fibroblasts	102
4.5	NIM images of the 800 nm squares with the downscaling setup	103
4.6	Comparison of contrast on an object and its image	104
4.7	ESF measured on the EBL sample for different step distances and LSF from it	105
4.8	Picture of the 2×32 LED array of 200 nm designated LED2 chip	106
4.9	Schematic overview of the architecture of the new compact setup	107
4.10	DE0-Nano Board PCB and component diagram	108
4.11	Discrete driver schematic	109
4.12	Pictures of the top and bottom sides of the LED driver PCBs	109
4.13	Block diagram of the control firmware in the DE0-Nano FPGA	110
4.14	Capture of the GUI interface for the advanced microscope prototypes	112

4.15	200 nm LED Microscope setup	113
4.16	Comparison of sample observed with NIM or optical microscope . .	116
4.17	ESF and LSF at the region of interest of the 200 nm LED setup.	116
4.18	Schematic distribution of the 200 nm LED array simulations	117
4.19	Results of the simulation of the 200 nm LED array	118
4.20	Simulation of FWHM size beyond the LED array surface	119
4.21	Scheme of the near field electromagnetic simulations	120
4.22	Far-field light intensity escaping Al bar from dipole array	121
4.23	Contrast obtained by the different dipole models	122
5.1	Next generation NIM microscope	128
A.1	Esquema d'un microscopi sense lents	134
A.2	Esquemàtic de l'estructura bàsica d'un MNI	134
A.3	Fotografia i esquemàtic de la matriu SPADs	136
A.4	Xips de LEDs desenvolupats i emprats al llarg del projecte Chipscope	138
A.5	Microfotografia de les matrius de LEDs	139
A.6	Principi d'operació del microscopi	140
A.7	Esquema general dels components del MNI	140
A.8	Interfície gràfica d'usuari pel microscopi	141
A.9	Fotografia del primer microscopi de nano il·luminació	142
A.10	Muntatge de reducció de punt de llum	145
A.11	Imatges MNI de quadres de 800 nm amb reducció del punt de llum .	146
A.12	Muntatge per als LEDs de 200 nm	146
A.13	Comparativa entre mic. òptic i MNI amb LEDs de 200 nm	147

List of Tables

1.1	Comparison of SRM techniques	19
2.1	I/O table for the SPAD camera chip	40
3.1	First prototype NIM image results	92
4.1	Main microscope control functionalities implemented.	111
4.2	Overview of the microscope components	113
A.1	Comparació de tècniques de microscopia de super-resolució	133
A.2	Resultats del primer microscopi	142

Acronyms

AXI	Advanced eXtensible Interface
CCD	Charge-Coupled Device
CMOS	Complementary Metal-Oxide Semiconductor
DAC	Digital to Analog Converter
DCR	Dark Count Rate
DPI	Dots Per Inch
EBL	Electron Beam Lithography
EMCCD	Electron Multiplying Charge-Coupled Device
ESF	Edge Spread Function
FOV	Field Of View
FPGA	Field Programmable Gate Array
FWHM	Full Width at Half Maximum
GUI	Graphical User Interface
IC	Integrated Circuit
LCD	Liquid Crystal Display
LDO	Linear Dropout Regulator
LED	Light Emitting Diode
LSF	Line Spread Function
LUT	Look-Up Table
MTF	Modulation Transfer Function
NIM	Nano Illumination Microscopy
PCB	Printed Circuit Board
PDP	Photon Detection Probability
PSF	Point Spread Function
PMT	Photon Multiplying Tube
PWM	Pulse Width Modulation
sCMOS	scientific CMOS
SEM	Scanning Electron Microscopy
SoC	System on Chip
SNR	Signal-Noise Ratio
SPAD	Single Photon Avalanche Diode
TCSPC	Time Correlated Single Photon Counting
TDC	Time to Digital Converter
TEM	Transmission Electron Microscopy

1

Introduction to Microscopy

While there were photonic detectors in living beings before, the development of organs capable of focusing light into images during the Cambrian period supposed a revolution, to the point that today, 95% of all multicellular animals have eyes. The sense of sight started an arms race which produced plenty of adaptations: since it began, prey animals had to develop either camouflage or shells to protect themselves [1]. In the case of humans, no other sense comes close to eyesight. It is the sense upon which we built the modern cultures and the one used to read and share knowledge with others.

The human eye is sensitive to electromagnetic radiation with wavelengths between 400 and 700 nm. The brain interprets the information on the wavelength of the detected light to create the perception of colours accordingly. Visible light, though, represents a small part of the electromagnetic spectrum, which goes from radio waves with wavelengths of thousands of kilometres to gamma rays, that have wavelengths of 10^{-12} m. The evolution of the eye selected that range of sensibility because the wavelengths corresponding to visible light reach Earth's surface with more energy coming from the Sun.

The energy of electromagnetic radiation is contained in discrete units of quanta called photons that have the properties of both particles and waves. This duality is vital in microscopy, being used for example in electronic microscopy by propagating electrons instead of light to study the sample or in fluorescence microscopy.

The eye, as can be seen in figure 1.1, evolved to capture and focus light in the visible range. It is full of a fluid with a refractive index (n) higher than that of air (1.34 vs 1), the vitreous humor. An additional lens evolved inside the eye, behind the cornea, to focus on objects at different distances. This lens, full of aqueous humor with a different refractive index than that of the eye, can be thinned or expanded by the musculature connected to it to provide the focusing capabilities. The system acts as a composite lens and creates a real image on the retina, the back part of the

eye, which contains the receptor cells sensitive to light.

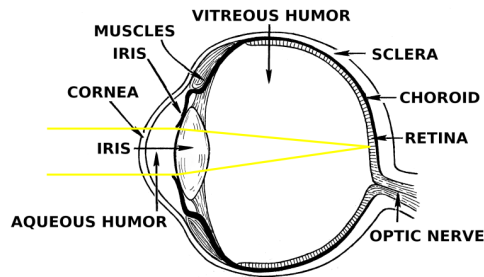


Figure 1.1: Drawing of the human eye, showing image formation in it: the cornea and lens act as a converging lens system that projects the image onto the retina.

While eyesight is the sense we use more prominently to explore the natural world, it is evident it presents limitations, such as being unable to distinguish objects far away or small below certain limits. These limitations motivated the development of tools to help go over those limits, such as telescopes or optical microscopes. The idea behind both is to provide augmentation so that the eye can perceive the objects under scrutiny. The difference between both, though, is that the telescope is prepared to work with objects situated away, while the microscope forms the image from samples nearby but smaller than the natural limitation of the naked eye to resolve them.

1.1. A short story of optics

The science of optics began far in the past by studying the nature of light and how it propagated. This latter aspect was specially studied and developed by Ancient Greek scientists, which proposed a set of geometrical laws for it, initiating the field of geometrical optics. Euclides, in his treatise *Catoptrics* (year 280 BC), proposed that light travelled in straight lines in homogeneous media. This work also included the correct formulation for the law of reflection. Two hundred years later, Hero of Alexandria further developed this work in a treatise also named *Catoptrics*. He offered a geometrical derivation of the law of reflection by theorising that light rays always travel between two points in space using the shortest path possible. A bit before Hero's work, Claudius Ptolemy studied the propagation of light through different mediums, making observations on how the light changed its path on interfaces between air and water or glass, and tabulated the observed values. This allowed him to formulate a first approximation to the law of refraction, which, while very imprecise, remained the only one available until 1500 years later Willebrord Snellius formulated currently used law with his name [2, 3].

After the fall of the Roman empire, it was in the Islamic world where several scientists did the job of recovering and compiling Greek optical theories. For example,

Ibn Sahl formulated an improved law for refraction [4], and Ibn al-Haytham (965 - 1040) is considered the father of modern optics due to his extensive works on the subject, which greatly influenced later Western European authors. He discarded the Greek theory that light originated in the eye and provided plenty of experimentation on lenses, mirrors, refraction and reflection, as well as experimenting with pinhole cameras and image formation [5, 6].

While in the late 13th century Italian glassworkers were fabricating lenses for correcting poor eyesight, such work attracted no scientific interest [2, 3, 7], probably because further development of optical theory required mathematics to advance as well. It was not until Johannes Kepler (1571–1630) realised optics would be crucial for astronomy and began to work in the field that it saw new advances. In his manuscript *Astronomiae Pars Optica* (year 1604), he described the inverse-square law for light propagating from a source, reflection on flat or curved mirrors, and the principles behind pinhole cameras. This document was considered the foundation of modern optics, but it did not include any study on refraction. It was not until the year the 1620s that both Snellius and Descartes independently discovered the mathematical law for it. Meanwhile, Kepler used the classical Greek approximation, valid only for small angles of incidence. Despite that, he produced a theoretical explanation of how lenses operated within the telescopes used at his time.

The first refracting telescopes appeared in the Netherlands in the early 17th century, being of common usage and without a known inventor. Microscopes similarly appeared a bit later during the same century. Galileo Galilei actually realised the importance of those devices and vastly improved both, proposing his telescope in 1609 and his compound microscope in 1625.

Newton (1643-1727) contributed greatly by developing plenty of experimental methodologies, through which he finally proposed a theory on the colours of light. He realised that the colour observed in objects results from their interaction with already coloured light. From this work, he predicted that optical instruments based on refraction would suffer from chromatic aberration and invented the reflection telescope to avoid the problem. Newton ground his own mirrors for the experiments, developing their fabrication. This, for example, allowed him to obtain huge mirrors to use for his telescope, which meant it was better than the refraction based ones of his time. Newton proposed that light consisted of tiny particles, explaining refraction as an attraction from the denser material. This required light particles to move faster in the denser material.

Grimaldi (1605) had observed the 'breaking' of light in diffraction patterns. While Newton tried to describe the phenomenon within his theory, calling it inflection, he failed to produce a proper theory for it. Instead, Hooke (1665) and later Huygens in his work *Traité de la lumière* (1690) proposed a wave theory for light, becoming the first mathematical theory for it. However, this wave theory had to compete with Newton's corpuscular one, and since it failed to describe phenomena such as birefringence, it was not widely accepted.

The corpuscular theory of light stood for a whole century until Young (1803) observed the pattern of light produced when illuminating two closely spaced slits. He went on to study various interference phenomena, describing it as the cancellation or addition of the amplitudes of waves. This also allowed him to estimate the light wavelength, approximating the correct and different values for red and blue light. Young also studied vision, showing that focusing depended on changes in the shape of the eye and its lens, and even suggested that the eye contains a discrete number of light-sensitive elements, which responded only to three colours: red, green and blue-violet.

Fresnel further developed in 1821 the mathematical description of the wave theory for light and did additional experiments on diffraction. He explained birefringence by proposing light not as a longitudinal wave but as a transverse wave. Fresnel's improvement of Huygens theory finally described all aspects of light propagation. Within the context of the development of his famous laws, Maxwell later proposed that light waves were electromagnetic in nature, and Hertz confirmed that electromagnetic waves in the MHz range obeyed the same reflection and refraction laws as light. This meant that the wave theory of light stood unchallenged until the study of its interactions with matter began.

Planck (1900) studied the black-body radiation and found out that he could only correctly describe it by postulating that the internal energy of such body could only change as an integer number of a small quantity (the quanta). This necessarily meant that the electromagnetic field emitted by such a body would also change in discrete jumps of the size of that energy quantum, be it when absorbing or emitting the radiation. It was Einstein (1905) that proposed that light consisted of energy quanta, an assumption that allowed to explain the photoelectric effect. This did not mean by any means a return to the previous corpuscular model. It was evident at this point that no simple description would suffice, the latest contribution being the one presented by Feynman and others in the development of quantum electrodynamics. Light is now considered to propagate as a wave function and thus a probability amplitude. When that wave function interacts with matter (is detected), it collapses and is perceived as individual particles.

1.1.1. The resolving power of the microscope

The works from Galileo and Kepler started an era of continuous development of optical instruments, which provided the grounds for better astronomic and biological observations. At the same time, opening the doors to new discoveries kept driving the interest in improving the instrumentation.

The resolving power of an optical system is its ability to distinguish closely spaced objects as different. Astronomers realised that their ability to separate double star systems improved when they increased the size of the lens of their telescope, which increased the angular aperture of the instrument. For microscopes, increasingly small specimens with regular structures were observed and used as resolution pat-

terns, beginning with insect wings and moving to diatoms or the insides of cells. These observations helped scientists conclude that similarly to telescopes, the resolving power of a microscope depended on the angular aperture of the objective lens.

Beyond that rule, the design of microscopes was primarily based on trial and error until Abbe (1840-1905) produced a major breakthrough by proposing the sine condition for optical systems: the relationship that they must fulfil to produce images of objects.

1.1.1.1. Abbe's resolution criterion and image formation

Abbe's discovery made optical instruments manufacturers think that further improvement of their devices depended only on their skill in making better lenses or systems. However, Abbe again dismissed such ideas in 1873, when as a result of his continuous work on the subject, he showed that the geometrical optical theory, while a helpful abstraction, was incomplete since it did not take into consideration the wave properties of the light. In the geometrical approach, the main condition to produce a perfect image is that the rays from any point in the object should be refracted so that they meet together at a point on the image. Abbe showed that this condition could not possibly be met beyond a certain point: since waves spread through diffraction, they cannot intersect on a single point.

Abbe developed the diffraction theory of image formation by conducting experiments on optical systems, using a grating with controlled periodicity as the object. He noticed that light, after illuminating the grating and propagating through the lens, created a diffraction pattern in the focal plane of the lens when the image was properly in focus. In the particular case of studying his periodic grating, the diffraction pattern was a series of points where light focused. These points, and in general the patterns of light appearing at the focal plane of such system, are a natural representation of the Fourier transform of the object, and so the lower order diffraction spots (the ones closer to the centre of the optical system) correspond to the smaller order number of the Fourier transform, that is those representing the lower harmonics and low detail parts of the object.

Abbe went further and proposed that the points in the focal plane corresponding to diffraction orders act as point sources of light which emitted according to Huygens and Fresnel theory of spherical waves, as shown in figure 1.2. The wavefronts emitted from the focal plane interfere as they diffract, and in the image plane, this interference forms the image of the object grating: the image appears only indirectly from the actual points on the object, with the diffraction spots on the back focal plane of the lens being the critical aspect for image formation. Abbe conducted experiments with masks to block diffraction spots on the focal point, observing how it was akin to removing the corresponding component of the Fourier transform.

What this meant in terms of resolution and image formation is that in order to form a perfect image of any object, it is necessary to capture to the back focal

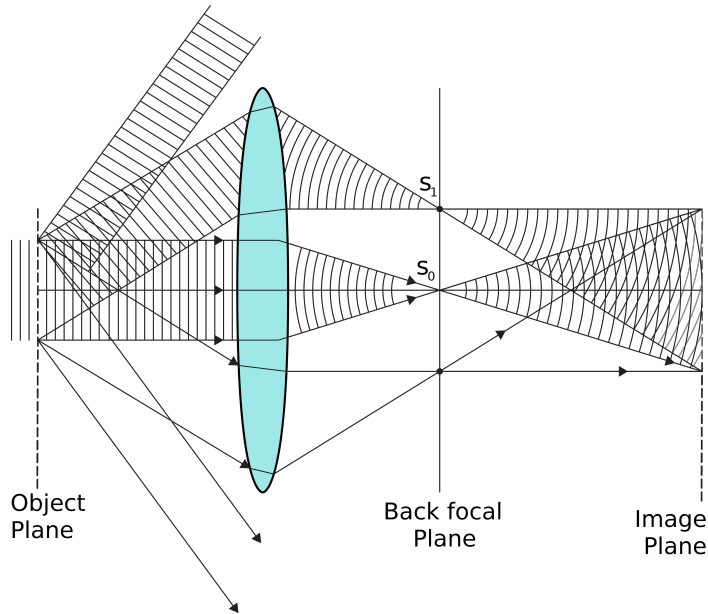


Figure 1.2: Image formation by diffraction of a grating. The object diffracts the illuminating light. The lens makes the wavefronts converge and produce a diffraction pattern at the back focal plane, with the spots (s_0, s_1) representing the diffraction orders. These points serve as emission points for the spherical waves of the second diffraction, which interfere to create the image of the object on the image plane.

plane of the lens an infinite number of Fourier terms, each appearing further away from the centre of the lens system, and so that it would be impossible to form the image of an object faithfully. Abbe set his resolution criterion based on his work with gratings illuminated by axial and coherent light and requiring that at the very least, the objective lens had to be wide enough (or close enough to the object) as to capture the rays necessary to form the diffracted first order spots on the back focal plane. From diffraction theory, the (half) angle necessary is shown to be $\sin \alpha = \lambda/d$, and offers a first approximation to the resolving power of the system.

Abbe also realised that the actual angular aperture of an objective would be affected by the mediums between the object and the surface and incorporated it by defining the *numerical aperture* (NA), as $NA = n \sin(\alpha)$, where n is the refractive index of the medium between the object and the lens. The resulting expression for the minimum observable grating distance is given by 1.1.

$$d = \frac{\lambda}{NA} \quad (1.1)$$

The fundamental equation in 1.1 means that the resolving power of such microscope can be increased by using light of shorter wavelengths, but that presents other limitations, as will be shown. As an example, since the absolute ideal angle α

can have is $\pi/2$ and thus $\sin \alpha = 1$, and using a glass lens immersed in oil with the same refractive index $n = 1.5$, illuminating with violet light at the limit of detection of the human eye with $\lambda = 380\text{nm}$, the resolution limit would be 253 nm.

Usually, Abbe's resolution limit is given with an additional $1/2$ factor in equation 1.1. However, it was pointed to Abbe that there were observations that seemed to go below his limit, and he realised this was because using oblique instead of direct axial illumination made it easier to capture light, doubling the resolving power of the objective.

1.1.1.2. Rayleigh's resolution criterion

Rayleigh's approach [8] to the resolution problem is a continuation of Abbe's work. Instead of thinking in terms of the image of a grating, he considered that each point on the object acted as a point source of light which generated spherical front waves propagating according to the Huygens-Fresnel principle. Even for a perfect optical system (one without defects in its lens and where even the naturally occurring aberrations are corrected), this meant that each of these points in the object would generate a distorted, larger image due to diffraction. This pattern is known as the Airy disks, which can be seen in figure 1.3. Objects close to each other create disks closer to each other, up to the point in which it is not possible to differentiate them both. Rayleigh, rather arbitrarily, chose the resolving limit at the point where the maximum of an Airy disk pattern produced by one object falls exactly on the 0 from the pattern of the object next to it. The condition can be shown in figure 1.3 b).

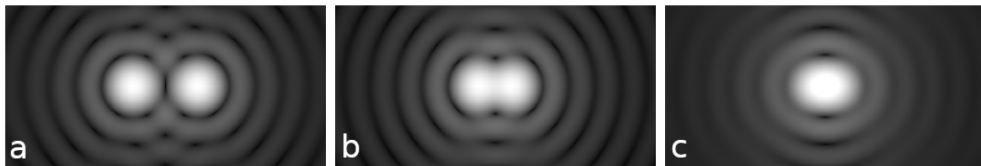


Figure 1.3: Airy disks from two point objects created by a diffraction-limited system. In a), both images can be clearly resolved. b) shows the limit condition, with the disks overlapping. In c), the images can no longer be resolved.

Without going into detail into diffraction theory and the origin of the Airy disk, we note that the first minimum on the Airy disk occurs at a distance of 1.22λ from the maximum at its centre, and it implies that there is a 19% dip in the total intensity. The smallest resolving detail will depend on the wavelength of the light used to illuminate the sample and the numerical aperture of the objective according to equation 1.2. Again, the expression in the equation is as easily found with an additional factor $1/2$ due to illuminating the sample with oblique light, which is standard practice. According to Rayleigh's criterion, the resolving power is less than that of Abbe because it takes contrast into account.

$$d = \frac{1.22\lambda}{NA} \quad (1.2)$$

1.1.1.3. Sparrow resolution criterion

While Rayleigh's criterion is the best-known one, it has problems in real applications: it fails to provide a proper resolution criterion if the diffraction pattern lacks well-defined zeros (due to noise, for example). It is also unnecessarily strict in plenty of cases since modern instrumentation can detect intensity dips much lower than the 19% it imposes. Sparrow [9] instead offered a criterion solving those issues: that two point images are considered to be resolved if the total intensity function detected presents a minimum between the maximums corresponding to each individual Airy disk. This translates into having a minimum resolution figure equal to Abbe's limit given in equation 1.1.

1.1.1.4. Observable world

The resolution criteria show that in order to increase the resolving power of an instrument, it is required to either increase the light captured by the objective or use lower wavelengths to illuminate the system. However, as shown in figure 1.4, there is plenty to observe below the resolving power of visible light microscopes, and this indeed meant the development of new microscopy techniques to try and gain information.

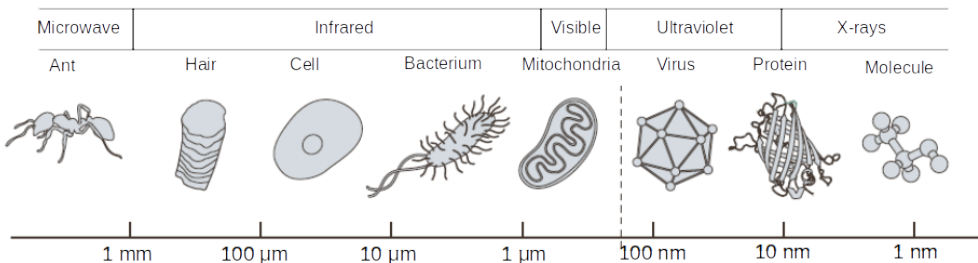


Figure 1.4: Part of the electromagnetic spectrum and the corresponding objects that could be resolved at each wavelength since they are of comparable size to it. The dashed line marks Abbe's diffraction limit for visible light, showing the smallest objects optical microscopes could resolve.

With the arrival of quantum mechanics and the principle of wave-particle duality, new forms of microscopy also developed: charged particles can have their trajectory changed by electromagnetic fields while presenting wave qualities such as diffraction. If carefully crafted, the EM fields can reproduce the refraction of a lens and make image formation possible. The obvious particle to use in such experiments were electrons, and the resulting electronic microscopy techniques have been extensively used. Following de Broglie's relation between the electron momentum and its wavelength, such devices can accelerate electrons into speeds that give them a wavelength on the order of size of atoms (~ 100 pm) or even less.

1.2. Microscopy techniques

1.2.1. Optical Microscopy

1.2.1.1. Visible light microscopy

Optical microscopy is the natural consequence of relying upon sight as our primary sense and the need to study things too small to be seen without the aid of instrumentation to provide magnification. While crude lenses had been used from ancient times, it was not until the early 1600s that the development of mathematics and science eased the first microscopes to appear and stimulated the curiosity to study the structure of objects too small to be seen by the bare eye. During the second half of the 17th century, the Dutch Antonie Philips van Leeuwenhoek, despite being self-taught, conducted careful and repeatable observations which credit him with the discovery of protists, bacteria and the vacuole of the cell, as well as being attributed with the first use of a stain to colour the specimens, using saffron. He did so with single-lens microscopes, which were very difficult to keep still and were affected by aberrations.

Composite microscopes, consisting of an objective lens and an eyepiece, are much more convenient. Nowadays, objectives and eyepieces are usually complex optical systems consisting of multiple lenses. In theory, such optical systems could provide an arbitrarily huge magnification, but as shown before, that does not guarantee that small details are resolvable. Despite that the compound microscope from Galileo preceded van Leeuwenhoek's work, it was not until the 1850s that compound microscopes provided the same quality as the single-lens systems due to the aberrations introduced by working with multiple lenses [10]. Nowadays, the aberrations in optical instruments are vanishing small, and the limitation is the diffraction limit.

1.2.1.2. Phase contrast microscopy

Unstained objects, such as living cells, are difficult to observe in ordinary bright-field microscopy because their images have very little contrast and are essentially invisible. Phase contrast microscopes transform differences in the phase of the light diffracted by transparent objects into amplitude differences in the image, which can then be detected. This supposed a fundamental revolution in biological observations and merited a Nobel Prize to Frits Zernike, who invented it in 1934.

The change in the phase of a light wave going through an object is due to the change in its optical path, which is expressed as the product of the refractive index and the thickness of the specimen, thus the optical path length between an object and the surrounding area will be different when the refractive indexes (and thicknesses) are different. In biological samples, the refractive index is related to the concentration of organic substances within it (proteins, lipids, nucleic acids). Therefore, the change in the optical path can even offer insight into the specific molecules it went through.

1.2.1.3. Ultra-violet microscopy

After Abbe's work showed the fundamental role of wavelength in the resolving power of microscopes, an obvious way of improving it was to use shorter wavelength radiation, moving to ultra-violet light (UV, wavelengths between 400 and 100 nm). The light source for such microscopes is usually a gas-discharge lamp, and a phosphor screen is used to convert the UV to visible light. Ordinary glass absorbs much of the UV radiation, so lenses are made from quartz or lithium fluoride materials. Microscopes operating with such wavelengths have applications in biology to study the internals of organelles with special UV absorption [11] and the study of non-organic materials. Ultra-violet light is very destructive to living cells, so any in-vivo observations using it will end relatively fast with the death of the sample. UV optical systems have found much more widespread use in photolithography, for example in the elaboration of masks to be used to fabricate microelectronic electronics.

1.2.1.4. Fluorescence Microscopy

Techniques leaning on fluorescence are another form of visible light microscopy. In the current days, they are quite active because fluorescence is at the base of plenty of super-resolution techniques. These techniques are discussed in a later section, but the phenomenon will be introduced here. Fluorescence had a vast impact on biological imaging, and a deeper discussion of both the mechanisms and applications can be found in the bibliography [12–15]. Some of the most relevant ones are to study the structure of intracellular structures such as the cellular membranes [16, 17], to observe the intracellular dynamics [18, 19], even in vivo when the tagging molecules are non-toxic [20, 21].

In contrast to other forms of light microscopy, which use the properties of the materials in the sample, fluorescence microscopy instead relies on the presence of specific molecules on it, either naturally occurring or tagged into molecules, which allows targeting specific molecules or ions such as proteins for example.

Fluorescence is a phenomenon through which a molecule absorbs energy which is then released after a short delay. In the most simple description, a fluorescent molecule has two states: a ground one and an excited one, separated by an electronic transition energy. Without any illumination, that transition energy is large enough to guarantee that the molecule remains at the ground state. However, when illuminated by light of a specific energy (remembering that the energy of photons can be defined as $E = h\nu$, where h is Planck's constant and ν is the frequency for the electromagnetic radiation), the photons are absorbed, and the molecule can change to the excited state. From that state, the molecule can relax back to the ground state by emitting a photon. Both excited and ground states are not definite states of specific energies, but rather a spread of bands, and so fluorescent molecules present an absorption spectrum as shown in figure 1.5a. The electrons in the excited state usually relax quite fast into the lowest bands of the state by dissipating that energy as heat. When a photon is then emitted to return to the ground state, it will have lower

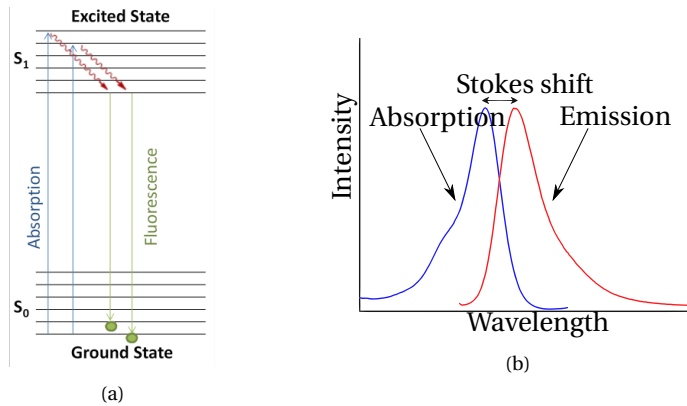


Figure 1.5: a) Schematic of a molecular system with the bands for both the excited and ground states, and showing the absorption and fluorescence emission paths, in what is called a Jablonski diagram. The de-excitation to the lowest orbital of the excited state is responsible for the Stokes shift b) Excitation and emission fluorescence spectra, showing the effects of the Stokes shift in the separation between the absorption and emission regions.

energy and so a higher wavelength, shifting to redder colours. This phenomenon is called Stokes shift and is quite important for fluorescence microscopy because, as it can be seen in figure 1.5b, it means that the excitation light can be removed from the observation by filtering it out, leaving only the light due to fluorescence.

1.2.1.5. Confocal microscopy

Confocal microscopy appears as a technique to confront one of the main issues from microscopy in general but particularly from fluorescence microscopy: the presence of background illumination mixing with the information of interest from the sample. Confocal microscopy corrects this by rejecting out-of-focus light, which is done by physically blocking the light from reaching the sensor (opposed to methods based on destructive interference). Minsky devised it in 1957 as a result of his attempts to observe the structure of the brain as a whole [22].

The modern confocal system consists of an intense illumination source -more often than not, a laser- an illumination pinhole and an objective lens to obtain a point-like focused spot of high intensity, which is scanned over the sample. Of equal importance is the detection pinhole, which produces a point-like image on the photon detector. While any microscopy technique can be used in a confocal approach, the most usual forms use reflected light (as opposed to transmitted), and usually in fluorescence microscopy, where the out-of-focus light poses a severe problem.

This technique provides higher contrast than the wide-field approach and allows to focus thin axial sections of the sample. These thin sections have then been used to reconstruct a 3D image of a complex sample without the need for invasive sectioning or destructive preparation.

While in theory, it would be possible to achieve super-resolution in fluorescence

imaging by decreasing the pinholes to sizes lower than those of the Airy disk involved in the system, this is not practical due to the massive rejection of the desired emission signal, which reduces the signal-to-noise ratio. It remains, therefore, useful as a technique for obtaining high-contrast images and has been the workhorse of cell biology.

1.2.2. Electron Microscopy

Electron microscopy uses magnetic fields carefully shaped to act as optical lenses on accelerated electrons. According to the relationship discovered by Louis de Broglie, the faster the electrons, the shorter the wavelength, which allows for resolutions much better than the conventional optic microscopes. Nowadays, electron microscopy offers the best resolving power, with a scanning transmission electron microscope having reached 39 pm resolution [23], but at the price of limiting the sample size and requiring complex and invasive sample preparation.

1.2.2.1. Transmission Electron Microscopy

In a Transmission Electron Microscopy (TEM), electrons penetrate a thin specimen and then are imaged by an electronic lens, in a process not unlike the light microscope. Thomson demonstrated in 1927 that accelerated electrons created diffraction patterns when they passed through thin crystalline material, very much as x-rays, which brought the question of if it would be possible to focus them as lenses do for light.

Electron lenses rely on the particle being negatively charged. The first designs were developed by Ernst Ruka in Berlin in 1931 and consisted of short coils carrying direct current. Two years later, his design produced images with resolution slightly above that of a light microscope.

TEM has been extensively used in material sciences to study the structure of solid materials and the presence of defects to distinguish even individual atoms. In life sciences, it has been used to image all kinds of tissue, bacteria and viruses, providing access to even the internal structure of organelles.

One handicap of the TEM technique is that electrons penetrate less than 1 μm into samples. This can be partially addressed with high voltage versions of the microscopes, but those instruments run into problems of stabilisation of the beam. Another problem is that high-energy electrons are even more harmful to biological samples than x-rays, and any living tissue is killed before any useful image can be taken from it.

1.2.2.2. Scanning Electron Microscopy

There are very early reports from the 1920s of experiments with the technique, but the first high resolution Scanning Electron Microscopy (SEM) is attributed to von Ardenne in 1937. He was attempting to surpass the resolution of TEM and address some of its problems.

In SEM, the highly energetic primary electrons are focused over a piece of the sample, providing energy to the atomic electrons of the sample, which are then emitted as much less energetic secondary electrons. Scanning the primary beam over the sample and recovering the secondary electrons allows forming an image of the area. Secondary electrons are not the only sources of information generated by the electron beam. SEM can also detect back-scattered electrons and X-rays, each providing information from deeper layers of the sample at the price of reduced resolution.

Modern SEM offers resolutions as low as 1 nm, far beyond the optical techniques, while not as good as what TEM can offer. Additionally, SEM has a larger depth of focus, with features from the sample appearing clearly despite being at different levels, which allows for detailed 3D imaging. Another advantage of SEM is that since it does not require that the electrons pass through the sample, it does not need to be cut to thin layers. This allows studying the surfaces of larger and intact specimens, though at the same price as TEM: costly sample preparation, incompatible with live observations.

1.2.3. Scanning Probe Microscopy

Scanning probe microscopy (SPM) is a family of techniques that scan a sharp tip (the probe) over the sample's surface in very close proximity. For the case of the first devices of this family to achieve high resolutions, the scanning tunnelling microscopes (STM), the tip has to be placed at 1 nm from the sample, without touching it. Such precision requires an absence of vibration and the use of feedback mechanisms to correct drifts in the positioning.

Since STM is based on the quantum tunnelling of electrons from the tip of the probe to the sample being studied, which has to be electrically conducting, it has resolutions on the order of 10 pm in the z-direction since the tunnelling current is highly dependent on the gap distance between the specimen and the probe. The lateral resolutions are also exceptionally high, even to the point of allowing the images of surfaces with a resolution of single atoms.

The problems STM faces are image artefacts due to electrons tunnelling to different and undesired parts of the sample (or from different parts of the probe) in the presence of irregularities or changes in conductivity. Other problems are the long times required to scan a sample while keeping the gap distance constant.

The STM inspired other scanning probe microscopes, such as the atomic force microscope (AFM). In this technique, the tip is approached to the sample until it is basically in contact with it to measure the interatomic force, and nowadays, it also has near-atomic resolving power. One advantage of AFM cantilever tips is that they can be fabricated in large quantities through photolithographic processes such as those used for semiconductors, which means that the tips can be easily replaced when damaged. Furthermore, while AFM has a slightly lower resolution than STM, it does not require a conducting sample and can operate with wet specimens, mak-

ing it especially useful in biological observations.

There are many other types within the SPM family, depending on the physical process used to obtain the information, such as SNOM (or NSOM, with lateral resolutions below 10 nm) [24] or Total Internal Reflection microscopy, with resolutions around 100 nm [25]. All the techniques share the approach of the small tip, with the advantage over electron microscopy of not requiring vacuum chambers for the samples, but with the disadvantages of presenting aberrations which are difficult to separate from the information observed, long scanning times, and also importantly that SPM methods offer only information about the very surface of the sample, with no insights on the interior.

1.2.4. Optical Super-resolution Microscopy

Super-resolution microscopy is a term covering a series of light microscopy techniques which offer resolving power beyond the diffraction limit predicted by Abbe. As seen with the techniques introduced during this chapter, while this limit seemed impossible to overcome, it was only so because it is built on the strict assumption that light must be collected by an objective. Super-resolution techniques use different approaches to escape that limitation: Stimulated Emission Depletion (STED) microscopy [26] and Structured Illumination Microscopy (SIM) [27] are based on patterned illumination and nonlinear optical effects coming from saturation phenomena to modulate the point spread function of the microscope. Another approach is to move away from the traditional objective geometry in order to collect a larger part of the spherical wavefront. Techniques such as 4Pi microscopy [28] and I^5M [29] collect light from both sides of the sample. There is yet another set of techniques that are based on localising single fluorophores, such as stochastic optical reconstruction microscopy (STORM) [30], photoactivation localisation microscopy (PALM) [31] or fluorescence photoactivation localisation microscopy (FPALM) [32].

1.2.4.1. STED

STED microscopy was proposed in 1994 by Stefan Hell and Jan Wichmann [26], and successfully implemented for the first time a few years later [33]. As in a standard confocal laser scanning microscope, a focused laser beam excites a fluorescent marker into its excited state. The difference is the addition of a second laser source, the STED illumination, which forces a stimulated emission from the zone of the fluorescent sample it illuminates. When the intensity of the de-excitation beam is high, the molecules absorbing it de-excite almost immediately, meaning that the fluorophore is effectively confined in the relaxed state. The de-excitation process does generate a photon, though it is of lesser energy and filtered out.

The key aspect of the technique is the shaping of the STED beam focus so that when it is compounded with the excitation focus, only an arbitrarily small zone of excitation is left. This can be seen in figure 1.6, which shows an example of the PSFs involved in the technique. Figure 1.6a presents a typical diffraction-limited

focused laser spot used to excite fluorescence. The usual shape for that beam is that of a torus, shown in figure 1.6b, which will allow excitation only on its centre, but other distributions have been used. The wavelength to stimulate emission is usually on the red end of the spectrum to ensure that the photons of such beam provide stimulated emission instead of being absorbed (since as shown in figure 1.5b any fluorophore will be less efficient in absorbing light towards the red end of the spectrum). At the same time, in order to be able to distinguish the actual stimulated emission from the desired -excited- fluorophores, it is necessary to be able to filter out the stimulated photons. Again, the emission spectrum also descends in relative intensity towards the red end, offering a window to apply such filter and remove the stimulated emission light. The resulting spot shown in figure 1.6c is the area in which fluorescence will be stimulated.

The lateral resolution d of this technique, given as the Full Width at Half Maximum (FWHM) of the volume where fluorescence emission is allowed, can be seen in equation 1.3, where d_c is the FWHM of the excitation beam (which would be the same for a confocal setup, and thus follows Abbe's relation from equation 1.1). a is a factor for the shape of the STED pattern, I the maximum intensity of the STED beam and I_{sat} the saturation intensity, which is characteristic for each fluorophore. From this expression follows that an increase in the STED intensity reduces the effective size of the image (the PSF).

$$d \approx \frac{d_c}{\sqrt{1 + d_c^2 a^2 \frac{I}{I_{sat}}}} \quad (1.3)$$

STED relies on two essential factors: that the process is nonlinear, that is, that the relation between the relaxation of the fluorophore and the intensity of the STED beam is exponential, while the normal excitation follows a linear relationship with the intensity of the excitation beam. This allows the creation of zones of saturated and depleted fluorophores. If both mechanisms were linear, it would be impossible to shape the PSF to be arbitrarily small. This presents the limitation that not all dyes are compatible with the technique, limiting the extent of fluorophores. Unlike others, this technique has the advantage of providing a super-resolution image directly without the need for any special post-processing of the received signal.

STED can provide images with a lateral resolution of 2 nm in solids [34], enabling, for example, the optical recording of electron spin resonances [35]. One of the problems common in all scanning techniques is a long time required to obtain a whole image. However, since the focal spot size depends on the relationship of intensities of the excitation and STED beams, the actual spot size can be regulated to what is required for the task, giving flexibility to the technique, with 80 frames per second achieved [36].

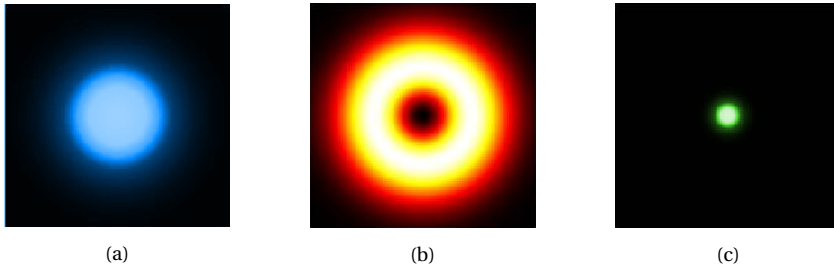


Figure 1.6: STED illumination spots / PSFs. a) is the excitation spot, a laser focused to the limit allowed by diffraction. b) shows a typical toroidal de-excitation beam. c) presents the area where fluorescence is allowed, as a result of the composition of a) and b)

1.2.4.2. SIM

Structured Illumination Microscopy found two distinct uses: it directly addresses the long scan times characteristic of confocal microscopy by allowing similar sectioning of the sample while allowing a fast acquisition of the image since it is a wide-field technique. The sample is illuminated by a harmonic pattern such as a grating or an array of points. Images are acquired from different positions of the resulting light distribution, and from there a sectioned image can be computed by dedicated software.

Besides the optical sectioning of a sample, though, the technique allows for the acquisition of images beyond Abbe's limit of resolution. Furthermore, using the Moiré effect, this technique allows an improvement of the resolving power by a factor of two (so the smallest resolvable sizes becoming $\sim \frac{\lambda}{4}$ instead of $\sim \frac{\lambda}{2}$).

The Moiré effect is the coarse, low-frequency pattern appearing as a result of the multiplication of two smaller high frequency ones. It can be observed in everyday life, sometimes when looking through two fences. This effect is exploited in SIM: the sample contains high frequency information, invisible by the microscope. When illuminated by a fine illumination pattern, a coarse distribution that can be easily detected appears as a result of the convolution. Properly reconstruction of the sample requires obtaining several images from different positions.

1.2.4.3. 4Pi and I^5M

Most of the super-resolution techniques prioritise lateral resolution over the axial one. 4Pi microscopy, on the other hand, specialises in increasing it. While with a single lens the absolute (theoretical) maximum angle to collect light is 2π , this technique uses two opposed objectives to approach the limit of capturing the entire spherical wave from a focus point, which would be an angle of 4π and hence the name. Not only is light collected from both sides of the emitting point of the sample: the collected wavefronts constructively interfere. This technique allows axial resolutions around 50 nm [37] but does not improve on lateral resolution over conventional optical microscopy.

4Pi has been thus used to obtain plenty of observations of biological samples since it shares plenty of the capabilities of conventional optics. It also offered a new tool to measure the thickness of the thin cellular structures with very high precision, thanks to the quantification of the ratio of the interference of the light captured on both sides, allowing for example to measure the diameter of tubules of the mitochondrial network [38]. A point of interest of the 4Pi technique is that it is used in combination with other super-resolution techniques to obtain 3D super-resolution, for example with STED microscopy [39].

I^5M is related to 4Pi. It is the result of the combination of two interference-based techniques: image interference microscopy (I^2M) and incoherent interference illumination (I^3M) [29]. In the first, fluorescence emission beams are collected from two opposed objective lenses and are superimposed on a CCD sensor after going through precisely the same optical distance, with the image being the result of the interference of the two beams. In the I^3M mode, the sample is illuminated from both sides with incoherent light and is polarised so that the beams interfere at the focal plane, creating a standing wave that excites a smaller area of a fluorescent sample. A detector recovers the emission from that fluorescence. The combined methods produce a high axial resolution but operate with wide-field and single-photon illumination.

1.2.4.4. STORM, PALM, FPALM

Despite the different names, these three techniques use a similar strategy to localise fluorophores with nanometer precision: they rely on having only a single fluorophore molecule active at any given moment within a diffraction-limited area. The images of spots that would be too close to resolve are decoupled in time, taken at different moments.

Before taking an image, the fluorophores are either at the ground state (in photoactivated localisation microscopy or PALM and fluorescent photoactivated localisation microscopy or FPALM). Then, a laser pulse excites a tiny fraction of fluorophores to their excited state, and the resulting fluorescence emission is then detected. This process is repeated many times, each stochastically activating different molecules until enough spots are collected to reconstruct the image. When PALM is carried on a confocal setup, it is named FPALM [32].

Stochastic optical reconstruction microscopy (STORM) requires the use of specific activable fluorescent dyes, such as carbocyanine pairs (Cy3 and Cy5). These labels are attached to the molecules of interest and consist of cycling the activation of the Cy5 label as explained for PALM. To do so, a red imaging laser is used to force the Cy5 molecule to a dark state. Next, a green activating laser pulse is absorbed by the Cy3 molecules, which then switch a small random number of Cy5 molecules to an active state. Then, the red laser is pulsed again, enabling the emission of the Cy5 molecules, and a frame is captured before they are forced back to a dark state and unable to fluoresce.

Despite the spots of light captured in these techniques being diffraction-limited, the position of the emitting molecule can be obtained using a software correction: the detected intensity and point spread function is fitted to a Gaussian function, with the position of the molecule being assigned to the centre of the distribution. Since this operation is statistical, obtaining a good fit requires the acquisition of several photons from each spot.

These techniques provided ~ 2 nm resolutions of fluorescent proteins. Imaging living cells is more difficult due to the inherent movements of the molecules and the long times required to build the final image, but resolutions of 40 nm in living cells have been obtained [40]. In addition, the involved setups are relatively simple and thus low cost, though the acquisition is slow and post-processing is required to calculate the position of the molecules.

1.2.4.5. Comparison of super-resolution techniques

The techniques presented before offer distinct possibilities to approach an observation, each with its capabilities. Table 1.1 aims at providing some summarised comparisons between the techniques. Which one to use will depend on the final application, and a deeper review of the techniques with insights aimed at selecting the best technique can be found in the literature [41].

1.2.5. Lensless Microscopy

The holographic principle presented by Gabor in 1948 [51] was initially used in electron microscopy, as well as x-ray setups. This technique has recently seen increased use with visible light and in life sciences, serving as an alternative approach to classical optical microscopy. Taking advantage of the electronics downscaling as well as of the increased availability of processing power, lensless setups have attracted interest due to the possibility to build simple, miniaturised and inexpensive setups with good optical capabilities, thanks to the lack of optical elements [52–57], even enabling the integration of microfluidics directly on dedicated microscopes [58]. With these capabilities, lensless microscopes evolved to become widely used, for example, in disease diagnosis [59], tracking of biological samples [60] or microbial observation [61].

A typical lensless holographic setup can be seen in figure 1.7, consisting of a light source, the semi-transparent sample, and as close as possible under it the imaging sensor chip. The sample casts an inline hologram over the sensor as a result of being illuminated by the light source, which can be a laser [62] but also a LED in portable devices [63]. While plenty of setups use a pinhole to improve the spatial resolution of the setup [58], this is not even required if the distance z_1 is large enough when compared with z_2 [64]. In these conditions, the magnification of the setup is $M = 1$, and the Field Of View (FOV) is the entire area of the image sensor chip. Accordingly, the resolving power of such setup is limited by the maximum frequency the sensor can capture, which depends on its pixel size and fill factor [65].

Techniques	STED	SIM	PALM / STORM / FPALM
Lateral Resolution	40 nm	100-130 nm	20-50 nm
Axial Resolution*	500 / 20-100 nm	250 / 100 nm	100 / 20 nm
Detection	Scanning	Wide-field	Wide-field
Fluorophore choice	Limited (STED compatible)	Broad	Restricted, photoswitchable for STORM
Imaging speed	Seconds	Milliseconds to seconds	Seconds
Requires data processing?	No	Yes	Yes
Setup complexity	High	Medium to high	Low to medium
3D	Yes, isoSTED	Yes, 3D SIM, I5S	Yes, 3D STORM, iPALM
Refs	[41–44]	[41, 45–47]	[41, 48–50]

Table 1.1: Comparison of super-resolution microscopy techniques. *The axial resolution is given in both the normal amount and the amount obtained through the 3D technique applied, separated by /

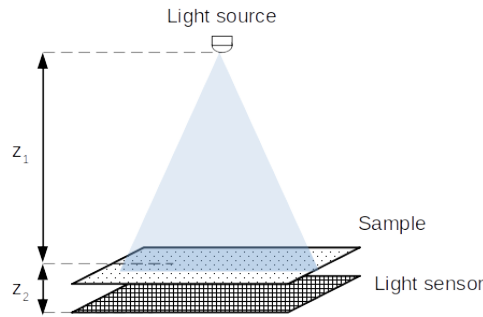


Figure 1.7: Schematic of a simplified lensless holographic setup for on-chip microscopy.

However, pixel super-resolution algorithms can be used to generate effective pixel sizes smaller than the wavelength of the light used for illumination [66], but at the cost of adding additional components. Another limitation to the resolving power of such setups is the temporal coherence of the light source [67], which requires the light source to have a quite narrow wavelength spectrum.

The holography used in these lensless setups can be used with some adaptations to obtain information about the intensity reaching the sensor and the phase of the electromagnetic field. In such cases, the technique is usually referred to as ptychography [68].

Ptychography is fundamentally a computational technique: with the same setup presented before for the basic intensity measurement, several measurements are taken while changing the relative positions of the object and the light source. This data is then fed to an algorithm that solves the diffraction problem, reconstructing the image and obtaining the intensity pattern and the phase. It was developed mainly for x-ray and electron microscopes as a way of obtaining high resolutions without using optics, which are challenging to develop for those setups [69].

Despite this competition with the improvement of optical elements, the main advantage it presents and where scientific interest is focusing is the possibility to use it to obtain tomographical images [70]. This is done in x-ray [71], wavelengths which are well suited for the technique since the rays are not easily absorbed by most materials and so provide good energy at the sensor. Tomography is also used with visible light and compares favourably with confocal microscopy because it does not need specific labelling of the sample [72].

While the setups we will construct in this thesis are similar to those used in ptychographic microscopy, our objective is entirely different. We will not use a coherent light source but instead miniaturised LEDs. Furthermore, we do not intend in this work to attempt phase recovery at all: as it will be shown, it can be seen as a different approach to the lenses digital inline holography pictured in figure 1.7, but it can be interesting in the future to investigate the application of the developments of ptychographic techniques in the microscopes that will be developed.

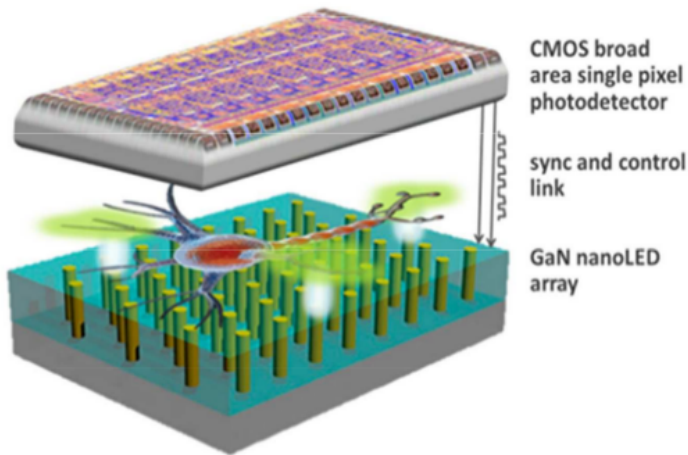


Figure 1.8: Schematic of the basic Nano Illumination Microscope (NIM) distribution

1.3. Thesis motivation

As shown, super-resolution is a very active field of research that offered many new insights about the natural world below the barrier set by Abbe's limit for visible light microscopy. At the same time, the microscopy methods capable of super-resolution require costly and bulky setups. Moreover, even conventional optical microscopes capable of operating near Abbe's limit are quite sensitive and not really suitable as mobile devices to be used in the field.

With these problems in mind, the EU funded the H2020-FETOPEN ChipScope research project, which aimed to provide a new kind of super-resolution microscope but take the approach of lensless setups to make it low-cost and compact.

We named this new method Nano Illumination Microscopy (NIM) because it relies on using nanometric light sources in an ordered array to illuminate a sample placed in close proximity to them, as shown in figure 1.8, where a hypothetical biological sample is placed over the array of GaN-based nano-LEDs. In a setup like this, the resolving power is provided by the nano-LEDs and their distribution instead of the sensing devices, as is the case in the other methods, referenced in the figure by the broad area single-pixel detector. Therefore, only some geometrical considerations have to be taken into account regarding this sensor and its placement and dimensions to avoid imaging artifacts, and the final proposed microscope is compact and low cost, suitable to be developed into a point of care device to be used in the field.

Since the resolving power depends on the pitch of the LED array, this method also sets a path to obtain super-resolution images, depending only on obtaining LED arrays with smaller pitches. This rides on the development of micro and nano LEDs in arrays for microdisplays, an active field of research.

Despite this, displays for recreational use do not have the same requirements as the ones to be used in our microscopy technique. They can afford thick insulation to protect the LEDs, while as it will be shown in this thesis, this is a problem for microscopes using the Nano Illumination Microscopy (NIM) principle. This means that while the development of the nanoLED technology will help, their application to microscopy will probably require specialised custom LED array designs.

Another field open to study for this kind of microscope is the possibility of studying fluorescent samples. Combined with small size light sources, this might offer further resolution improvements or at least be used to detect labelled antibodies present in the sample.

The ChipScope European project is a joint effort of an interdisciplinary consortium, consisting on:

- Technische Universität Braunschweig, in charge of developing semiconductor nano light-emitting diode (nanoLED) arrays for the microscope.
- University Tor Vergata Roma, who provided the simulations of the LED operation
- Austrian Institute of Technology, which provided high-precision and micro-volume pumps and fluidic system for carrying samples into position within the microscope.
- Ludwig-Maximilians-Universität München took care of calibration and characterisation steps of the microscope
- Medical University of Vienna studied suitable applications in the medical sciences, as well as providing living samples.
- Swiss Foundation for Research in Microtechnology was in charge of providing dissemination of the project.
- Universitat de Barcelona, responsible for developing and studying the sensors, integrating the microscopes and coordinating the European Project.

After the introduction to microscopy offered in this chapter, we continue in chapter 2 by presenting the main components of the microscope prototypes built in the context of this thesis, beginning with the Complementary Metal-Oxide Semiconductor (CMOS) Single Photon Avalanche Diode (SPAD) detectors developed for using in the microscope as well as their particular characteristics, going into detail with the electronic circuits used to control them. Also included is a brief mention of other commercial cameras used in the later stages of the work.

The other main component of the microscopes is also introduced: the LED array and a small overview of LED technology. The different devices used are presented and briefly discussed.

Moving on, chapter 3 presents and studies the NIM concept, with simulations showing how images are formed with this scanning method. This information is then used to build the very first prototype, a microscope capable of forming 8x8 pixel images -since that is the form factor of the LED array used, with LEDs of 5 μm in size (and 10 μm in pitch).

The first results from this technique are presented and compared with the simulations, showing the agreement between both, validating the method, and offering insight on building the next prototypes, which will use smaller LEDs in an attempt to study the technological limits.

Chapter 4 details this push for the limits, testing for the best implementations and confronting the limitations which arise. Some of those came from the structure of the LED arrays themselves: while nano-LEDs well below the sizes used have been reported [73, 74], those have been isolated structures or non individually addressable. Selecting exactly which LED will emit is one of the main problems to solve since with increasingly large arrays, the connections required increase exponentially until routing is impossible. The thesis also studies this problem, as the LED arrays were changed in search of the proper solution. This implied moving from a direct addressing strategy, in which each LED was selected individually, towards a matrix-addressing format, in which the LEDs are selected by polarising the appropriate row and columns.

The thesis concludes with a synthesis chapter that offers an outlook of how the developments this microscopy technique can follow.

1.4. Conclusions

Humans use sight as our primary sense to study the world around us, and hence visible light. Pursuing a more profound understanding of the structure of the world drove a constant push for being able to obtain information from objects smaller than we could see with the naked eye.

This push manifested first with approaches at using lenses, quite limited by the technological methods available until at the Renaissance the knowledge improved enough to finally allow the telescopes and microscopes to appear, opening entirely new fields of study.

The push for seeing smaller things continued, and in the s. XIX Abbe, as well as nearly perfecting the optical, lens-based microscopes, also offered what seemed like a definitive physical limitation to how small we would be able to see: Abbe's diffraction limit, telling that it would not be possible to resolve objects smaller than the wavelength of the light used to illuminate them.

Nevertheless, the curiosity to see further inside things did not disappear, and the paradigm shift of quantum mechanics opened new ways for it: electronic microscopes offered the first insights, and more recently, the different super-resolution methods, allowing us to resolve objects as small as a nanometer.

These methods have been a true revolution in many aspects, earning the Nobel Prize in Chemistry in 2014. Despite this, they all present the hindrance of requiring bulky and expensive equipment and delicate procedures.

On the other hand, improvements in the integration of electronics also opened the way for new kinds of microscopy techniques, moving in opposite directions than that of super-resolution methods: lensless microscopes eliminate optical elements, reducing the size and cost of the device, using the reduction in the size of the sensors to obtain resolutions on the order of the micron, or below when using additional computational techniques.

These developments inspired us to explore if we could offer super-resolution in a lensless setup to offer a compact and low-cost alternative to the methods currently existing. This materialised in the ChipScope European project and in the work presented in this thesis, in which a new kind of microscope is developed. Instead of obtaining its resolving power from miniaturised sensors, this microscope is based on miniaturising the light sources, which have the potential to be fabricated in smaller sizes than sensors are, thus having potential for greater resolving power than conventional lensless setups while keeping their advantages.

References

- [1] Andrew R. Parker. “On the origin of optics”. In: *Optics & Laser Technology* 43.2 (Mar. 2011), pp. 323–329. ISSN: 00303992. DOI: 10.1016/j.optlastec.2008.12.020.
- [2] Brian Vohnsen. “A Short History of Optics”. In: *Physica Scripta* T109 (2004), p. 75. ISSN: 0031-8949. DOI: 10.1238/Physica.Topical.109a00075.
- [3] P. K. Hoenich, Vasco Ronchi, and V. Barocas. “The Nature of Light: A Historical Survey”. In: *Leonardo* 6.1 (1973), p. 74. ISSN: 0024094X. DOI: 10.2307/1572442.
- [4] Roshdi Rashed. “A Pioneer in Anaclastics Ibn Sahl on Burning Mirrors and Lenses”. In: *New Perspectives on the History of Islamic Science*. Routledge, May 2017, pp. 271–298. DOI: 10.4324/9781315248011-14.
- [5] Bruce Eastwood and David C. Lindberg. “Theories of Vision from Al-Kindi to Kepler”. In: *The American Historical Review* 82.2 (Apr. 1977), p. 334. ISSN: 00028762. DOI: 10.2307/1849957.
- [6] Massimo Guarnieri. “Two Millennia of Light: The Long Path to Maxwell’s Waves”. In: *IEEE Industrial Electronics Magazine* 9.2 (2015), pp. 54–57. ISSN: 19324529. DOI: 10.1109/MIE.2015.2421754.
- [7] David Park and A. P. French. “The Fire within the Eye: A Historical Essay on the Nature and Meaning of Light”. In: *American Journal of Physics* 66.3 (Mar. 1998), pp. 262–263. ISSN: 0002-9505. DOI: 10.1119/1.18857.

- [8] Rayleigh. “XXXI. Investigations in optics, with special reference to the spectroscope”. In: *The London, Edinburgh, and Dublin Philosophical Magazine and Journal of Science* 8.49 (Oct. 1879), pp. 261–274. ISSN: 1941-5982. DOI: 10.1080/14786447908639684.
- [9] C. Sparrow. “On Spectroscopic Resolving Power”. In: *The Astrophysical Journal* 44 (1916), p. 76. DOI: 10.1086/142271.
- [10] J L Riddell. “On the Binocular Microscope”. In: *Quarterly Journal of Microscopical Science* s1-2.5 (1854), 18 LP –24.
- [11] J. Smiles. “ULTRAVIOLET MICROSCOPY”. In: *Journal of Applied Bacteriology* 21.1 (June 1958), pp. 137–142. ISSN: 00218847. DOI: 10.1111/j.1365-2672.1958.tb00127.x.
- [12] Joseph R. Lakowicz and Barry R. Masters. “Principles of Fluorescence Spectroscopy, Third Edition”. In: *Journal of Biomedical Optics* 13.2 (2008). ISSN: 10833668. DOI: 10.1117/1.2904580.
- [13] Bernard Valeur and Mário Nuno Berberan-Santos. *Molecular Fluorescence*. Weinheim, Germany: Wiley-VCH Verlag GmbH & Co. KGaA, Apr. 2012. ISBN: 9783527650002. DOI: 10.1002/9783527650002.
- [14] Rodney Loudon and Thomas von Foerster. “The Quantum Theory of Light”. In: *American Journal of Physics* 42.11 (Nov. 1974), pp. 1041–1042. ISSN: 0002-9505. DOI: 10.1119/1.1987930.
- [15] Nicholas J. Turro, Vaidhyanathan Ramamurthy, and Juan C. Scaiano. “Modern Molecular Photochemistry of Organic Molecules”. In: *Photochemistry and Photobiology* 88.4 (July 2012), pp. 1033–1033. ISSN: 1751-1097. DOI: 10.1111/j.1751-1097.2012.01178.x.
- [16] Ariana Velasco-Olmo et al. “Combining patch-clamping and fluorescence microscopy for quantitative reconstitution of cellular membrane processes with Giant Suspended Bilayers”. In: *Scientific Reports* 9.1 (Dec. 2019), p. 7255. ISSN: 2045-2322. DOI: 10.1038/s41598-019-43561-4.
- [17] D.J. Frankel et al. “Revealing the Topography of Cellular Membrane Domains by Combined Atomic Force Microscopy/Fluorescence Imaging”. In: *Biophysical Journal* 90.7 (Apr. 2006), pp. 2404–2413. ISSN: 00063495. DOI: 10.1529/biophysj.105.073692.
- [18] Carla De Los Santos et al. “FRAP, FLIM, and FRET: Detection and analysis of cellular dynamics on a molecular scale using fluorescence microscopy”. In: *Molecular Reproduction and Development* 82.7-8 (July 2015), pp. 587–604. ISSN: 1040452X. DOI: 10.1002/mrd.22501.

- [19] Sohila Zadran et al. “Fluorescence resonance energy transfer (FRET)-based biosensors: visualizing cellular dynamics and bioenergetics”. In: *Applied Microbiology and Biotechnology* 96.4 (Nov. 2012), pp. 895–902. ISSN: 0175-7598. DOI: 10.1007/s00253-012-4449-6.
- [20] Elizabeth A. Specht, Esther Braselmann, and Amy E. Palmer. “A Critical and Comparative Review of Fluorescent Tools for Live-Cell Imaging”. In: *Annual Review of Physiology* 79.1 (Feb. 2017), pp. 93–117. ISSN: 0066-4278. DOI: 10.1146/annurev-physiol-022516-034055.
- [21] Liang Gao et al. “3D live fluorescence imaging of cellular dynamics using Bessel beam plane illumination microscopy”. In: *Nature Protocols* 9.5 (May 2014), pp. 1083–1101. ISSN: 1754-2189. DOI: 10.1038/nprot.2014.087.
- [22] M. Minsky. “Memoir on inventing the confocal scanning microscope”. In: *Scanning* 10.4 (1988), pp. 128–138. ISSN: 01610457. DOI: 10.1002/sca.4950100403.
- [23] Yi Jiang et al. “Electron ptychography of 2D materials to deep sub-ångström resolution”. In: *Nature* 559.7714 (July 2018), pp. 343–349. ISSN: 0028-0836. DOI: 10.1038/s41586-018-0298-5.
- [24] Xinzhong Chen et al. “Modern Scattering-Type Scanning Near-Field Optical Microscopy for Advanced Material Research”. In: *Advanced Materials* 31.24 (Apr. 2019), p. 1804774. ISSN: 0935-9648. DOI: 10.1002/adma.201804774.
- [25] Min Guo et al. “Single-shot super-resolution total internal reflection fluorescence microscopy”. In: *Nature Methods* 15.6 (June 2018), pp. 425–428. ISSN: 1548-7091. DOI: 10.1038/s41592-018-0004-4.
- [26] Stefan W. Hell and Jan Wichmann. “Breaking the diffraction resolution limit by stimulated emission: stimulated-emission-depletion fluorescence microscopy”. In: *Optics Letters* 19.11 (June 1994), p. 780. ISSN: 0146-9592. DOI: 10.1364/OL.19.000780.
- [27] M. G. L. Gustafsson. “Surpassing the lateral resolution limit by a factor of two using structured illumination microscopy. SHORT COMMUNICATION”. In: *Journal of Microscopy* 198.2 (May 2000), pp. 82–87. ISSN: 0022-2720. DOI: 10.1046/j.1365-2818.2000.00710.x.
- [28] Stefan W. Hell et al. “Confocal microscopy with an increased detection aperture: type-B 4Pi confocal microscopy”. In: *Optics Letters* 19.3 (Feb. 1994), p. 222. ISSN: 0146-9592. DOI: 10.1364/OL.19.000222.
- [29] Gustafsson, Agard, and Sedat. “I5M: 3D widefield light microscopy with better than 100 nm axial resolution”. In: *Journal of Microscopy* 195.1 (July 1999), pp. 10–16. ISSN: 0022-2720. DOI: 10.1046/j.1365-2818.1999.00576.x.
- [30] Michael J Rust, Mark Bates, and Xiaowei Zhuang. “Sub-diffraction-limit imaging by stochastic optical reconstruction microscopy (STORM)”. In: *Nature Methods* 3.10 (Oct. 2006), pp. 793–796. ISSN: 1548-7091. DOI: 10.1038/nmeth929.

- [31] Eric Betzig et al. “Imaging Intracellular Fluorescent Proteins at Nanometer Resolution”. In: *Science* 313.5793 (Sept. 2006), pp. 1642–1645. ISSN: 0036-8075. DOI: 10.1126/science.1127344.
- [32] Samuel T. Hess, Thanu P.K. Girirajan, and Michael D. Mason. “Ultra-High Resolution Imaging by Fluorescence Photoactivation Localization Microscopy”. In: *Biophysical Journal* 91.11 (Dec. 2006), pp. 4258–4272. ISSN: 00063495. DOI: 10.1529/biophysj.106.091116.
- [33] Thomas A Klar and Stefan W Hell. “Subdiffraction resolution in far-field fluorescence microscopy”. In: *Optics Letters* 24.14 (July 1999), p. 954. ISSN: 0146-9592. DOI: 10.1364/OL.24.000954.
- [34] Dominik Wildanger et al. “Solid immersion facilitates fluorescence microscopy with nanometer resolution and sub-Ångström emitter localization”. In: *Advanced Materials* 24.44 (2012). ISSN: 09359648. DOI: 10.1002/adma.201203033.
- [35] Dominik Wildanger, Jeronimo R. Maze, and Stefan W. Hell. “Diffraction Unlimited All-Optical Recording of Electron Spin Resonances”. In: *Physical Review Letters* 107.1 (July 2011), p. 017601. ISSN: 0031-9007. DOI: 10.1103/PhysRevLett.107.017601.
- [36] V. Westphal et al. “Dynamic far-field fluorescence nanoscopy”. In: *New Journal of Physics* 9 (2007). ISSN: 13672630. DOI: 10.1088/1367-2630/9/12/435.
- [37] Stefan Hell and Ernst H. K. Stelzer. “Properties of a 4Pi confocal fluorescence microscope”. In: *Journal of the Optical Society of America A* 9.12 (Dec. 1992), p. 2159. ISSN: 1084-7529. DOI: 10.1364/JOSAA.9.002159.
- [38] Andrea Dlasková et al. “Distribution of mitochondrial DNA nucleoids inside the linear tubules vs. bulk parts of mitochondrial network as visualized by 4Pi microscopy”. In: *Journal of Bioenergetics and Biomembranes* 47.3 (June 2015), pp. 255–263. ISSN: 0145-479X. DOI: 10.1007/s10863-015-9610-3.
- [39] Wenjie Liu et al. *Breaking the Axial Diffraction Limit: A Guide to Axial Super-Resolution Fluorescence Microscopy*. 2018. DOI: 10.1002/lpor.201700333.
- [40] Samuel T. Hess et al. “Dynamic clustered distribution of hemagglutinin resolved at 40 nm in living cell membranes discriminates between raft theories”. In: *Proceedings of the National Academy of Sciences of the United States of America* 104.44 (2007). ISSN: 00278424. DOI: 10.1073/pnas.0708066104.
- [41] Lothar Schermelleh et al. “Super-resolution microscopy demystified”. In: *Nature Cell Biology* 21.1 (Jan. 2019), pp. 72–84. ISSN: 1465-7392. DOI: 10.1038/s41556-018-0251-8.
- [42] Christian Eggeling et al. “Lens-based fluorescence nanoscopy”. In: *Quarterly Reviews of Biophysics* 48.2 (May 2015), pp. 178–243. ISSN: 0033-5835. DOI: 10.1017/S0033583514000146.

- [43] Eva Wegel et al. “Imaging cellular structures in super-resolution with SIM, STED and Localisation Microscopy: A practical comparison”. In: *Scientific Reports* 6 (2016). ISSN: 20452322. DOI: 10.1038/srep27290.
- [44] Kseniya Korobchevskaya et al. “Exploring the potential of Airyscan microscopy for live cell imaging”. In: *Photonics* 4.3 (2017). ISSN: 23046732. DOI: 10.3390/photonics4030041.
- [45] Colin J. R. Sheppard, Shalin B. Mehta, and Rainer Heintzmann. “Superresolution by image scanning microscopy using pixel reassignment”. In: *Optics Letters* 38.15 (2013). ISSN: 0146-9592. DOI: 10.1364/ol.38.002889.
- [46] Justin Demmerle et al. “Assessing resolution in super-resolution imaging”. In: *Methods* 88 (2015). ISSN: 10959130. DOI: 10.1016/j.ymeth.2015.07.001.
- [47] David Baddeley and Joerg Bewersdorf. *Biological Insight from Super-Resolution Microscopy: What We Can Learn from Localization-Based Images*. 2018. DOI: 10.1146/annurev-biochem-060815-014801.
- [48] Yuji Ishitsuka, Karin Nienhaus, and G. Ulrich Nienhaus. “Photoactivatable fluorescent proteins for super-resolution microscopy”. In: *Methods in Molecular Biology* 1148 (2014). ISSN: 10643745. DOI: 10.1007/978-1-4939-0470-9_16.
- [49] Bo Huang et al. “Three-dimensional super-resolution imaging by stochastic optical reconstruction microscopy”. In: *Science* 319.5864 (2008). ISSN: 00368075. DOI: 10.1126/science.1153529.
- [50] Sri Rama Prasanna Pavani et al. “Three-dimensional, single-molecule fluorescence imaging beyond the diffraction limit by using a double-helix point spread function”. In: *Proceedings of the National Academy of Sciences of the United States of America* 106.9 (2009). ISSN: 00278424. DOI: 10.1073/pnas.0900245106.
- [51] D. Gabor. *A new microscopic principle*. 1948. DOI: 10.1038/161777a0.
- [52] Waleed S. Haddad et al. “Fourier-transform holographic microscope”. In: *Applied Optics* (2009). ISSN: 0003-6935. DOI: 10.1364/ao.31.004973.
- [53] W. Xu et al. “Digital in-line holography for biological applications”. In: *Proceedings of the National Academy of Sciences* (2002). ISSN: 0027-8424. DOI: 10.1073/pnas.191361398.
- [54] L. Repetto, E. Piano, and C. Pontiggia. “Lensless digital holographic microscope with light-emitting diode illumination”. In: *Optics Letters* (2004). ISSN: 0146-9592. DOI: 10.1364/OL.29.001132.
- [55] Giancarlo Pedrini and Hans J. Tiziani. “Short-coherence digital microscopy by use of a lensless holographic imaging system”. In: *Applied Optics* (2007). ISSN: 0003-6935. DOI: 10.1364/ao.41.004489.

- [56] Alok Kumar Singh et al. "Scatter-plate microscope for lensless microscopy with diffraction limited resolution". In: *Scientific Reports* 7.1 (2017), pp. 1–8. ISSN: 20452322. DOI: 10.1038/s41598-017-10767-3.
- [57] Aydogan Ozcan and Euan McLeod. "Lensless Imaging and Sensing". In: *Annual Review of Biomedical Engineering* (2016). DOI: 10.1146/annurev-bioeng-092515-010849.
- [58] Antonio C. Sobieranski et al. "Portable lensless wide-field microscopy imaging platform based on digital inline holography and multi-frame pixel super-resolution". In: *Light: Science and Applications* 4.10 (2015). ISSN: 20477538. DOI: 10.1038/lsa.2015.119.
- [59] Casey W. Pirnstill and Gerard L. Coté. "Malaria Diagnosis Using a Mobile Phone Polarized Microscope". In: *Scientific Reports* (2015). ISSN: 20452322. DOI: 10.1038/srep13368.
- [60] John F. Restrepo and Jorge Garcia-Sucerquia. "Automatic three-dimensional tracking of particles with high-numerical-aperture digital lensless holographic microscopy". In: *Optics Letters* (2012). ISSN: 0146-9592. DOI: 10.1364/ol.37.000752.
- [61] Yichen Wu and Aydogan Ozcan. *Lensless digital holographic microscopy and its applications in biomedicine and environmental monitoring*. 2018. DOI: 10.1016/j.ymeth.2017.08.013.
- [62] Alon Greenbaum et al. "Wide-field computational imaging of pathology slides using lens-free on-chip microscopy". In: *Science Translational Medicine* 6.267 (2014). ISSN: 19466242. DOI: 10.1126/scitranslmed.3009850.
- [63] Derek Tseng et al. "Lensfree microscopy on a cellphone". In: *Lab on a Chip* 10.14 (2010). ISSN: 14730189. DOI: 10.1039/c003477k.
- [64] Onur Mudanyali et al. "Compact, light-weight and cost-effective microscope based on lensless incoherent holography for telemedicine applications". In: *Lab on a Chip* 10.11 (2010). ISSN: 14730189. DOI: 10.1039/c000453g.
- [65] Nathan C. Lindquist. "An Introduction to Lensless Digital Holographic Microscopy". In: 2018, pp. 147–170. DOI: 10.1007/978-3-319-64747-0_6.
- [66] Waheb Bishara et al. "Handheld, lensless microscope identifies malaria parasites". In: *SPIE Newsroom* (2011), pp. 10–12. ISSN: 18182259. DOI: 10.1117/2.1201107.003812.
- [67] Yichen Wu et al. "Demosaiced pixel super-resolution in digital holography for multiplexed computational color imaging on-a-chip (Conference Presentation)". In: 2017, p. 5. DOI: 10.1117/12.2251572.
- [68] John Rodenburg and Andrew Maiden. "Ptychography". In: *Springer Handbooks*. 2019, pp. 819–904. DOI: 10.1007/978-3-030-00069-1_17.

- [69] Yukio Takahashi et al. “High-resolution and high-sensitivity phase-contrast imaging by focused hard x-ray ptychography with a spatial filter”. In: *Applied Physics Letters* 102.9 (Mar. 2013), p. 5486. ISSN: 00036951. DOI: 10.1063/1.4794063.
- [70] Martin Dierolf et al. “Ptychographic X-ray computed tomography at the nanoscale”. In: *Nature* 467.7314 (Sept. 2010), pp. 436–439. ISSN: 0028-0836. DOI: 10.1038/nature09419.
- [71] Mirko Holler et al. “High-resolution non-destructive three-dimensional imaging of integrated circuits”. In: *Nature* 543.7645 (Mar. 2017), pp. 402–406. ISSN: 0028-0836. DOI: 10.1038/nature21698.
- [72] T. M. Godden et al. “Ptychographic microscope for three-dimensional imaging”. In: *Optics Express* 22.10 (May 2014), p. 12513. ISSN: 1094-4087. DOI: 10.1364/OE.22.012513.
- [73] Hutomo Suryo Wasisto et al. *Beyond solid-state lighting: Miniaturization, hybrid integration, and applications of GaN nano- and micro-LEDs*. Dec. 2019. DOI: 10.1063/1.5096322.
- [74] Martin Mikulics et al. “Nano-LED induced chemical reactions for structuring processes”. In: *Nanoscale Advances* 2.11 (2020). ISSN: 25160230. DOI: 10.1039/d0na00851f.

2

Components of the Nano Illumination Microscope

2.1. Introduction

NIM is based on scanning a sample by illuminating it successively with the different nano-LEDs of the array, mapping the amount of light reaching the sensor from each Light Emitting Diode (LED) to detect the presence of an object above them (and possibly other information such as the thickness). As such, NIM setups will need a way to capture the incoming light and store the signal received in order to rebuild and present it as a complete image frame once the scanning process is complete, as opposed to simply exposing the light received directly to the human eye.

The general architecture of the microscope can be seen in figure 2.1, with the light sources placed at the base and the sample immediately above them. The LEDs are kept at the base because the distance between sample and light source is critical for the operation of this microscope. Done this way, weight plays in favour of keeping the sample close. Above the sample and at a certain distance, the sensor will measure the light transmitted.

In this chapter, we present the components used or developed for creating the microscope, beginning with the development of a sensor camera specific for the NIM setup, which consisted of a SPAD camera. The intent behind it is to use it for low light detection since the LEDs were expected to be small and emit low intensity of light.

In later versions of the microscope, and in order to make the setups more flexible, we appreciated the benefits of using conventional CMOS cameras for their high resolutions since the LEDs emitted enough power to not make the single-photon detection capabilities of SPAD technology critical, as will be shown in later chapters.

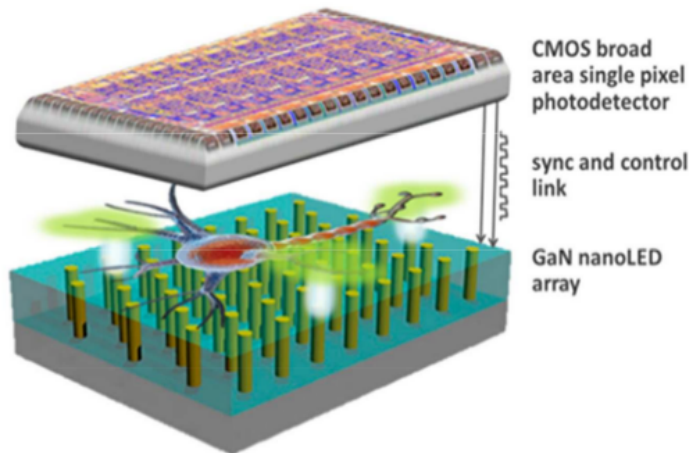


Figure 2.1: Schematic of the basic Nano Illumination Microscope (NIM) distribution

Another essential component of the microscopes that are presented are the light sources, the GaN nano-LED arrays. We will also introduce a brief overview of the state of the art in light source array fabrication and of the arrays used in this project. The LED arrays have been developed by the Technische Universität Braunschweig team of the Chipscope project, and the work done in this thesis consisted in creating the driving circuits and integrating them into the microscope.

2.2. SPAD sensors

While conventional Charge-Coupled Device (CCD) sensors offer quantum efficiencies of near 100% for wavelengths in the visible light range and have very small dark currents, their measurements become dominated by the readout noise, which is the noise in the readout amplifier that converts the captured charge from each pixel into a digital value. Even with extremely low readout rates to minimise the readout noise, it is still impossible to count photons (that is, to operate in photon starved conditions) since, at photon rates of one photon per reading, the contributed charge is lost in the readout noise [1].

These kinds of conditions are present in fluorescence experiments [2], as well as in astronomy observations [3]. In the context of this thesis, the μ LEDs and nanoLEDs were expected to produce low photon numbers, and that together with the possibility to explore fluorescence observations in NIM conditions, made it interesting to use devices ready to operate in photon starved conditions.

In the case of fluorescence based super-resolution microscopy, Electron Multiplying Charge-Coupled Devices (EMCCDs) have seen extensive use due to their high quantum efficiency and single-photon detection capabilities. EMCCDs are an improvement on CCD which incorporate amplification stages at the output of

each pixel. That allows running the sensor at higher frame rates, keeping the Signal-Noise Ratio (SNR) constant. Even then, the trade-off with output frame rate is still limiting the data output rate, at around 100 frames per second [4–7].

scientific CMOS (sCMOS) sensors directly address this problem, avoiding read-out noise entirely and thus allowing for much higher frame rates, with applications such as high-speed live-cell imaging [8], though their performance suffers in conditions of extremely low light [9].

SPADs based sensors are also a rising alternative, with constant research. Their extremely high gain allows each captured photon to be read as a digital signal, and so the readout noise is zero and they can offer more than 1000 fps [10], though they suffer from lower efficiency due to low fill factors.

Comparison shows how at low photon counts a commercial EMCCD obtains better results than a sCMOS camera [11]. Even more, when adding SPADs to the comparison, it is confirmed that both EMCCDs and SPADs sensors are better than sCMOSs sensors for photon starved applications [12].

Large SPAD arrays have been used in super-resolution microscopy [13], and works comparing it with an EMCCD camera showed location uncertainty is similar in both devices, though the EMCCD sensor was able to obtain better resolution [14].

A considerable advantage of SPAD sensors is that their swift response allows to use them in Time Correlated Single Photon Counting (TCSPC) measurements to observe, for example, the decay in fluorescence. Photon Multiplying Tube (PMT) devices can also be used for such measurements [2], but those devices are usually large, have to be operated in vacuum and require extremely high voltages, and are sensitive to magnetic fields around them, making their use difficult. On the other hand, the fabrication of SPADs sensors in CMOS processes [15] made it easy and inexpensive to integrate them and construct imaging arrays, to the point of being able to construct point-of-care devices [16] which use them.

This last characteristic is what brought us to implement the light-sensing device for the microscope as a SPAD: we expect to be able to study living samples in a low-cost setup. This requires fast acquisition times in low light conditions without creating vacuum conditions in the setup. At the same time, we needed flexibility to implement an imaging sensor capable of studying samples in a setup yet to be designed. The most flexible implementation is to use an array of sensors, a SPAD camera, which will allow to explore and locate the samples within the prototype. This concept is illustrated by figure 2.2, which schematically shows how the array contributes to locating LEDs and samples which might be of micrometre size. At the same time, having an array of sensors available will allow us to choose the one with the best characteristics for the measurement, and since it is custom made, we can access a single pixel instead of reading through the whole array, a design decision to try and further improve image acquisition speed.

The CMOS process node used to implement the device determines its perfor-

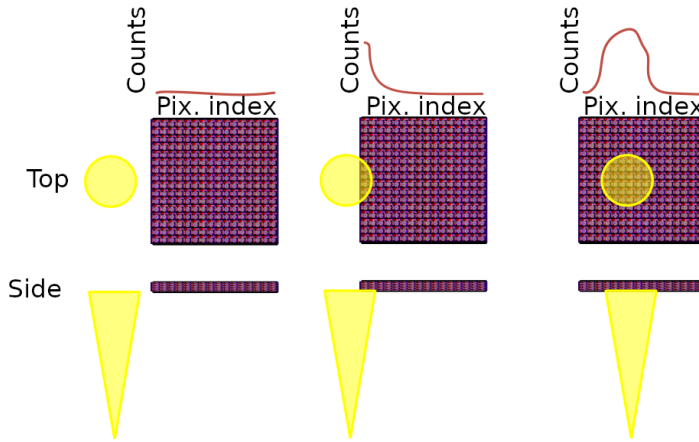


Figure 2.2: Schematic showing how the SPAD array can be used to locate the light cone from the nanoLEDs. Using a single sensor could mean long time for preparing the setup. With an array, any light captured allows for easy alignment.

mance and capabilities, such as how many of them can be integrated and how close, the dark noise of each pixel, and the photon detection probability. In this work, we have implemented a 16x16 SPAD camera in the 0.35 μm HV-CMOS process offered by Austria Micro-Systems (AMS). This chapter introduces the general aspects of SPAD sensors in imaging devices and goes on to explain the designed camera and its characterisation, as well as show some of its applications.

The reverse-biased p-n junctions operating as avalanche photo-diodes were developed already in the decade of 1960 [17, 18], but they remained as scientific curiosities until the properly developed SPAD sensors were implemented in a CMOS process in 2003 [15]. Compared to Avalanche Diodes, SPADs are specifically designed to operate above the avalanche breakdown voltage or Geiger mode, as shown at the left of figure 2.3, instead of simply in reverse bias. The schematic on the right of figure 2.3 shows the structure of the SPADs implemented in this work. While there are variations over it in the bibliography, the intent is the same: to create a depleted region of controlled size, which stabilises the electric field and keeps it free of impurities. When a photon or charged particle crosses through this depleted region of the p-n junction, it may be captured and ionise the material, generating an electron-hole pair. The high bias applied across the junction in these devices means that even such a single electron-hole pair will have enough energy to ionise several other atoms in the junction and thus create a self-sustaining avalanche of charge carriers of macroscopic magnitude. This avalanche builds up in picoseconds and thus can be used to time the arrival of the photons precisely [19]. It is also a digital signal, independent of the number of photons reaching the sensor or their wavelengths.

Once an avalanche is ongoing, the SPAD will require additional circuitry in or-

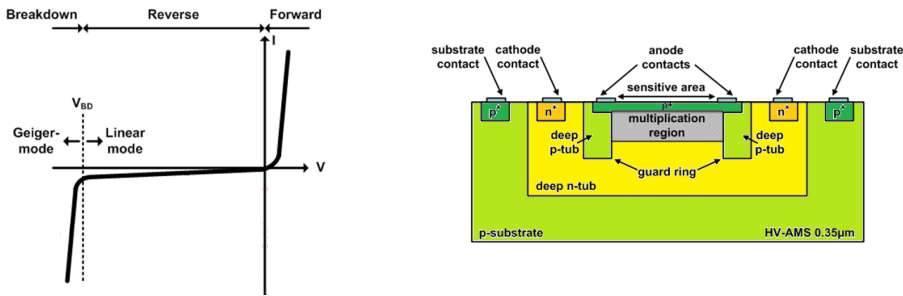


Figure 2.3: At the left, typical current / voltage relationship in a p-n junction. SPADs operate with a reverse bias putting them in Geiger mode. Right, schematic of the structure of the SPAD implemented in this work, as an example of a structure for the devices. Other combinations can be found in bibliography, but the approach is similar.

der to stop it and return to a sensitive state since the avalanche is self-sustaining. These avalanche quenching circuits lower the bias voltage through the junction at a value below breakdown, removing the energy available for the charge carriers so that they stop ionising the material. Even with the avalanche stopped, before the SPAD can sense again, the bias through the junction has to be restored to above the breakdown voltage V_{BD} . The quenching and recharge circuitry will have, thus, a critical role in the time the sensor is available for taking measurements.

Figure 2.4 shows two schematic examples of active (left) and passive (right) quenching strategies. Passive circuits can be used for the quenching process but are usually slower and offer less control [19–21]. Meanwhile, active circuits allow for a more controlled return of the sensor to a sensitive state, which helps avoid negative effects such as afterpulsing (see section 2.2.1.3) and reduce the time it takes for the SPAD to be capable of sensing again, the sensor dead time. For this reason, most SPAD based devices use active circuitry nowadays [22–26].

2.2.1. Figures of merit of SPADs

2.2.1.1. Dark count rate

Once the p-n junction of the SPAD is depleted and with a strong enough bias so that avalanches can be triggered, any free carrier in that region can trigger an avalanche. While the intended source of charge carriers is the absorption of photons, there are other unwanted sources. These unwanted sources constitute the noise of the SPAD sensor. Dark counts are the avalanches triggered by carriers not generated by the absorption of photons and are characterised as the mean rate of avalanches per second, or Dark Count Rate (DCR). It is an uncorrelated noise (not related to previous avalanches), contributed mainly by the thermal generation of carriers and band-to-band tunnelling, both things technological process dependant [15, 27].

The generation of an electron-hole pair consists of the transfer of the electron from the valence to the conduction band. The thermal excitation of electrons can

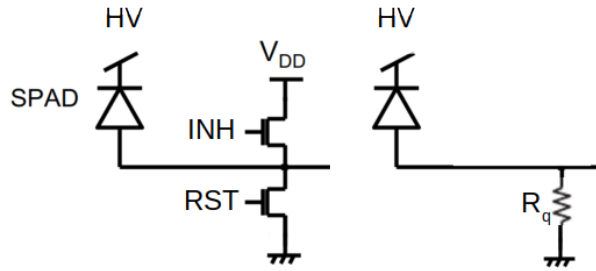


Figure 2.4: Schematics showing an example of active and passive quenching circuits. The schematic on the left corresponds to a pixel with active quenching. First, the INH transistor raises the voltage at the anode of the diode, reducing the voltage through it below breakdown. Then, the RST transistor restores the breakdown conditions. At the right, the schematic depicts a pixel with passive quenching. The resistor limits the current through the diode, avoiding damage on it and making the voltage at the anode charge until the avalanche stops. Then, the node discharges through the resistance until it is ready for breakdown again.

provide this energy. While intrinsic silicon has a large bandgap and thus the promotion of electrons is not efficient, the doping impurities act as intermediate band levels, enhancing this process. Therefore, the amount of thermal energy available for electron promotion is a significant factor in it, such that the thermal contribution to DCR has an exponential dependence with temperature [28].

The impurities in the lattice also help in the band-to-band tunnelling process since the tunnelling of an electron depends on the energy gap it has to cross, and impurities effectively reduce the material's bandgap. Electrons, then, may randomly tunnel up to the conduction band.

In a normal SPAD at room temperature, the main contribution to DCR is the thermal generation of carriers. DCR can then be lowered by the refrigeration of the sensor, though around 5°C it becomes equal to the tunnelling contribution, which has a very weak dependence with temperature. Other strategies can be explored to control the noise, such as designing the SPAD using special doping profiles [29–31]. Even then, in SPADs containing enough impurities inside the multiplication region, those become the primary source of charge carriers, to the point that the SPAD has a high probability of triggering each time it is enabled. Those are called hot pixels and are too noisy to be used for acquiring measurements, basically triggering an avalanche each time they are enabled [32, 33].

2.2.1.2. Dead Time

The SPAD dead time is the time required for the sensor to be sensitive again after an avalanche. The SPAD will not be sensitive to any radiation during that amount of time, which depending on the technology used, can vary from nanoseconds up to the microsecond time range. While the avalanche quenching electronics could play an important role in resetting the SPAD to its sensitive state, the dead time is usu-

ally a parameter to be decided as a trade-off with afterpulsing: longer dead times remove the charges trapped in the SPAD, lowering the noise from after-pulse triggered avalanches. This limitation is often the dominant component of dead time.

2.2.1.3. Afterpulsing

Afterpulsing is a source of noise in SPAD detectors. During an avalanche, some of the charge carriers going through the depletion region of the diode are captured by impurities in the semiconductor, called traps. These trapped charges can randomly obtain enough energy to be promoted back into the conductive band. This free charge will trigger a new avalanche if the sensor has been reset.

Afterpulsing depends strongly on the quality of the technological process and the actual layers of the CMOS chip used to implement the diode. It also depends on the number of charges crossing the depleted region in the avalanche: cutting the avalanche short using active quenching circuits reduces the number of charge carriers trapped [34]. Finally, afterpulsing is also affected by the parasitic capacitance in the avalanche source of the SPAD, which can be reduced through careful design [35].

2.2.1.4. Photon Detection Probability (PDP)

The Photon Detection Probability (PDP) is the probability that a photon crossing through the sensing device is captured and triggers an avalanche and is thus detected. It is usually expressed as equation 2.1, where P_a is the probability that a charge carrier generates an avalanche (as opposed to being trapped or absorbed too fast), FF is the fill-factor of the device, or the ratio of area sensitive to photons in the sensor as opposed to the total area. Finally, $QE(\lambda)$ is the quantum efficiency or ratio of electron-hole pairs generated by the total incident photons. It is a property intrinsic to the silicon with which the SPAD is fabricated, related to the energy needed to promote an electron from the valence to conduction band, and thus has a strong dependence with the wavelength (λ) of the incident photon.

$$PDP = P_a \cdot FF \cdot QE(\lambda) \quad (2.1)$$

The probability P_a that a charge carrier will trigger an avalanche increases with an increase on the reverse bias applied through the SPAD since that field provides energy to the charge carriers so that they can ionise atoms in the lattice, but it also increases the effects of the noise sources.

The PDP can also be determined experimentally by the relationship in equation 2.2, which requires being able to determine the photon flux through the detector, as well as being able to take into account any avalanches contributed by any noise source instead of photons.

$$PDP = \frac{\text{Number of avalanches} - \text{Number of noise avalanches}}{\text{Incident photons}} \quad (2.2)$$

2.2.1.5. Crosstalk

Crosstalk is a correlated noise appearing in arrays of SPADs, in which an avalanche is triggered by an avalanche taking place in another neighbouring pixel. This can happen due to the carriers generated in the avalanche diffusing to another SPAD through the semiconductor. Placing the pixels in isolated well areas with guard ring structures avoids this diffusion, though at the price of reducing the fill-factor of the array.

Another source of crosstalk is the generation of photons when an avalanche takes place, which may then be detected by other pixels. This process is dependent on the current during the avalanche. Beyond reducing the current and making the avalanche shorter, optical crosstalk can also be reduced with a proper design, for example including deep trenches between SPADs [36].

2.3. SPAD camera design

2.3.1. Design overview

The possibility that the nanoLED structures emitted a minimal quantity of light made it necessary to consider using single-photon capable sensors for the microscope. Since fluorescent samples were an open option, the use of SPAD sensors was an appropriate choice.

At the same time, it was evident that a single SPAD or even a linear array would not be practical for a microscope: while the NIM technique could be used with a single sensor, the alignment process of a sensor in the micrometre range with a particular zone of interest of the sample suggested it would be better to include an array. A 16×16 pixels camera was designed with all this in mind.

The camera was specifically designed to be used in a NIM microscope and thus to ensure a compact form factor. The natural way to do so was to keep all the PAD contacts with their bondings on the opposite side of the chip than the camera sensors since this would allow to keep the sensitive metal contacts away from the microscope structure and directly approaching the camera pixels.

Since reading the state of the whole array -if an avalanche has been received or not- is time-consuming and could affect the frame rate, the camera was designed with the capability to internally count the avalanches received and accumulate up to 255 per pixel before having to be read. When operating, the SPAD is enabled and avalanche capable for a fixed duration (called ON time), and after that time, it is moved out of breakdown conditions so that avalanches do not happen (OFF time). During the OFF time, since the diode is still polarised in reverse, charge carriers trapped in the depletion zone are removed by the electric field, which is important to avoid afterpulsing effects when the pixel is enabled again.

Since it is not possible to know the exact time within the ON time window at which an avalanche took place, the camera was designed with the possibility to support another operation mode: to directly couple a single SPAD from the array

to a dedicated output of the chip, with the intent of connecting it with a Field Programmable Gate Array (FPGA) implemented Time to Digital Converter (TDC) which had been previously implemented [37] in order to be able to measure exact photon time of arrival and thus reconstruct, for example, fluorescence decays for identifying fluorophores.

The process selected for the SPAD to be designed is a High Voltage $0.35\mu\text{m}$ process from Austria MicroSystems, due to the expected low noise of sensors implemented in such process, as documented extensively in the bibliography, with DCR noise below $10^4 \frac{\text{KHz}}{\text{mm}^2}$ [38–41].

Figure 2.5 shows the fabricated ASIC once received. The chip is $2.93 \times 1.98\text{mm}^2$ in size, and shown are the SPAD array camera and the test structures included for characterisation purposes and the internal circuitry are shown.

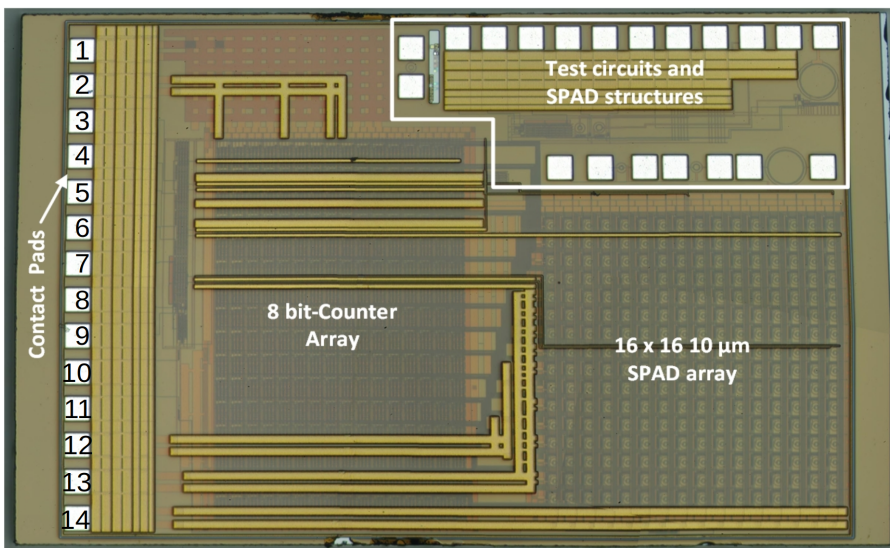


Figure 2.5: Photography of the fabricated SPAD array camera chip, with the included test structures enclosed by the white border. The SPAD array and the counter can be seen under and around the corresponding labels. The signal pads for the camera are numbered and are detailed in table 2.1.

2.3.1.1. Camera architecture and operation

The camera is composed of an array of 16×16 circular SPADs of $10\mu\text{m}$ of diameter and a pitch of $70\mu\text{m}$, with the outputs connected as rolling shutter. Each pixel has its digital readout logic connected to an 8-bit counter, forming an array that has each register connected in a chain to read out the results stored in the counters. All the pads used to control the camera are distributed to one side of the chip (left in figure 2.5) so that the SPAD array can be on the opposed edge, to ease the inclusion of the chip into NIM setups, as will be presented in the next chapter. Figure 2.6 shows a schematic of the overall architecture of the SPAD camera. The principal

Pin	Name	I/O	Description
1	GND	S	Ground
2	VDD	S	Supply 3.3V
3	SCAN_TEST	I	SCAN Data input for pixel configuration
4	SCAN_EN	I	SCAN ENABLE signal for camera
5	SYS_RST	I	System RESET
6	CLK	I	Clock for camera operation
7	RST_EXT	I	External RST signal for SPADS
8	SEL	I	External / Internal SPAD control selection
9	INH_EXT	I	External INH signal for SPADs
10	SCAN_OUT	O	Counter Matrix Scan Output (for camera mode)
11	TDC_OUT	O	Summed Anodes output for TDC measure
12	VDD	S	Supply 3.3V
13	GND	S	Ground
14	HV	S	HV for the pixel matrix

Table 2.1: Input and Output signals table for the ASIC of the SPAD camera, with pins numbered as indicated in figure 2.5. S in the I/O column indicates the pad is for a Supply Voltage, not a signal.

interconnections and the logic used to select the operation modes are indicated, which are detailed below.

The readout and the counters of the camera have four modes of operation implemented, detailed below and shown graphically in the waveforms in figure 2.7:

- **Pixel configuration:** this mode reads external data into the camera, setting the active or inactive state of each individual SPAD of the array, used to activate only a part of the camera or kill noisy pixels. Controlled by the SCAN_EN signal in high, and represented by letter C in figure 2.7.
- **TDC operation:** this mode ignores the counters in the camera. Normally used with only one pixel active, the output of the pixel readout circuitry is sent out of the chip directly so that the time of arrival of each avalanche can be measured by an external TDC, presented by letter D for OPCODE in 2.7.
- **Camera operation:** in this mode, the avalanche counters are active and increase with each received hit. It requires the external CLK to be inactive and is shown by letter E in figure 2.7.
- **Counter read:** this is the operation mode used to read the counters and output their data from the chip. The first bit to be read is the most significant bit of the last pixel of the camera (number 255). Its value is always set at the output, even before any CLK cycle or enabling has taken place. The counters store the data in big-endian representation and rolling shutter order. 2047 CLK cycles

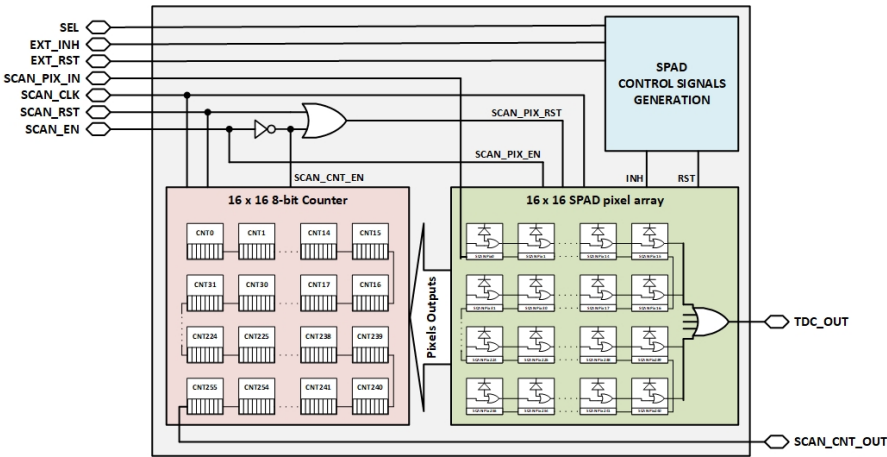


Figure 2.6: Schematic of the general SPAD camera architecture and main internal connections and the logic used for the control signals. Each SPAD circuit (on the right of the image, in green) connects with the corresponding 8-bit counter (left side / red section).

are required in order to read the entire camera, and `SCAN_EN` has to be at low level, as shown under `OPMODE F` in figure 2.7.

During the TDC or camera operations, the FPGA has to generate the SPAD driving signals detailed in the following sections (in figure 2.8). Since the results from camera operation mode are accumulated in an 8 bit counter, to ensure the counters do not overflow, the SPADs should only be triggered 255 times before reading the counter scan chain. This process can be repeated as many times as necessary to obtain an adequately populated measurement, depending on the desired dynamic range. For 8 bits range, typically, ten measurement blocks would be needed, a total of 2560 SPAD measurements. Since a typical measurement will complete in 200 ns, the entire experiment would take 512 μ s in active SPAD time. The overhead added by having to read and reset the counter matrix every 255 measurements has to be added to this time. Typically clocked at 100 MHz, a single read of the entire camera requires 20.48 μ s and as said, ten blocks are required for the entire matrix, adding a total 205 μ s.

If the experiment allows using a small subset of pixels from the camera (preferably a single one, as is the case for NIM measurements), the TDC operation mode can be used instead. In this mode, the detected avalanches bypass the counters entirely and are directed towards the `TDC_OUT` pad. The TDC circuit must be provided externally. In our case, we used a previously developed FPGA solution [37]. Since this external TDC can accumulate an arbitrarily large number of counts, the overhead caused by reading the counters disappears. The TDC also offers information on the time of arrival of the photons with a resolution of 70 ps.

The fine control on the timings of the camera signals allows applying a dynamic

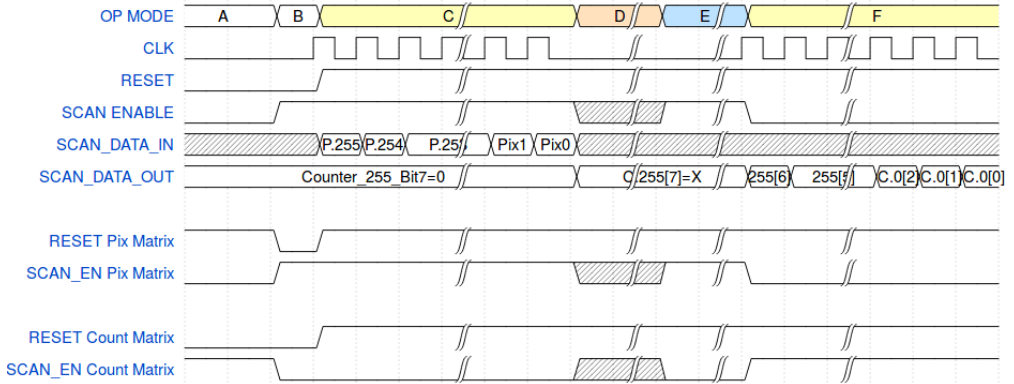


Figure 2.7: Timing diagrams for the control signals and the operation modes of the camera. The general operation mode is indicated by OP MODE: A, initial idle state. B, camera reset. C, pixel configuration. D, TDC operation. E, camera operation. F counter read operation.

range enhancement technique consisting of a linear addition of the number of avalanches detected with different measurement windows (TON). Longer measurement windows are necessary for weak emissions or situations with a small number of photons, but using this same window might saturate the sensor in the presence of a more intense light source. Combining the measurements obtained from both allows having the information on both situations, extending the dynamic range of the camera [42]. This has been successfully applied with this camera in a miniature point-of-care device capable of performing intensity and time-resolved measurements of fluorescent tags, which was validated for the detection of plasmodium antigen (a biomarker of malaria infection) [43].

2.3.2. SPAD and readout circuit design

As introduced before, active quenching of the avalanche in the SPAD offers better control and reduces the dead time of the sensor, and is the strategy followed in this design: the control of each SPAD is done by two signals, INH (for inhibit) and RST (for reset). A wave diagram showing the general operation of the circuit is shown in figure 2.8: a low level in the INH signal reduces the bias through the SPAD below the Geiger region of operation, leaving it deactivated since it charges the anode node of the SPAD to the voltage level of the power source. Meanwhile, a high logical level in the RST signal discharges the anode node, returning the pixel to a sensitive state. When an avalanche occurs, the current from it charges the anode node, increasing the voltage to a certain level. This voltage level is called *overvoltage*, further explained in the following paragraphs. Even if no avalanche has been detected, the measurement might be stopped externally at any time. This is done by setting the INH signal to a low logical level, which in addition to charging the anode node, also sets the output of the pixel to a logical low level.

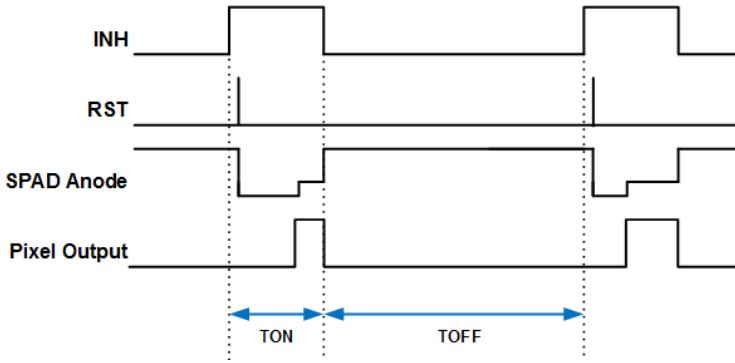


Figure 2.8: Waveform of the SPAD control signals. Independently of the state of the SPAD anode, INH to 0 will set it to a high logical level, while the short RST pulse discharges it to ground. The Output pixel signal is the wave from the output register.

The operation of the SPAD readout is better understood with the schematic shown in figure 2.9. The HV on the cathode of the SPAD refers to the High Voltage, the negative voltage level biasing the device on or near the breakdown region of operation. For this technology, breakdown occurs at -19.5 V. At higher voltages, the field through the device is not strong enough to ionise charges in the diode and produce avalanches. When an avalanche finally takes place, the anode node quickly charges up until the overvoltage level, which is the voltage above the breakdown threshold at which HV is polarised, since beyond that point, the potential through the SPAD is below breakdown, and the avalanche quenches. This limits the maximum HV usable in this camera to about 23 V, which would set the anode at 3.5 V, at the limit of burning the non-HV, 3.3 V powered devices used at the rest of the circuit.

As explained before, the INH PMOS transistor, shown in figure 2.9 as M_1 , has the function of deactivating the SPAD by charging the anode up with the 3.3 V of the VDD source. Doing so is useful after an avalanche to keep the SPAD inactive and clear the charges trapped in its depletion layer. The dimensions of this transistor have been set at $\frac{W}{L} = \frac{3\mu\text{m}}{0.4\mu\text{m}}$. These dimensions allow charging the anode node in less than three nanoseconds once open, allowing for precise circuit control.

Meanwhile, the RST transistor (M_2 in figure 2.9) is critical for the correct operation of the device. This is because the pixel will become sensitive to light when the bias across it becomes higher than the breakdown voltage. Any avalanche taking place while the RST transistor is open will thus be a potentially destructive short-circuit, making it impossible to determine the exact time of arrival of the photon. Due to that, the RST transistor has been designed with the condition of it being able to discharge the anode node in 300 ps, for which 3 NMOS transistors with $\frac{W}{L} = \frac{8\mu\text{m}}{0.4\mu\text{m}}$ each have been used after calculating the parasitical capacitances of the node.

Finally, a buffer (BF in figure 2.9) isolates the SPAD anode from the rest of the readout. This is done to reduce the capacitance at the node, which helps reduce

the sensor's noise and properly detect the avalanche. The buffer has been custom designed to minimise the threshold tension down to $V_T = 909mV$, a critical parameter since this will be the minimum overvoltage that can be used with these pixels. To do so, with both inverters having $L = L_{\min} = 0.35\mu m$, the widths are $W_p = 0.4\mu m$ and $W_n = 2\mu m$ for the first one and a more balanced $W_p = 2\mu m$ and $W_n = 0.8\mu m$ for the second. The propagation delay is one nanosecond, but this is not critical for timing since this value is constant and thus can be characterised as an offset to all measurements.

In order to store and propagate the avalanche, the output from the buffer is used as the clock signal for a register. This register has a constant high logical level as the data input and uses the INH signal as a reset: with INH at a low level, and thus the pixel deactivated, the register is reset and inactive. The faster switching of the reset transistors also eliminates the possibility of registering avalanches just out of the operation window or the result of the anode charging thanks precisely to the commutation of the INH signal.

In order to be able to select if individual pixels are on or off, a register chain is included. Each register stores the active or inactive status of the corresponding readout circuit and thus pixel from the camera, keeping the INH and RST signals at 0 when inactive through an AND gate, as can be seen in figure 2.9. The register receives the scan data from the previous pixel in the array, except for the first flip-flop of the chain, which gets the data from the corresponding chip pad. The output of each register is sent to the data input of the next one and used to enable or disable the pixel.

A set of buffers is also included for driving the INH and RST signals. While the INH signal is again less critical, the RST attacks large gates and has a strict timing constraint. As such, and to keep the delay on both signals synchronised, INH only uses a single force one inverter while the RST signal is buffered through a chain of up to force eight inverters.

In addition to the output from the readout circuit, each pixel has an additional output consisting of the OR operation between that readout output value and the one from previous circuits. This output is used to connect all the pixel readouts in the camera to a single output pad without adding other circuitry, allowing access to the arrival time of the avalanche. This information would not be accessible through the registered output since the counters can only accumulate the number of avalanches but cannot track the time of arrival. The aim is for this output to be connected to an external TDC, implemented in the device controlling the camera.

The SPAD structure implemented in this work has been introduced in the cross-section of figure 2.3 and is P+ anode over N cathode with a guard ring in a design inspired on previous work by the group [44]. The pixels have been designed with a circular shape to avoid sharp edges, where the field gradient becomes more intense and can then promote avalanches, increasing the noise in the sensor [45].

Figure 2.10 a) shows the layout taken from the Cadence design software. The

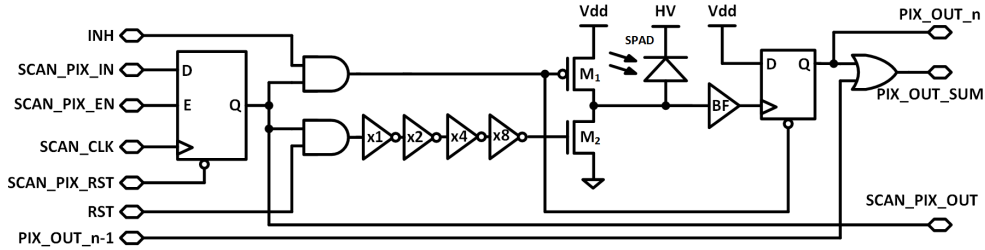


Figure 2.9: Schematic of the SPAD and its control and readout circuit, as well as the corresponding SCAN register used to disable or enable the pixel

SPAD itself is the green circular area at the centre of the image, surrounded by the ring of anode contacts. The second ring consists of the N+ doped area, which forms the cathode of the diode. The most external ring is the one making the isolating substrate contacts. In the same figure, along the borders of the SPAD can be seen the read circuitry as pictured in figure 2.9. Highlighted in red is the scan register, which selects if the pixel will be enabled or not. The buffers and enabling NAND for the RST and INH signals are in yellow. In green, the INH and RST transistors at the anode of the SPAD. The area highlighted in white shows the output buffer, followed in orange by the output register. The last area, marked in blue, consists of the OR gate to sum the avalanche status of the pixel with the previous ones of the same row.

At the same time, 2.10 b) shows a micro-photography of two of the SPADs of the array taken from the fabricated chip. Marked in red is the diameter of the central sensitive area, as well as the 70 μm pitch between pixels.

Besides the pixels for the camera, several test structures were also included in the first iteration of the chip, as shown in figure 2.5 in order to characterise the new designs and study the feasibility of new ones, such as bigger SPADs (20 μm and 130 μm diameter SPADs), with the same basic design. The 130 μm SPADs were interesting to try and implement a single large sensor to integrate the signal received from the whole LED array, but it proved to be too large for the technological process. Its large size meant it contained more than a single impurity, making it set off an avalanche from the very moment it was enabled.

2.3.3. Matrix structure

The matrix is organised in 16 rows, each containing 16 pixels. Figure 2.11 shows one of those rows. Each PIXEL_OUT is an output for the matrix, which the counters will register and increase the number they are storing. SCAN_OUT corresponds to the output of the configuration register chain. It connects into the SCAN_IN input of the next pixel in the row, as does the PIXEL_SUM_OUT. Each row has the initial PREV_PIX connected to GND. The last PIXEL_SUM_OUT signal of the row connects into an OR tree which provides said operation for all rows of the camera before con-

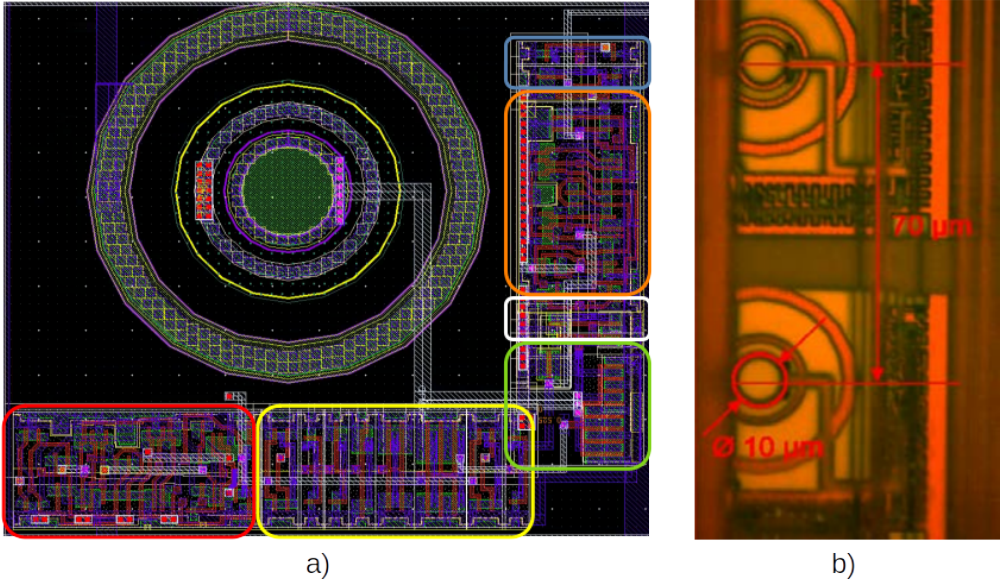


Figure 2.10: a) Capture of the spad layout (circular structure at the centre) and readout circuits, highlighted in colour for reference. b) Micro-photography of two SPADs and their circuits, with the diameter and distance between pixels indicated.

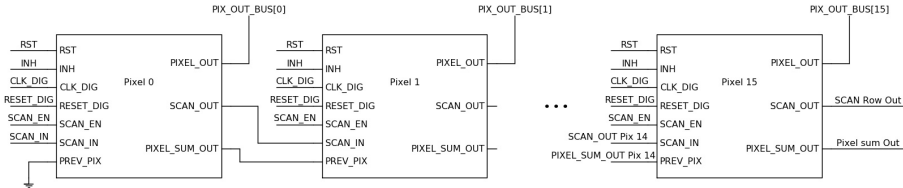


Figure 2.11: Schematic for a row of the SPAD camera, showing an overview of its interconnections.

necting directly to an output pad, providing a fast path to detect avalanches outside the chip beyond accumulating them on the counters.

The configuration SCAN chain connects each row and is finally left floating at the last row since there is no interest in recovering any configuration data.

2.3.4. Counter Matrix

The 8-bit up counter in charge of tracking the number of avalanches received is implemented through standard JK flip-flops with SCAN support. The SCAN enable signal, in addition to enabling the corresponding SCAN inputs of each flip-flop, also selects what clock drives the counter: the external digital clock or the signal coming from each pixel output. When the external clock mode is selected (SCAN enabled), the value of each FF passes to the next one following the SCAN chain, and thus the data can be read. Otherwise, the counter will increase its value with each high level

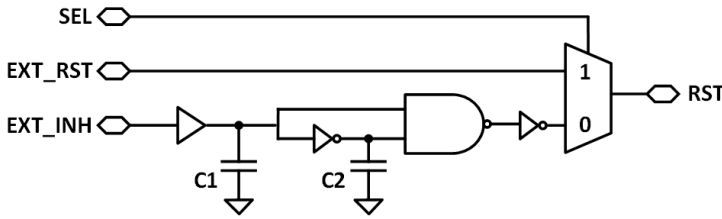


Figure 2.12: Schematic of the RST signal generator showing the distribution of the capacitances to generate delays and the selection logic

arriving from the pixel readout.

2.3.5. Internal control signal generation

While the camera requires the support of an external driving element (a FPGA), previous work [37] has shown that the correct timing of the SPAD control signals is critical. The best way to keep the control signals controlled and maintain their integrity is to generate them internally on-chip instead of sending them through a Printed Circuit Board (PCB) board and cables from an external driving circuit such as an FPGA. At the same time, for the camera to be part of a microscope with a small form factor, it is helpful to explore the possibility of removing the dependence on the FPGA entirely.

To begin exploring the exposed possibilities, we included an internal control signal generator in the design, which can be enabled or disabled as required by using the SEL input signal. Once enabled with SEL high, this circuit requires only a trigger signal to generate both INH and RST signals for the SPADs. This trigger signal is taken from the INH pad.

2.3.5.1. Internal RST signal generation

The FPGA used for the test, a Zynq-7020, could not provide a pulse to the chip shorter than 1.6 ns. This is especially critical for the RST signal pulse because it having such a shape means that the SPAD cannot capture information during the 1.6 nanosecond window at the beginning of each measurement window. Making the RST signal as short as possible is then desirable, and the best option for doing so is to generate it internally in the chip.

Generation of the RST signal is done through a buffer chain with added capacitances to introduce the desired delays, together with a NAND logic gate to generate the pulse itself. The circuit is shown in figure 2.12, in which C1 and the buffers before it (the picture shows a single buffer to summarise the buffer chain) set the delay between the RST signal and the rising flank of the INH signal, and C2 sets the duration of the pulse. The circuit generates pulses 500 ps long Full Width at Half Maximum (FWHM) that begin 1.6 ns after the rising flank of the INH signal to give time to all the INH transistors to close and avoid short-circuits in the readout.

2.3.5.2. Internal INH signal generation

The precise timing feasible with internal signals is intended to be used in applications such as measuring fluorescence lifetimes from biological fluorophores, which usually are very short. We use a variation of the circuit shown in figure 2.12 to generate the short on-time windows, adjusted to generate INH pulses lasting 12 ns and without C1 capacitance, since delaying the beginning of the pulse has no interest. This means the active measurement window, or TON, has a fixed duration of 10 ns: the 12 ns of the INH pulse minus the 1.6 ns delay of the RST signal and its width. Since the starting time of the TON window is controlled by the trigger, it can be synchronised (and even delayed) with an external light source providing the illumination.

2.4. Camera Characterization

PCBs were designed to adapt the camera chip with an external controller, in this case a Zynq-7020 System on Chip (SoC) FPGA from Xilinx mounted in a development board. This FPGA generates all the input signals to the chip, reads the results from the stored memories, and also includes a TDC for time-of-flight measurements. The SoC interfaces the FPGA with a USB (or Ethernet) connection to a PC where the user can control the measurement and study the results. Further detail of the FPGA and the boards interfacing with it will be given in the next chapter since it is part of the development of the microscope prototypes.

Meanwhile, the general setup used to characterise can be seen in figure 2.13, where the components used in general to test the SPAD camera are shown. This same setup remained basically the same while building the initial microscope versions, only switching to more compact devices once the basic requirements for the microscope were settled. This evolution is shown in the following chapters.

In the setup shown in figure 2.13, the optical bench is important to absorb ambient vibrations and keep the system stable. This becomes important when working with positioning stages and distances at the micron scale or below. In addition, given the SPADs' sensitivity to light, it is necessary to enclose the experiments in a dark environment. We do that with the box shown, which has tubes for interfacing the cables, filled with foam to avoid any light entering through them.

The initial tests carried out were the electrical ones, done in the test structures on the chip to measure the voltage at which the avalanche took place. The $10\mu\text{m}$ diameter SPADs go into breakdown at a HV of 19 V. This allowed us to design the PCBs with internal biasing control around this voltage for the next iteration of designs.

As explained before, the tension above the 19 V is the overvoltage, and it is the level at which the internal anode node will charge once the avalanche takes place. For the avalanche to be detected, the overvoltage has to be higher than the threshold voltage of the buffer in the readout circuit. Therefore, we designed the buffer to minimise the input threshold to increase the readout range as much as possible.

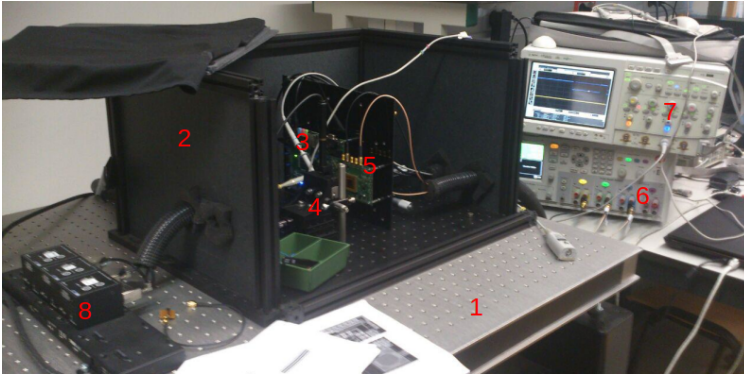


Figure 2.13: Experimental setup for the characterisation of the SPAD camera, with the relevant elements numbered. 1) Optical bench; 2) Black box with foam blocked holes for cables; 3) FPGA board; 4) Positioning stages; 5) Camera PCB board; 6) Power supply unit; 7) Oscilloscope; 8) Piezoelectric positioning stage motors.

At the same time, the overvoltage cannot be higher than the maximum voltage the gate of the transistors can take, which is a bit more than 3.3 V. Care is necessary to ensure that the SPAD is never biased above 23 V.

2.4.1. Dark count rate

The DCR of the camera is characterised each time a new chip is to be used in any experiment by taking millions of measurements with the whole SPAD array in dark conditions. The frequency of avalanches, the number of detected events per second, is the Dark Count Rate. Figure 2.14 shows the cumulative plot of the DCR for two different over-voltages, 1.0 V and 1.3 V, at room temperature, obtained with the cumulative results of different chips. The DCR is below 1 kHz for 90% of the pixels for both overvoltages. Therefore, the absolute minimum noise for the 1.3 V overvoltage is 300 Hz for this array. This noise level is in agreement with the literature for this technology [46], and translates to $3.8 \cdot 10^3 \frac{\text{kHz}}{\text{mm}^2}$, on the low end for noise in this technological node. Meanwhile, figure 2.15 shows the distribution of dark count noise at room temperature on a specific camera chip. Both representations show the same information: the typical dark counts of each pixel on the 16×16 pixels array. On the left, this figure is presented as a heat map, and on the right, the noise level is shown as the height of the columns (cut when above 2000 counts for clarity). The hot pixels are easily identified and usually avoided entirely when taking measurements with the camera since they are saturated and usually do not offer any useful information while distorting image representations if not careful.

2.4.2. Photon Detection Probability

The PDP was measured in an experimental setup consisting of a white-light lamp with a monochromator at the output. The device allows for the wavelength of emis-

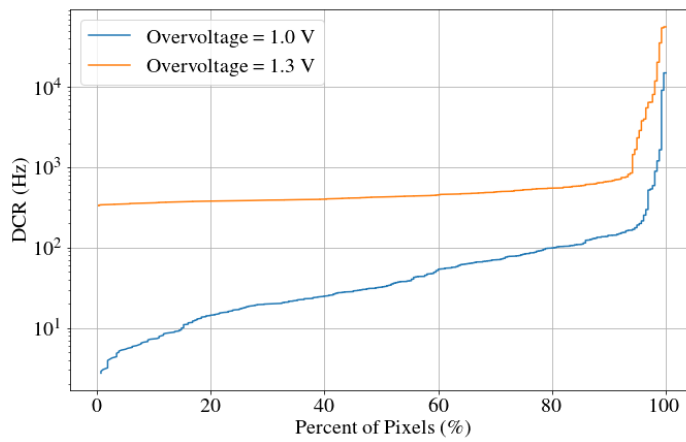


Figure 2.14: Dark count rate statistical distribution across SPAD pixels, measured at 1V and 1.3V of overvoltage.

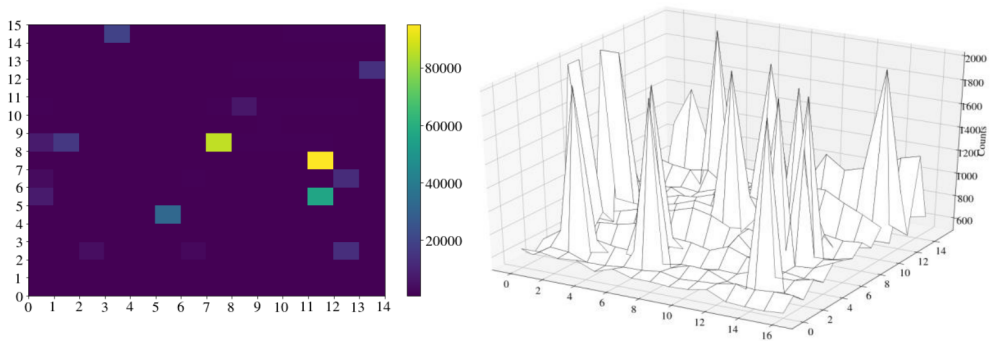


Figure 2.15: Dark count rate distribution across the SPAD pixels of a single camera, measured at 1.3V of overvoltage. Presented as a heat map with the number of counts at the left and a heightmap on the right side.

sion to be selected, and the experiment consisted of sweeping through wavelengths illuminating the sensor. Figure 2.16 a) shows the PDP of a SPAD in the wavelength of interest, between 300 and 1000 nm, and at two different overvoltages, at room temperature. The measured PDP is lower than expected for the $0.35\mu\text{m}$ technological process, which is usually around 30%, but similar values are found in the bibliography [46].

The cause for such low PDP is that the AMS HV process covers the chip in a polyimide layer for protection. This was validated by applying a plasma etching process on the chip surface, removing the protection layer and repeating the experiment. As it can be seen in figure 2.16 b), the sensor becomes three times more sensitive, which sets the PDP around the expected 30%. Future iterations of the camera chip can be requested without polyimide for increased sensitivity, though at the price of more fragility, and so for the construction of the microscopes, the normal process, with the protection layer, will be used.

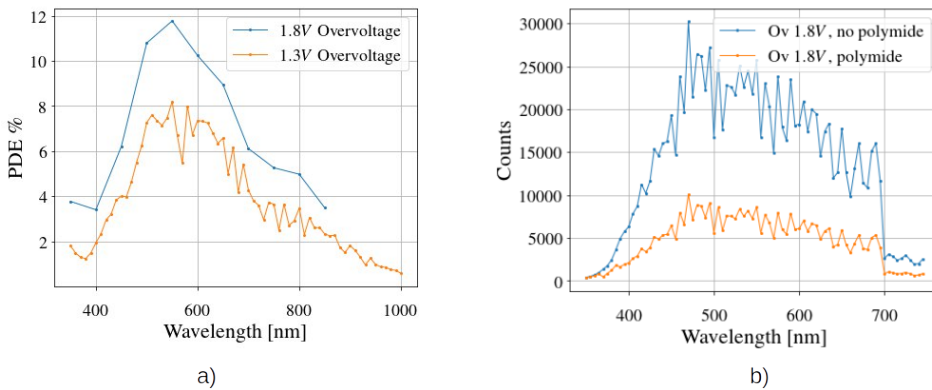


Figure 2.16: a) Photon Detection Probability as a function of the wavelength for the $10\mu\text{m}$ SPAD implemented, at 1.3 V and 1.8 V overvoltages. b) Comparison of the detection capabilities on the same sensor with and without polyimide chip protection.

2.4.3. Afterpulsing

Afterpulsing, as explained before, is a result of the charges lingering in the depleted area of the diode, but the trapped carriers can be removed by keeping the device polarised without enough field to generate avalanches. The natural way of doing so with the circuit developed is by making the TOFF longer.

Avalanches contributed by afterpulsing are correlated noise and can be characterised with the same setup and procedure as with dark count noise done before. This has been done for different SPAD off times to obtain figure 2.17. For short TOFF times, the trapped charges have not been cleaned by the device bias, and so they have a high probability of suddenly promoting into the conduction bands when the SPAD is ready to capture a photon, causing an avalanche. The figure shows the DCR

level as a function of the TOFF allowed in ns. The baseline dark noise level is given by the Noise level line. As it can be seen, the probability descends quite fast with TOFF: for practical uses, in most measurements, we use TOFFs of 200 ns to keep this time from dominating the measurement time, since using this time only increases the noise by 1%. Getting rid of that small percentage requires extending each individual measurement by more than a factor of 10, significantly increasing the total duration of a measurement. Ultimately, the experiment to be done will determine what compromise is tolerable: shorter TOFFs and thus higher frame rates at the price of higher noise count, for example, in scanning microscopy measurements, or a more precise number of counts allowing for more extended measurements, which might be the case in non-live fluorescence measurements.

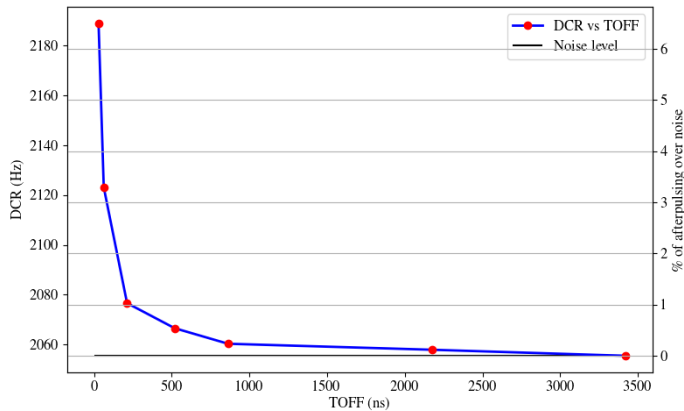


Figure 2.17: Afterpulsing as a function of the off time (TOFF) allowed at each measurement, as well as the noise baseline and the percentage above it

2.4.4. SPAD response calibration

Given the number of SPADs (256) in the camera and their distribution along the chip, lattice defects and fluctuations in the doping profile introduce variations in the DCR and PDP [47]. Furthermore, the different doping also causes a non-linear and changing response to the intensity of light captured by each pixel of the array, which would affect the quality of the resulting frame captured by the sensor, since each pixel would report a different intensity (or number of photon avalanches after a given time) to a uniform exposition to light.

This response can be corrected through a calibration process. This process consists of adding a controlled light source to the setup previously used to characterise the dark noise of the camera array. The light source must illuminate the camera homogeneously, a requirement easily satisfied by adding an LED at a distance from the 1×1 mm camera. Frames are then captured for different illuminations, starting from entirely dark conditions up to saturation. The curves obtained differ not only

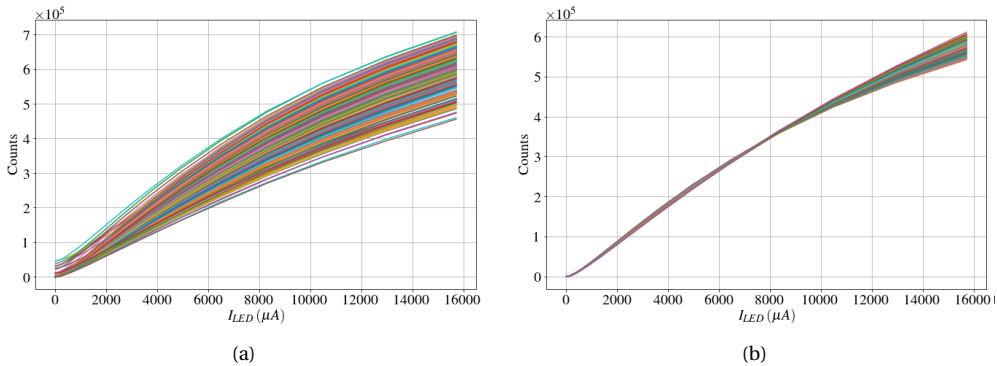


Figure 2.18: Calibration of the SPAD camera. The figures show the number of counts read by each SPAD of the camera as a function of the current through a LED. In a), the raw reading are shown. In b), each SPAD is corrected to the mean response (after removing hot pixels).

at the starting point (the differences in dark count rates presented before) but also on the response to the light, meaning each pixel presents a different gain. With the response of each camera pixel known, look-up tables can be elaborated for each one to equalise their response to the average one [48].

Figure 2.18 shows the response of all the pixels of the camera without calibration in 2.18a and the final result of applying the calibration process in 2.18b.

2.5. LED arrays

The other main component of NIM microscopy is the illumination source, in the form of an array of individual light sources. The size and arrangement of each microLED are critical for the correct operation of the microscope, as will be discussed in the next chapter.

Meanwhile, we will offer a short overview of display technology, presenting the trend towards smaller display devices that will benefit this microscopy technique. After the overview, more attention is paid to GaN micro/nano LEDs, which are the light sources used in this microscope.

2.5.1. Introduction to display technologies

Displays are a vital part of our lives: this work is being written thanks to one, it will probably be read in another, and in general, during a regular day we lay eyes on plenty of them, and this is a trend which certainly is not changing. Moreover, new devices that include a display are continuously being added into our lives [49–51].

The predominant display technology since the beginning of the century has been Liquid Crystal Display (LCD), invented in the decade of the 1970 [52]. Characteristics such as a flat design, low weight, low driving voltage, design flexibility and low power consumption (at least in reflection-based displays) made them surpass

the previously used CRT technology [53], and are still the benchmark against which new display technologies are measured. Far from being replaced, LCD is still widely used in general display applications [54].

Display technologies, in all their versions, are being pushed into higher integration to provide high Pixels Per Inch (PPI) for mobile phones [55] and more recently for virtual or augmented reality applications [56]. Smaller pixels immediately allow for higher resolutions without increasing the device size, so the current development of the display technology is pushing it towards a favourable direction for the application developed in this thesis: large LED arrays of smaller pixels. For LCD, recent results report a 4K resolution LCD with 1058 PPI [57], though larger PPI have been reported for lesser resolutions [58].

Despite those good characteristics, LCDs are, after all, a passive technology and require a backlight or an external illumination source like the sun for displays. This light source adds to the total device thickness and limits the flexibility of the design. This opened the way for different technologies to develop in parallel and challenge LCD capabilities, even taking its place in specific applications.

The main competition to LCD in displays comes from the OLED technology, especially on screens for mobile devices since they have thinner and more flexible substrates [59]. In general terms, OLED displays have better response speed [60], are thinner and have better black contrast than LCDs, but on the other hand, they are less bright, degrade faster and still are more expensive to manufacture [60–63].

An OLED is an LED in which the emissive layer is an organic compound that emits light in response to electric current, situated between the anode and the cathode. The basic structure of an OLED can be seen in figure 2.19. When forward polarised, charge carriers move through the transport layer through a hopping mechanism and meet in the emission layer, where they have a chance to recombine into a high energy state called an exciton. After a characteristic lifetime, the exciton emits light. While this process is similar to that of inorganic LEDs, the mechanisms are different. The charge carriers in inorganic devices are described by band theory applied on the semiconductor crystal, which does not apply to the disordered layers of the organic molecules.

For emission to be efficient, the Hole Injection Layer (HIL) must ease the injection of holes into the Hole Transport Layer. This layer must have high hole mobility while keeping the electrons from reaching the anode. The equivalent requirements are in place for the Electron Transport and Electron Injection Layers (ETL and EIL). Additionally, the organic layers must have high transmittivity in the emission wavelength to ensure the photons are not absorbed. Finally, at least one of the electrodes must be transparent to extract the light efficiently. In many cases, Indium-Tin Oxide (ITO) is used for it [64].

The highest integration reported for OLED displays is for an array of 1920×1080 pixels with a PPI of 5644, an effective pixel size of $4.5 \mu\text{m}$ [65]. Other similar integration examples are the demonstration of a smaller array with 5291 PPI [66].

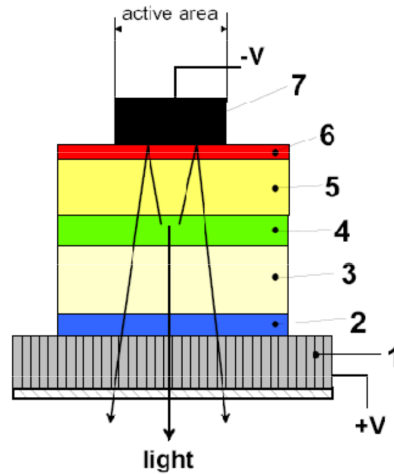


Figure 2.19: Diagram with the layer structure of a single OLED. The layers are 1) Substrate and anode; 2) Hole Injection Layer (HIL); 3) Hole Transport Layer (HTL); 4) Emission Layer (EML); 5) Electron Transport Layer (ETL); 6) Electron Injection Layer (EIL); 7) Cathode.

Finally, micro-LEDs are a growing alternative to compete with OLED for general microdisplay applications [67]. They possess the same advantages over LCDs than OLED technology but improve over these in all the weak aspects for OLEDs, such as presenting much higher brightness, response times and lifetimes, as well as higher integration (with some demonstrations as high as 10000 PPI or pixels of $2.54\ \mu\text{m}$) [68].

GaN crystals for the fabrication of blue-emitting LEDs are synthesised at high temperatures and with the help of a chemical reaction between ammonia (as the nitrogen source) [69] and using sapphire as substrate material since it interacts weakly with ammonia [70].

The first GaN LEDs, with very limited efficiency, were developed at the beginning of the 1970 decade [71], but they were not successful despite efforts to commercialise them done by companies [72, 73]. It was not until the second half of the 1980 decade that GaN growth would have its first breakthroughs paving the way towards efficient p-n junction LEDs [74]. However, it took a few years to develop the adequate methodology for p-GaN growth using thermal annealing, finally offering the first p-n GaN LEDs [75]. Soon after followed the first single-quantum-well LEDs, an important step to improve the efficiency of nitride LEDs [76].

GaN-based micro-LEDs are the field of expertise of the team at the Technische Universität Braunschweig, a partner in the Chipscope European Project in charge of developing the illumination sources. The GaN LED technology will be briefly introduced, as will the key developments within the project.

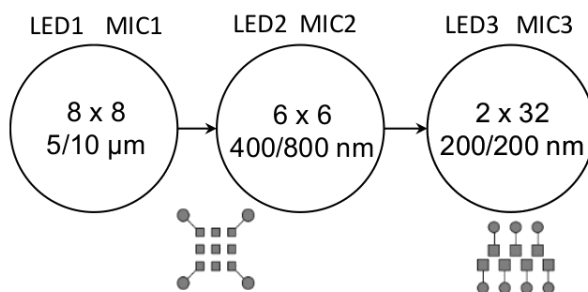


Figure 2.20: Evolution of the LEDs used in the Chipscope European project and in this work for integrating into the microscopes. Each step shows the form factor of the LED array and the dimensions of the LED / the pitch on each matrix.

2.5.2. Towards nanoLEDs arrays for NIM microscopy

The microLED (and in the later iterations, nanoLED) used to develop the NIM microscopes are Gallium Nitride (GaN) devices, following state of the art for efficient micro and nanodevices with applications such as point light sources for optical communications, imaging or sensing [77, 78].

The progress of the LEDs in the Chipscope project is shown in figure 2.20. The initial LED arrays, not shown in the figure, consisted of large 75 μm structures, which were used to test and validate the initial assembly of the microscope, but the prototype used the array of 5 μm LEDs, distributed in an 8 × matrix. The smallest LEDs developed in this project were 200 nm in size, in a directly addressed array with a 32 × 2 form factor.

While LED nanopillars [79] and nanostructures [80] have been already demonstrated, those are proof of concept devices for the associated LED technology and laboratory use and not intended to be integrated into arrays as is needed for the microscopes developed in this thesis. Instead, to control the light emission with as much spatial precision as possible, several GaN microLED arrays were fabricated by the team of Prof. Dr A. Waag at the Technische Universität Braunschweig. Beyond NIM, LEDs are already used in macroscopic structured illumination applications such as optical communications, which might benefit from further miniaturisation [81].

The most critical step to create dense arrays is to trace the contacts to each individual LED of the array without short circuits, minimise crosstalk and manage the high defect densities present in GaN wafers. There are two design strategies to address this problem in the way the LEDs in the array are addressed: direct LED addressing and matrix addressing.

In direct LED addressing, each LED is individually contacted, with all of them sharing the cathode contact. This means an array of N LEDs will need N connec-

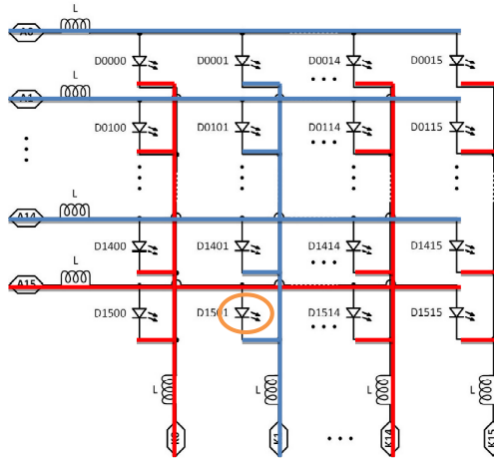


Figure 2.21: Matrix LED addressing connection scheme. Each row line connects the Anodes, while the columns connect with the cathodes. Setting an LED to emit requires a high voltage (shown in red) at the row of interest, combined with a low voltage level (shown in blue) at the desired column. In the image, this combines to allow emission from the highlighted LED.

tions and lines and a certain number of additional contacts for the shared cathode. The routing complexity grows with the number of LEDs in the array, and the physical space required for correct routing limits the size of the array to less than 100 LEDs with current technology. On the other hand, each LED is individually controlled, which allows for arbitrary illumination patterns and fast switching between them.

An alternative approach is matrix addressing, in which there is a chip contact for each row and column of the array. Addressing a specific LED requires setting the corresponding cathodes column at low voltage and the anodes row at a high, a process illustrated with an example in figure 2.21. In it, all the (anode) rows except the one of interest are kept at a low voltage level (shown in blue), while the (cathode) columns are kept at a high voltage level (shown in red), which polarises most LEDs in reverse and so not conducting, except for the circled LED, which will emit.

Matrix addressing greatly reduces the number of contacts necessary for the operation of the array. This is a vital step to reduce connection complexity and so to fabricate larger arrays, which will allow for NIM microscopes with a larger field of view. However, the fabrication process has only a single metal available for interconnections. This makes laying out the interconnections challenging since there will necessarily be overlapping lines. While this approach was investigated during the project, the only LED arrays fabricated with a matrix addressing strategy were of larger $10\ \mu\text{m}$ LEDs. The larger sizes and the fact that a matrix addressing approach does not allow arbitrary illumination patterns meant these have not been used in any of the microscopes, so these arrays are not discussed in this thesis.

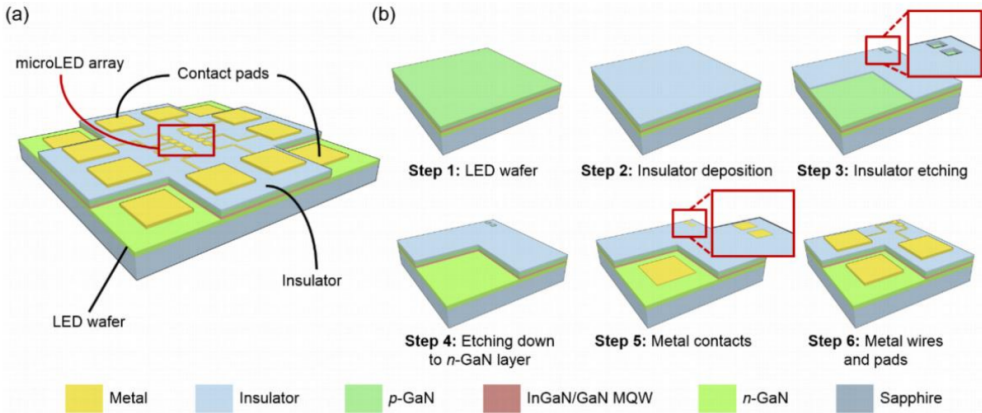


Figure 2.22: Structure of the LED array used for the first prototypes of the NIM microscope: a GaN nanoLED array chip with 64 (8×8) pixels sized $5 \mu\text{m}$. (a) 3D sketch of the chip and its layers. (b) fabrication flow.

For all the arrays developed, the spacing between LEDs equals the LED size. The first array, used for the first microscope prototype, is an 8×8 matrix of $5 \mu\text{m}$ LEDs, which implies a pitch of $10 \mu\text{m}$, based on InGaN/GaN quantum wells grown on sapphire wafer [82]. The technique used physically separates the LEDs by deep-etching and planarising the structures, a process difficult to control. This process deposited individual Cr/Au contacts to the p side of each LED and an n-type contact common to all pixels, with light being emitted through the $300 \mu\text{m}$ thick sapphire substrate. A schematic overview of the fabrication process can be seen in figure 2.22 a), illustrating the general structure of the array, while figure 2.22 b) shows the detailed picture of the LED array. Step 1 shows the LED wafer planarly grown, over which an insulating layer is deposited (Step 2). Step 3 shows the etching on the insulator to reach the p-GaN, followed by ICP-RIE for etching down to the n-GaN layer in step 4. After that, metal is deposited for n and p contacts as step 5, and finally, the metal interconnects and contact pads are created in step 6. The metallic lines needed to cross through the LED array on their way outwards towards the contact pads of the chip are densely distributed. This connection strategy is not scalable with a larger number of LEDs in the array, nor would it help with smaller LEDs. This can be better appreciated on figure 2.23 b), which shows the picture of the resulting first directly addressable, $5 \mu\text{m}$ LED array fabricated. Meanwhile, 2.23 a) shows a general view of the entire LED chip with its contact pads. These pads will be bonded to a PCB designed by us at UB for driving.

Keeping good interconnection to each LED was the main challenge in pushing their size down below the micron range. At the same time, and as it will be explained in the following chapters, emission through the sapphire was undesirable because it forced the sample away from the LED. To address this, a new method was devel-

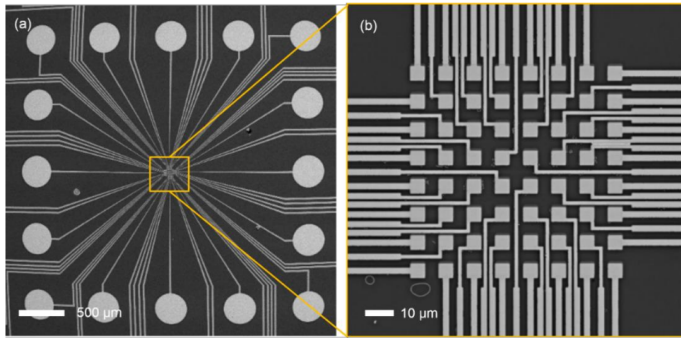


Figure 2.23: Picture of the realised 8×8 , $5 \mu\text{m}$ GaN LED chip with a direct addressing strategy. (a) Shows the large bonding pads surrounding the (b) microLED array for flip-chip integration.

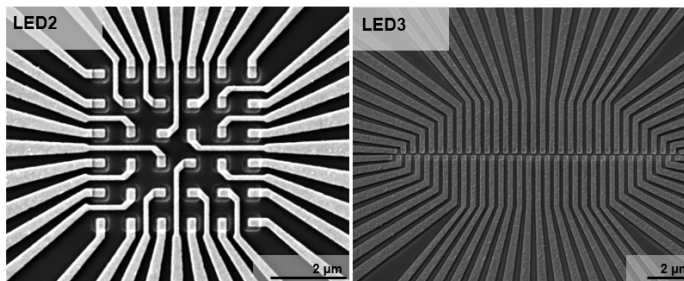


Figure 2.24: SEM images of the finalised array structures for the (a) 6×6 array of 400 nm LEDs and (b) the 2×32 array of 200 nm LEDs.

oped, consisting of a metal-oxide-GaN (MOGaN) process [78]. This process uses the low conductivity of the p-GaN layer to its advantage: since the current barely spreads from the metal contacts, the nanoLED is defined by the size of that contact without the need for etching structures to separate the individual LED. At the same time, the contacts were kept thin enough to ensure they were transparent, intending for the light emitted to go through them instead of flipping the chip and having to cross the sapphire. The resulting LED arrays can be seen in the SEM images of figure 2.24 for the 6×6 array of 400 nm LEDs and the 2×32 array of 200 nm LEDs.

The light emission on these arrays approximates a Lambertian profile as shown in figure 2.25, which shows a measurement of the angular radiant intensity distribution obtained experimentally by the Braunschweig team. This, together with the light being generated $300 \mu\text{m}$ below the surface of their chip for the first array and at least a few hundreds of nanometers for the MOGaN arrays, negatively affects the contrast attainable with the microscopes.

One of the main concerns to address with these small LEDs is the possibility to switch them fast. This would be vital for fluorescence measurements, and in any case, it is necessary to ensure it is not much of a limiting factor for the measurement

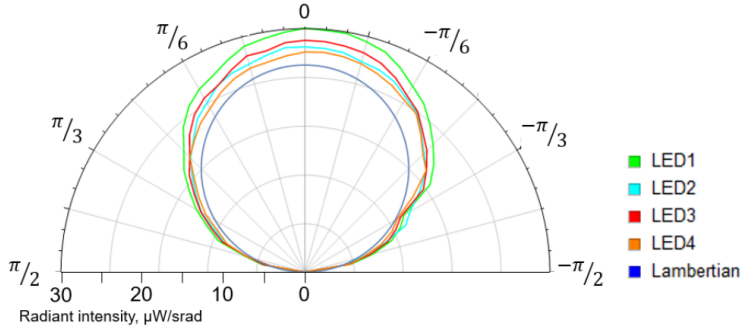


Figure 2.25: Angular radiant intensity distribution ($\mu\text{W}/\text{srad}$) of four micro-LEDs with an angular resolution of 1° .

rate. To test both the characteristics of the emission and the system, we did a series of tests by driving one of the $5\ \mu\text{m}$ LEDs from the array directly from the FPGA (and so with a fixed 3.3 V and 12 mA strength output). To study the optical response from the μLED , we used the SPAD camera previously presented, as well as the FPGA implemented TDC, which provides timing resolutions of 100 ps [37]. The optical pulses measured for different electrical pulses are shown in figure 2.26. The LEDs can accommodate a 13.33 ns pulse train, but the maximum intensity is reduced. To obtain the maximum number of counts (optical intensity), the pulse's minimal length is 24 ns.

2.6. Conclusions

In this chapter, we have detailed and offered an overview of the state of the art of the NIM microscope's main components, beginning with a SPAD array to be used to detect the emissions from the LED arrays. The use of a SPAD is justified by its flexibility, leaving open the possibility to use it for fluorescence measurements in the future, and also for its single-photon detection capabilities: they could be used even if the emissions of the smaller LEDs to be fabricated within the context of the project were low.

The SPADs have been designed in a High Voltage CMOS process in the 350 nm node and show a DCR around 200 Hz, with a PDE of around 30%, all in agreement with the bibliography on similar technological processes. These SPADs are used to build a 16×16 pixels camera with the intent set on offering more flexibility than a single SPAD sensor: it allows the use of the best SPAD in the array and offers some limited imaging capabilities while exploring a sample as a microscope.

Meanwhile, the other main component has also been presented: the LED arrays custom fabricated by TUBS. Three different versions have been developed, each building on the previous design experience. The first version was an 8×8 array of directly addressable LEDs with a size of $5\ \mu\text{m}$. This version allowed us to explore the

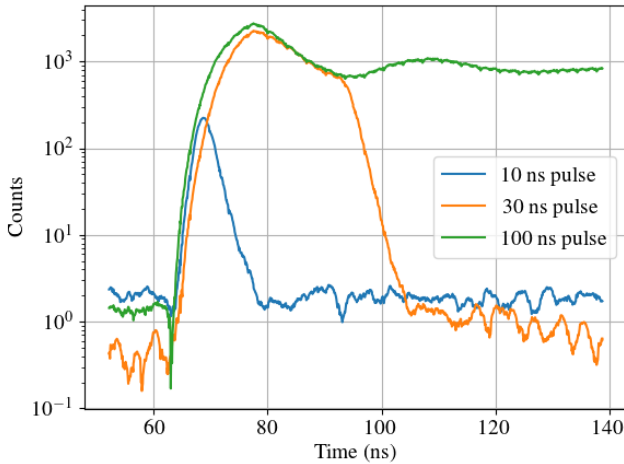


Figure 2.26: Optical response from the $5\ \mu\text{m}$ LEDs for pulses of 10, 30 and 100 ns measured with the SPAD camera. The 100 ns pulse offers the benchmark for ideal long commutation. The 30 ns pulse is in good agreement with it already.

NIM concept and raised some limitations: a direct addressing method to drive the LEDs would not be scalable to larger arrays since the space left for connections is further limited.

Different strategies were tested in the following arrays. The second version aimed to explore the limits of miniaturisation of the LED technology, but at the price of a worse form factor, of 2 rows and 32 columns of $200\ \text{nm}$ LEDs. This array clarified the difficulties that creating the contacts and the emitting structures for arrays at such a scale would have.

A final LED array was designed with a form factor of only 6×6 pixels and larger LEDs, but with the intent of validating the matrix driving strategy.

In conclusion, future works will require this final connection strategy: instead of direct LED addressing, a matrix-based selection scheme will allow the LED arrays to be scaled into devices with more pixels, an essential step for microscopes with more extensive fields of view and resolutions (with smaller LEDs).

In the next chapter, we use the initial 8×8 array of directly addressable LEDs with a size of $5\ \mu\text{m}$ to build the first NIM microscope from which we study the operation principle. Then, progressing further into the thesis, we use the smaller LEDs to try and push for the limits of the technology, as well as test the matrix addressing approach.

References

- [1] K. B. W. Harpsøe, M. I. Andersen, and P. Kjægaard. “Bayesian photon counting with electron-multiplying charge coupled devices (EMCCDs)”. In: *Astronomy & Astrophysics* 537 (Jan. 2012), A50. ISSN: 0004-6361. DOI: 10 . 1051 / 0004 - 6361 / 201117089. arXiv: 1111 . 2066.
- [2] Vaughn J. Koester and Robert M. Dowben. “Subnanosecond single photon counting fluorescence spectroscopy using synchronously pumped tunable dye laser excitation”. In: *Review of Scientific Instruments* 49.8 (Aug. 1978), p. 1186. ISSN: 0034-6748. DOI: 10 . 1063 / 1 . 1135545.
- [3] J. A. Tyson. “Progress in low-light-level charge-coupled device imaging in astronomy”. In: *Journal of the Optical Society of America A* 7.7 (July 1990), p. 1231. ISSN: 1084-7529. DOI: 10 . 1364 / JOSAA . 7 . 001231.
- [4] Paul Jerram et al. “The LLCCD: low-light imaging without the need for an intensifier”. In: *Sensors and Camera Systems for Scientific, Industrial, and Digital Photography Applications II*. Ed. by Morley M. Blouke, John Canosa, and Nitin Sampat. May 2001, p. 178. DOI: 10 . 1117 / 12 . 426953.
- [5] Eric Betzig et al. “Imaging Intracellular Fluorescent Proteins at Nanometer Resolution”. In: *Science* 313.5793 (Sept. 2006), pp. 1642–1645. ISSN: 0036-8075. DOI: 10 . 1126 / science . 1127344.
- [6] Samuel T. Hess, Thanu P.K. Girirajan, and Michael D. Mason. “Ultra-High Resolution Imaging by Fluorescence Photoactivation Localization Microscopy”. In: *Biophysical Journal* 91.11 (Dec. 2006), pp. 4258–4272. ISSN: 00063495. DOI: 10 . 1529 / biophysj . 106 . 091116.
- [7] Michael J Rust, Mark Bates, and Xiaowei Zhuang. “Sub-diffraction-limit imaging by stochastic optical reconstruction microscopy (STORM)”. In: *Nature Methods* 3.10 (Oct. 2006), pp. 793–796. ISSN: 1548-7091. DOI: 10 . 1038 / nmeth929.
- [8] Fang Huang et al. “Video-rate nanoscopy using sCMOS camera-specific single-molecule localization algorithms”. In: *Nature Methods* 10.7 (July 2013), pp. 653–658. ISSN: 1548-7091. DOI: 10 . 1038 / nmeth . 2488.
- [9] Boyd Fowler. “Single Photon CMOS Imaging Through Noise Minimization”. In: *Springer Series in Optical Sciences*. 2011, pp. 159–195. ISBN: 9783642184420. DOI: 10 . 1007 / 978 - 3 - 642 - 18443 - 7_8.
- [10] Chockalingam Veerappan et al. “A 160x128 single-photon image sensor with on-pixel 55ps 10b time-to-digital converter”. In: *2011 IEEE International Solid-State Circuits Conference*. IEEE, Feb. 2011, pp. 312–314. ISBN: 978-1-61284-303-2. DOI: 10 . 1109 / ISSCC . 2011 . 5746333.

- [11] Yujie Wang et al. “Understanding and assessing low-light cameras for super-resolution localization microscopy”. In: *2nd IET International Conference on Biomedical Image and Signal Processing (ICBISP 2017)*. Institution of Engineering and Technology, 2017, 2 (6 .)-2 (6 .) ISBN: 978-1-78561-318-0. DOI: 10.1049/cp.2017.0078.
- [12] Venkataraman Krishnaswami et al. “Towards digital photon counting cameras for single-molecule optical nanoscopy”. In: *Optical Nanoscopy 3.1* (2014), p. 1. ISSN: 2192-2853. DOI: 10.1186/2192-2853-3-1.
- [13] Neale A. W. Dutton et al. “A SPAD-Based QVGA Image Sensor for Single-Photon Counting and Quanta Imaging”. In: *IEEE Transactions on Electron Devices* 63.1 (Jan. 2016), pp. 189–196. DOI: 10.1109/TED.2015.2464682.
- [14] Istvan Gyongy et al. “Smart-aggregation imaging for single molecule localisation with SPAD cameras”. In: *Scientific Reports* 6.1 (Dec. 2016), p. 37349. ISSN: 2045-2322. DOI: 10.1038/srep37349. arXiv: 1602.04191.
- [15] A. Rochas et al. “Single photon detector fabricated in a complementary metal oxide semiconductor high-voltage technology”. In: *Review of Scientific Instruments* 74.7 (July 2003), pp. 3263–3270. ISSN: 0034-6748. DOI: 10.1063/1.1584083.
- [16] Joan Canals et al. “A Point-of-Care Device for Molecular Diagnosis Based on CMOS SPAD Detectors with Integrated Microfluidics”. In: *Sensors (Basel, Switzerland)* 19.3 (Jan. 2019), p. 445. ISSN: 1424-8220. DOI: 10.3390/s19030445.
- [17] R. J. McIntyre. “Theory of Microplasma Instability in Silicon”. In: *Journal of Applied Physics* 32.6 (June 1961), pp. 983–995. ISSN: 0021-8979. DOI: 10.1063/1.1736199.
- [18] Roland H. Haitz. “Model for the Electrical Behavior of a Microplasma”. In: *Journal of Applied Physics* 35.5 (May 1964), pp. 1370–1376. ISSN: 0021-8979. DOI: 10.1063/1.1713636.
- [19] Cristiano Niclass et al. “Toward a 3-D Camera Based on Single Photon Avalanche Diodes”. In: *IEEE Journal of Selected Topics in Quantum Electronics* 10.4 (July 2004), pp. 796–802. ISSN: 1077-260X. DOI: 10.1109/JSTQE.2004.833886.
- [20] S. Cova et al. “Avalanche photodiodes and quenching circuits for single-photon detection”. In: *Applied Optics* 35.12 (Apr. 1996), p. 1956. ISSN: 0003-6935. DOI: 10.1364/AO.35.001956.
- [21] S. Tisa et al. “Electronics for single photon avalanche diode arrays”. In: *Sensors and Actuators A: Physical* 140.1 (Oct. 2007), pp. 113–122. ISSN: 09244247. DOI: 10.1016/j.sna.2007.06.022.
- [22] Franco Zappa et al. “An integrated active-quenching circuit for single-photon avalanche diodes”. In: *IEEE Transactions on Instrumentation and Measurement* 49.6 (2000), pp. 1167–1175. ISSN: 00189456. DOI: 10.1109/19.893251.

- [23] Andreas Eisele and Robert Henderson. “185 MHz Count Rate, 139 dB Dynamic Range Single-Photon Avalanche Diode with Active Quenching Circuit in 130nm CMOS Technology”. In: *2011 International ...* (2011).
- [24] Nikola Krstajić et al. “256 × 2 SPAD line sensor for time resolved fluorescence spectroscopy”. In: *Optics Express* 23.5 (Mar. 2015), p. 5653. ISSN: 1094-4087. DOI: 10.1364/OE.23.005653.
- [25] H. A. R. Homulle et al. “Compact solid-state CMOS single-photon detector array for in vivo NIR fluorescence lifetime oncology measurements”. In: *Biomedical Optics Express* 7.5 (May 2016), p. 1797. ISSN: 2156-7085. DOI: 10.1364/BOE.7.001797.
- [26] Claudio Bruschini et al. “Single-photon avalanche diode imagers in biophotonics: review and outlook”. In: *Light: Science & Applications* 8.1 (Dec. 2019), p. 87. ISSN: 2047-7538. DOI: 10.1038/s41377-019-0191-5.
- [27] Mario Stipčević, Daqing Wang, and Rupert Ursin. “Characterization of a commercially available large area, high detection efficiency single-photon avalanche diode”. In: *Journal of Lightwave Technology* 31.23 (2013). ISSN: 07338724. DOI: 10.1109/JLT.2013.2286422.
- [28] Michael Hofbauer, Bernhard Steindl, and Horst Zimmermann. “Temperature Dependence of Dark Count Rate and after Pulsing of a Single-Photon Avalanche Diode with an Integrated Active Quenching Circuit in 0.35 μ m CMOS”. In: *Journal of Sensors* 2018 (2018). ISSN: 16877268. DOI: 10.1155/2018/9585931.
- [29] Marek Gersbach et al. “A low-noise single-photon detector implemented in a 130 nm CMOS imaging process”. In: *Solid-State Electronics* 53.7 (2009). ISSN: 00381101. DOI: 10.1016/j.sse.2009.02.014.
- [30] Robert K. Henderson, Lindsay A. Grant, and Justin A. Richardson. “Reduction of Band-to-band Tunneling in Deep-submicron CMOS Single Photon Avalanche Photodiodes”. In: *International Image Sensor Workshop* (2009).
- [31] Justin A. Richardson, Lindsay A. Grant, and Robert K. Henderson. “Low dark count single-photon avalanche diode structure compatible with standard nanometer scale CMOS technology”. In: *IEEE Photonics Technology Letters* 21.14 (2009). ISSN: 10411135. DOI: 10.1109/LPT.2009.2022059.
- [32] Matthew William Fishburn. “Fundamentals of CMOS single-photon avalanche diodes”. PhD thesis. Delft University of Technology, 2012. ISBN: 9491030299. DOI: 10.4233/uuid:7ed6e57d-404e-4372-8053-6b0b5c7fa0fe.
- [33] Ivan Michel Antolovic et al. “Nonuniformity Analysis of a 65-kpixel CMOS SPAD Imager”. In: *IEEE Transactions on Electron Devices* 63.1 (Jan. 2016), pp. 57–64. DOI: 10.1109/TED.2015.2458295.

- [34] Fabio Acerbi et al. “Fast active quenching circuit for reducing avalanche charge and afterpulsing in InGaAs/InP single-photon avalanche diode”. In: *IEEE Journal of Quantum Electronics* 49.7 (2013). ISSN: 00189197. DOI: 10.1109/JQE.2013.2260726.
- [35] Benoit Louis Berube et al. “Implementation Study of Single Photon Avalanche Diodes (SPAD) in 0.8 μ m HV CMOS Technology”. In: *IEEE Transactions on Nuclear Science* 62.3 (2015). ISSN: 00189499. DOI: 10.1109/TNS.2015.2424852.
- [36] E. Sciacca et al. “Arrays of geiger mode avalanche photodiodes”. In: *IEEE Photonics Technology Letters* 18.15 (2006). ISSN: 10411135. DOI: 10.1109/LPT.2006.879576.
- [37] N. Franch et al. “A low cost fluorescence lifetime measurement system based on SPAD detectors and FPGA processing”. In: *Journal of Instrumentation* 12.02 (Feb. 2017), pp. C02070–C02070. DOI: 10.1088/1748-0221/12/02/C02070.
- [38] Danilo Bronzi et al. “Low-noise and large-area CMOS SPADs with timing response free from slow tails”. In: *2012 Proceedings of the European Solid-State Device Research Conference (ESSDERC)*. IEEE, Sept. 2012, pp. 230–233. ISBN: 978-1-4673-1707-8. DOI: 10.1109/ESSDERC.2012.6343375.
- [39] E. Vilella and A. Diéguez. “A gated single-photon avalanche diode array fabricated in a conventional CMOS process for triggered systems”. In: *Sensors and Actuators, A: Physical*. Vol. 186. Oct. 2012, pp. 163–168. DOI: 10.1016/j.sna.2012.01.019.
- [40] Nicola D’Ascenzo, Xi Zhang, and Qingguo Xie. “Application of CMOS Technology to Silicon Photomultiplier Sensors”. In: *Sensors* 17.10 (Sept. 2017), p. 2204. ISSN: 1424-8220. DOI: 10.3390/s17102204.
- [41] R. Blanco, C. Kraemer, and I. Perić. “Silicon photomultiplier detector with multipurpose in-pixel electronics in standard CMOS technology”. In: *Nuclear Instruments and Methods in Physics Research Section A: Accelerators, Spectrometers, Detectors and Associated Equipment* 936 (Aug. 2019), pp. 699–700. ISSN: 01689002. DOI: 10.1016/j.nima.2018.09.107.
- [42] Neale A.W. Dutton et al. “High dynamic range imaging at the quantum limit with single photon avalanche diode-based image sensors”. In: *Sensors (Switzerland)* 18.4 (2018). ISSN: 14248220. DOI: 10.3390/s18041166.
- [43] O. Alonso et al. “An internet of things-based intensity and time-resolved fluorescence reader for point-of-care testing”. In: *Biosensors and Bioelectronics* 154 (2020). ISSN: 18734235. DOI: 10.1016/j.bios.2020.112074.
- [44] E. Vilella et al. “A low-noise time-gated single-photon detector in a HV-CMOS technology for triggered imaging”. In: *Sensors and Actuators, A: Physical* 201 (2013). ISSN: 09244247. DOI: 10.1016/j.sna.2013.08.006.

- [45] Justin A. Richardson et al. "Scaleable Single-Photon Avalanche Diode Structures in Nanometer CMOS Technology". In: *IEEE Transactions on Electron Devices* 58.7 (July 2011), pp. 2028–2035. DOI: 10.1109/TED.2011.2141138.
- [46] Danilo Bronzi et al. "SPAD Figures of Merit for Photon-Counting, Photon-Timing, and Imaging Applications: A Review". In: *IEEE Sensors Journal* 16.1 (Jan. 2016), pp. 3–12. ISSN: 1530-437X. DOI: 10.1109/JSEN.2015.2483565.
- [47] Vitali Savuskan et al. "An Estimation of Single Photon Avalanche Diode (SPAD) Photon Detection Efficiency (PDE) Nonuniformity". In: *IEEE Sensors Journal* 13.5 (May 2013), pp. 1637–1640. ISSN: 1530-437X. DOI: 10.1109/JSEN.2013.2240154.
- [48] Eva Vilella. "Feasibility of Geiger-mode avalanche photodiodes in CMOS standard technologies for tracker detectors". Universitat de Barcelona, 2013.
- [49] Andrew J. Clark et al. "Ocular Tolerance of Contemporary Electronic Display Devices". In: *Ophthalmic Surgery, Lasers and Imaging Retina* 49.5 (May 2018), pp. 346–354. ISSN: 2325-8160. DOI: 10.3928/23258160-20180501-08.
- [50] Hui Zhang. "Head-mounted display-based intuitive virtual reality training system for the mining industry". In: *International Journal of Mining Science and Technology* 27.4 (July 2017), pp. 717–722. ISSN: 20952686. DOI: 10.1016/j.ijmst.2017.05.005.
- [51] Seonil Kwon et al. "Recent Progress of Fiber Shaped Lighting Devices for Smart Display Applications—A Fibertronic Perspective". In: *Advanced Materials* 32.5 (Feb. 2020), p. 1903488. ISSN: 0935-9648. DOI: 10.1002/adma.201903488.
- [52] Donald L. White and Gary N. Taylor. "New absorptive mode reflective liquid-crystal display device". In: *Journal of Applied Physics* 45.11 (Nov. 1974), pp. 4718–4723. ISSN: 0021-8979. DOI: 10.1063/1.1663124.
- [53] Gerard Harbers, Wim Timmers, and Willem Sillevius-Smitt. "LED backlighting for LCD HDTV". In: *Journal of the Society for Information Display* 10.4 (2002), p. 347. ISSN: 10710922. DOI: 10.1889/1.1827889.
- [54] Peng Wang. "An LCD monitor with sufficiently precise timing for research in vision". In: *Frontiers in Human Neuroscience* 5.AUGUST (2011). ISSN: 16625161. DOI: 10.3389/fnhum.2011.00085.
- [55] Hiroyuki Ohshima and Dai-Liang Ting. "Turning Points in Mobile Display Development". In: *SID Symposium Digest of Technical Papers* 42.1 (June 2011), pp. 97–100. ISSN: 0097966X. DOI: 10.1889/1.3621507.

- [56] Eduardo Cuervo, Krishna Chintalapudi, and Manikanta Kotaru. "Creating the perfect illusion : what will it take to create life-like virtual reality headsets?" In: *HotMobile 2018 - Proceedings of the 19th International Workshop on Mobile Computing Systems and Applications*. Vol. 2018-Febru. New York, NY, USA: ACM, Feb. 2018, pp. 7–12. ISBN: 9781450356305. DOI: 10 . 1145 / 3177102 . 3177115.
- [57] Susumu Kawashima et al. "A 1058-ppi 4K ultrahigh-resolution and high aperture LCD with transparent pixels using OS/OC technology". In: vol. 48. 2017. DOI: 10 . 1002 / s d t p . 11679.
- [58] Taeil Jung et al. "Review of micro-light-emitting-diode technology for micro-display applications". In: *Digest of Technical Papers - SID International Symposium*. Vol. 50. Book 1. 2019. DOI: 10 . 1002 / s d t p . 12951.
- [59] Fumio Kataoka et al. "Evaluation of Clinical Usefulness of a Medical Monitor Equipped With an Organic Electroluminescence Panel in Comparison With Liquid Crystal Display Monitors". In: *Journal of Minimally Invasive Gynecology* 20.4 (July 2013), pp. 522–528. ISSN: 15534650. DOI: 10 . 1016 / j . j m i g . 2013 . 02 . 008.
- [60] Bernard Geffroy, Philippe le Roy, and Christophe Prat. "Organic light-emitting diode (OLED) technology: materials, devices and display technologies". In: *Polymer International* 55.6 (June 2006), pp. 572–582. ISSN: 0959-8103. DOI: 10 . 1002 / p i . 1974.
- [61] J.N. Bardsley. "International OLED Technology Roadmap". In: *IEEE Journal of Selected Topics in Quantum Electronics* 10.1 (Jan. 2004), pp. 3–9. ISSN: 1077-260X. DOI: 10 . 1109 / J S T Q E . 2004 . 824077.
- [62] Hiroshi Kanno, Yuji Hamada, and Hisakazu Takahashi. "Development of OLED With High Stability and Luminance Efficiency by Co-Doping Methods for Full Color Displays". In: *IEEE Journal of Selected Topics in Quantum Electronics* 10.1 (Jan. 2004), pp. 30–36. ISSN: 1077-260X. DOI: 10 . 1109 / J S T Q E . 2004 . 824076.
- [63] Bhrijesh N Patel and Mrugesh M Prajapati. "OLED: A Modern Display Technology". In: *International Journal of Scientific and Research Publications* 4.1 (2014), pp. 2250–3153.
- [64] Takatoshi Tsujimura. *OLED Display Fundamentals and Applications*. 2017. DOI: 10 . 1002 / 9781119187493.
- [65] Pengcheng Lu et al. "Highest PPI micro-OLED display sustain for near-eye application". In: vol. 50. 2019. DOI: 10 . 1002 / s d t p . 13022.

- [66] Shuichi Katsui et al. "A 5291 ppi organic light-emitting diode display using field-effect transistors including a c-axis aligned crystalline oxide semiconductor". In: *Journal of the Society for Information Display* 27.8 (Aug. 2019), pp. 497–506. ISSN: 1071-0922. DOI: 10.1002/jsid.822.
- [67] François Templier. "GaN-based emissive microdisplays: A very promising technology for compact, ultra-high brightness display systems". In: *Journal of the Society for Information Display* 24.11 (Nov. 2016), pp. 669–675. ISSN: 19383657. DOI: 10.1002/jsid.516.
- [68] Zhou Wang et al. "Characteristics and techniques of GaN-based micro-LEDs for application in next-generation display". In: *Journal of Semiconductors* 41.4 (Apr. 2020), p. 041606. ISSN: 1674-4926. DOI: 10.1088/1674-4926/41/4/041606.
- [69] Warren C. Johnson, J. B. Parson, and M. C. Crew. "Nitrogen Compounds of Gallium. III". In: *The Journal of Physical Chemistry* 36.10 (Oct. 1932), pp. 2651–2654. ISSN: 0092-7325. DOI: 10.1021/j150340a015.
- [70] H. P. Maruska and J. J. Tietjen. "The preparation and properties of vapor-deposited single-crystal-line GaN". In: *Applied Physics Letters* 15.10 (1969). ISSN: 00036951. DOI: 10.1063/1.1652845.
- [71] J. I. Pankove et al. *Electroluminescence in GaN*. 1971. DOI: 10.1016/0022-2313(71)90009-3.
- [72] Akira Shintani and Shigekazu Minagawa. "Electric properties of GaN light-emitting diodes". In: *Journal of Applied Physics* 48.4 (1977). ISSN: 00218979. DOI: 10.1063/1.323872.
- [73] Zhe Chuan Feng. *Handbook of solid-state lighting and LEDs*. 2017. DOI: 10.1201/9781315151595.
- [74] H. Amano et al. "Metalorganic vapor phase epitaxial growth of a high quality GaN film using an AlN buffer layer". In: *Applied Physics Letters* 48.5 (1986). ISSN: 00036951. DOI: 10.1063/1.96549.
- [75] Shuji Nakamura et al. "Thermal annealing effects on P-type Mg-doped GaN films". In: *Japanese Journal of Applied Physics* 31.2 (1992). ISSN: 13474065. DOI: 10.1143/JJAP.31.L139.
- [76] Shuji Nakamura et al. "InGaN multi-quantum-well-structure laser diodes with cleaved mirror cavity facets". In: *Japanese Journal of Applied Physics, Part 2: Letters* 35.2 B (1996). ISSN: 00214922. DOI: 10.1143/JJAP.35.L217.
- [77] Hutomo Suryo Wasisto et al. *Beyond solid-state lighting: Miniaturization, hybrid integration, and applications of GaN nano-and micro-LEDs*. Dec. 2019. DOI: 10.1063/1.5096322.

-
- [78] Daria D. Bezshlyakh et al. "Directly addressable GaN-based nano-LED arrays: fabrication and electro-optical characterization". In: *Microsystems and Nano-engineering* 6.1 (2020). ISSN: 20557434. DOI: 10.1038/s41378-020-00198-y.
- [79] M. Mikulics and H. Hardtdegen. "Nano-LED array fabrication suitable for future single photon lithography". In: *Nanotechnology* 26.18 (2015). ISSN: 13616528. DOI: 10.1088/0957-4484/26/18/185302.
- [80] Johannes Herrnsdorf et al. "Active-matrix GaN micro light-emitting diode display with unprecedented brightness". In: *IEEE Transactions on Electron Devices* 62.6 (2015). ISSN: 00189383. DOI: 10.1109/TED.2015.2416915.
- [81] Neil T. Clancy et al. "Spectrally encoded fiber-based structured lighting probe for intraoperative 3D imaging". In: *Biomedical Optics Express* 2.11 (2011). ISSN: 2156-7085. DOI: 10.1364/boe.2.003119.
- [82] Jan Gülink et al. "InGaN/GaN nanoLED Arrays as a Novel Illumination Source for Biomedical Imaging and Sensing Applications". In: *Proceedings* 2.13 (Dec. 2018), p. 892. DOI: 10.3390/proceedings2130892.

3

Nano Illumination Microscopy

Chapter based on the article by N. Franch et al., “Nano illumination microscopy: a technique based on scanning with an array of individually addressable nanoLEDs”, In *Optics Express* 28.5 (June 2020)

3.1. Introduction

As we have shown before, the principles of NIM are based on those of a lensless setup. The fundamental difference is that the sample is placed immediately on top of the light sources, and its shadow is then detected by the sensor further on top. At first, we discuss a general overview of the NIM operating principle. This basic structure will remain the same for the different microscopes implemented during the thesis and in further chapters. After the overview, we show the first NIM prototype in detail, with both the hardware and the software discussed and the general assembly.

The chapter ends by showing the results of the observations with the prototype of NIM microscope, which agree with the predictions from theory and the simulations.

3.2. NIM Operation principle

NIM is an optical scanning microscopy technique with an approach geared towards providing low-cost and compact devices. The sampling is discrete and done by

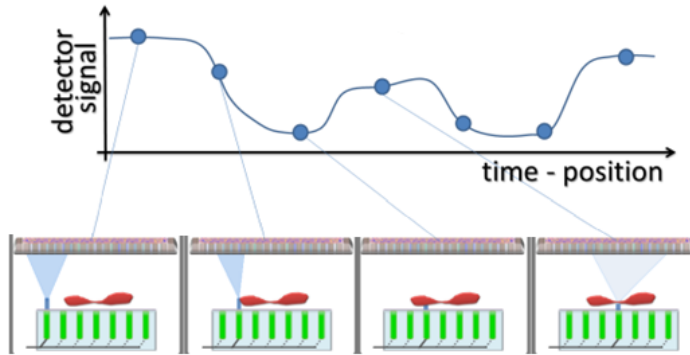


Figure 3.1: Operation principle of the NIM microscope: the sample is scanned by illuminating alternatively with different LEDs, and the sensor on top records the intensity of light reaching it.

switching on and off alternatively the LEDs in an array positioned as close as possible to the sample. Figure 3.1 shows a schema of the image acquisition process for a single line of the LED array: the sensor, opposite to the LEDs, measures the light reaching it from the LEDs through the sample. When the same process is repeated for every row of the array, the result is a direct map of the sample according to the light it blocks from each LED. This means that for this method, the microscope sensor only needs to capture the light/shadow cone from every LED in the array to operate correctly, hugely relaxing the impact of its fill factor or pixel size.

3.2.1. Operation of the microscope

In a usual lensless setup, the sample is positioned close to the sensors. This means that its field of view of these microscopes is approximately the area of the sensor device, usually an entire CMOS camera [1]. The field of view (FOV) is mainly given by the area scanned by the LEDs for a NIM microscope. The relationship between sensor and FOV is relaxed. In the ideal configuration in which the sample is in immediate contact with the light sources, the FOV has the same size as the LED array. This can be better appreciated in figure 3.2 c). Figure 3.2 shows the distribution and results of ray-tracing simulations comparing three fundamental operating conditions of a NIM setup using a single LED row since the process will be the same for each one. In this case, the sensor is $10\ \mu\text{m}$ in diameter, and the samples are four completely opaque, $12\ \mu\text{m}$ wide objects at different distances from the LEDs and the sensor.

In figure 3.2 a) the setup is that of a conventional lensless microscope. Samples are placed far from the light sources, and so the light reaches them as if it had been emitted from basically the same position since each LED propagates the same shadows from the sample to the sensor plane. This is due to the small pitch of the LEDs in comparison to the distance to the sample (note the difference in scale between the x and y axis). In shadow imaging, it is important to keep the sample as close to

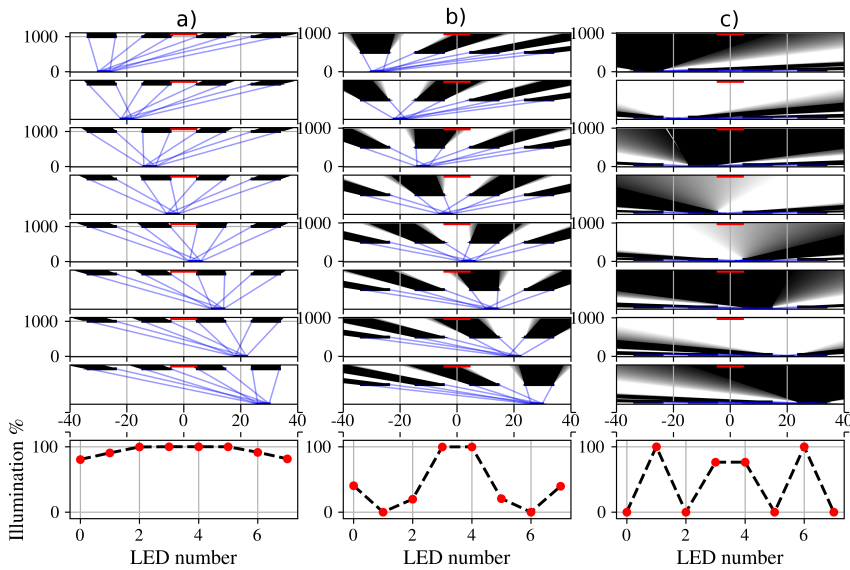


Figure 3.2: Detail and results for the ray-tracing simulation of the microscope operation for a single LED row. The red surfaces on the top part of each figure are the $10\ \mu\text{m}$ sensor, while the test samples are in black and are $12\ \mu\text{m}$ wide patterns. The LEDs (in blue at the lower part of each figure) switch on and off sequentially, creating shadow patterns on the sensor. The figure at the bottom shows the relative illumination received on the sensor with each LED. (a) Shadow imaging: the samples are close to the sensor, far from the LED. (b) Intermediate case: the increased distance makes proper sampling more difficult (c) Ideal NIM scan mode: the samples are very close to the LEDs, creating large shadow patterns.

the sensor as possible in order to have both maximum resolving power and field of view [2] so that the resolution is limited by the sensor pixel pitch and its fill factor. For NIM setups, it is the contrary, since the distance that needs to be minimized is the one between sample and light sources.

The reason for that can be appreciated in figures 3.2 b) and c), which show image formation for a single row of a micro-LED array. Image formation consists only of switching a single LED of the array to illuminate a small piece of the sample. The intensity of light reaching the sensor gives information about the object's geometry and transmissivity. This is repeated for all LEDs in the array to create the sample map.

Figure 3.2 c) simulates the ideal construction and distribution for a NIM setup, with the object very near to the LED array (ideally, in direct contact to it). As it can be seen, this creates large shadows projected from the object, which the sensor can easily detect, and also shows how the field of view of the microscope is the size of the LED array itself.

3.2.1.1. Resolving power and object detection

Thanks to the reciprocity principle, we see that the resolving power depends on similar and complementary parameters to those of conventional lensless setups. Where a lensless microscope relies on the pitch and fill-factor of the sensing camera pixels, here dependence is with the LED pitch. Other factors that cannot be ignored once the LED size approaches the micron size are the coherence of the light source and the diffraction through the medium between light source and sample.

Objects smaller than an individual LED can be detected, but it will be impossible to resolve two in close proximity, and even for a single object, the contrast will degrade. This is illustrated in figure 3.3, which shows a diagram of the shadows projected by an object smaller than the LEDs used for sampling. The illustration shows the detector pixel in red at the top, the LEDs in blue at the bottom and the sample at the middle. The sample is placed at a height d from the LEDs. The dark grey region corresponds to the umbra cone, where light from the LED is completely blocked by the sample, which is the optimal case regarding contrast. The region in clearer grey is the penumbra cone, or the region in which the sample only partially blocks the light from the LED. A detector with enough dynamics will detect that the object is blocking some light. However, no information about the object or its shape will be obtained.

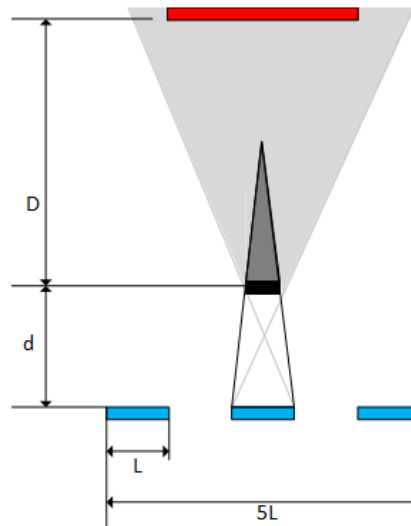


Figure 3.3: Schematic of the shadow cone projected by an object smaller than the LEDs. The red piece at the top of the illustration represents the detector pixel. At the bottom of the figure, the clear blue rectangles represent $3 \mu\text{LEDs}$ from the array. Between the two sets, in black, the sample might be found.

We can directly apply sampling theory to an idealized NIM microscope, with the LED matrix providing spatial sampling and the pitch in the array being the equiva-

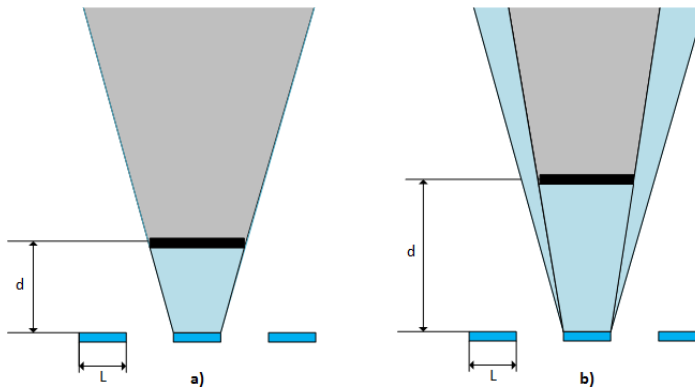


Figure 3.4: The schematic shows the reason for the contrast degradation with the distance between LEDs and the sample. The LED at the bottom emits light with the Lambertian profile previously shown, but for the image here, only the rays tracing the umbra of the sample are considered in a). In b), the object is further away from the LEDs.

lent of the sampling rate. With that said, to correctly resolve two objects (or details within a sample), their pitch has to be larger than twice the LEDs pitch to avoid aliasing and thus losing information [3, 4]. It must be noted that as the definition for the sampling theorem indicates, samples or details with the same periodicity as the LEDs will not be sampled appropriately, since even considering an ideal case for the other parameters, the sensor would detect the exact same signal from each LED, and so not offering useful information.

An example of incorrect sampling is shown in figure 3.2 b), in which the opaque squares used as samples have a pitch of $12.8 \mu\text{m}$ and a length of $6.4 \mu\text{m}$, and so are not sampled adequately by the array of LEDs with $20 \mu\text{m}$ pitch: at the central area of this image, due to aliasing, the objects are sampled as being joined together. This figure simulates the distances involved in a sample observed with the first prototype microscope built, shown later in this chapter.

3.2.1.2. Contrast

The closer the object to the light source, the better to produce sharper contrasted images: as the object moves away from the sampling LED and the light spot becomes more extensive, so does the illuminated area. With a larger illuminated area, information from a larger part of the sample will propagate towards the sensor, as can be seen in figure 3.4, which compares two cases. With the sample at the default position in a), a certain umbra propagates from the sample. In 3.4 b) the sample has been moved upwards, which makes the umbra smaller and, in this case, allows the light from the μLED to propagate. The clear blue area highlights the difference. This process can be thought of as taking multiple samples at the same coordinate, which are then integrated together and thus lower contrast.

Figure 3.5 shows the evolution of contrast as the system moves from bad oper-

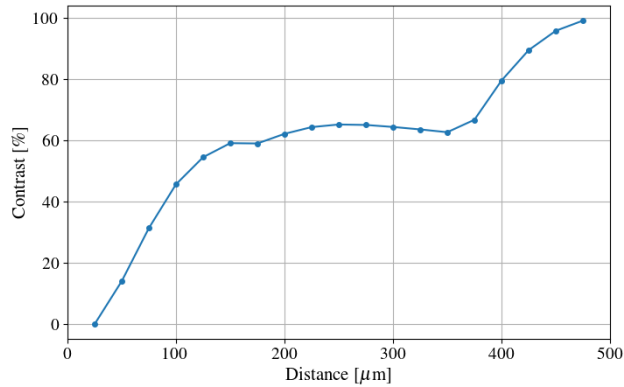


Figure 3.5: Contrast detected from scanning with a single row of the LED array as a function of the distance D between sample and sensor. These results were obtained from ray-tracing simulation, with the rest of the parameters fixed and chosen to reproduce the experimental setup found in the first prototype.

ating distances (sample much closer to the sensor than to the LED array) to NIM conditions. It has been obtained from ray-tracing simulations, with the intensities measured on a $10\ \mu\text{m}$ sensor while scanning with a single row of $5\ \mu\text{m}$ LEDs, varying the D distance between sample and sensor. The distance between LEDs and sample is kept constant as $d = 300\ \mu\text{m}$, simulating the conditions that will be found on the first microscope prototype fabricated later. For completion, the samples used are $11\ \mu\text{m}$ squares. The contrast improves as the system moves into NIM conditions. For distances D close to 0, the system is operating in what could be thought as classic lensless mode, conditions shown in figure 3.2 a). Contrast is improved as the relative distance between sample and sensor increases in relation to the distance between sample and LEDs.

3.3. NIM design guidelines

Discussion about the requirements on the design of a NIM microscope is illustrated with the help of figure 3.6, where d is the distance between LEDs and sample, and D is the distance between sample and sensing area. Figure 3.6 a) shows the FOV of a NIM setup and how it depends on the LED – sensing area distance, as well as the width of the sensing area itself and the width of the nanoLED array. When the distance D is much larger than the distance d , that is, the microscope operates in ideal NIM conditions, the field of view is the width of the LED array, as long as the effect of the angle of incidence for the light can be compensated (for example, by adjusting the current through the LEDs). A way to remove any dependence on the angle from the FOV could be to make the optical detector as wide as the LED array, but this would result in a reduced contrast for the microscope as illustrated

in figures 3.6 b) and 3.6 c). In figure 3.6 b) it is shown the worst case in which the shadows from different LEDs overlap. This would happen if the sensor at a distance D from the sample crossed the dashed red lines. To avoid this, we have to set a maximum width for the detector, x_{det} .

Figure 3.7 shows the same distribution as figure 3.6 b), but with the relevant triangles used for obtaining a boundary condition for the width of the detection highlighted in red. In the figure, L is the size of the LED (which is half the pitch). The sample has been taken as having a total length of $2L$, or the theoretical minimum sized object that the microscope will be capable of adequately sampling. The distances H and h are used as support values for the algebra.

In these conditions, the highlighted red triangles are similar, and we can write the relationship in 3.1 between both of them. We also can substitute H for its dependence as $H = D - h$. For the operation, we use half the value for the length of the detector, referred to as x_{hdet} below.

$$\frac{x_{\text{hdet}}}{\frac{5L}{2}} = \frac{H}{h+d} \Rightarrow x_{\text{hdet}} = \frac{\frac{5L}{2}H}{h+d} \Rightarrow x_{\text{hdet}} = \frac{D-h}{d+h} \frac{5L}{2} \quad (3.1)$$

To determine the value for h , we use the relationship between the lower triangle and the smaller formed at the top of the sample until the ray crossing point, shown in 3.2.

$$\frac{L}{\frac{5L}{2}} = \frac{h}{h+d} \Rightarrow h = \frac{Ld}{\frac{5L}{2} - L} \quad (3.2)$$

The previous equations can be combined to obtain the relationship for the maximum width of the detector in as equation 3.3, where the factor 2 is left explicit to show we made the substitution $x_{\text{det}} = 2x_{\text{hdet}}$.

$$x_{\text{det}} < 2 \frac{3D-2d}{2d} L \quad (3.3)$$

This relationship confirms that there is a minimal distance between the sample and the detector. Moreover, to relax the requirements on the sensor, the distance D should be kept larger than d as necessary.

Figure 3.6 c) illustrates another situation to be considered. The sensor pictured integrates the shadows projected by different sample regions illuminated by the same LED. Since samples should be spaced twice the LED pitch, the condition follows equation 3.4. This relationship, obtained using similar triangles and very similar algebra than the previous demonstration, is less restrictive than the condition set in 3.3, and so this condition can be ignored.

$$x_{\text{det}} < 2 \frac{3D+2d}{2d} L \quad (3.4)$$

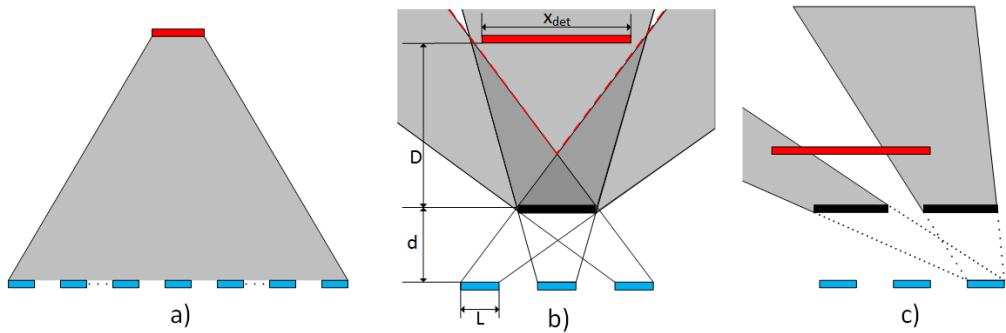


Figure 3.6: General schematics of the NIM microscope. In blue, LEDs from the array. In red, sensing area or sensor. a) shows the field of view for an arbitrary large LED array and sensor (grey shaded region). b) shows the shadow cones projected by a single sample (in black) from different LEDs and how they may overlap, which would mean the same area of the sample would be sampled by different LEDs, reducing the contrast of the microscope. The dashed red lines show the limits of that overlap zone c) shows the shadow cones projected by different samples while illuminated by the same LED and how they may be integrated together by a sensor too large.

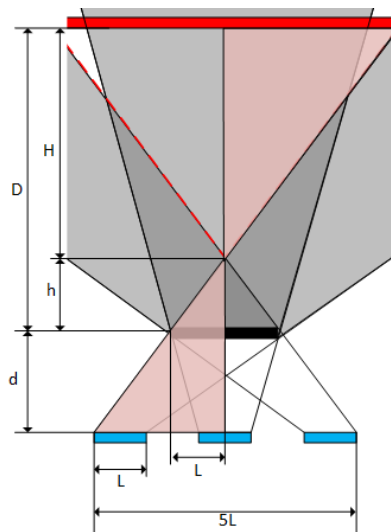


Figure 3.7: Schematic drawing highlighting the triangles used for obtaining the maximum size of the detector. L is the size of the LEDs. d is the distance between the LED array and sample. D is the distance between the sample and the detector. H and h are distances used in algebra.

3.4. Setup overview

All the NIM microscopes are built with the general structure shown in figure 3.8: the sample is held between the LED and the sensors. Since the sample has to be kept as close as possible to the light sources, we propose a setup with the LED array at the bottom and the sensor at the top. This proposal means that the sample can rest directly on the LED chip without the added complexity necessary for the opposite setup: keeping the LED array at the top would require a positioning stage raising the sample towards it and a way of making sure the distance is kept minimal without breaking the sample holder. In any case, all the different microscopes developed include positioning stages to move the sample into the microscope's field of view and to be able to explore different regions of interest. As it can be seen in figure 3.8, the light from the LEDs is transmitted through the sample, generating a pattern of shadows that the sensor will detect at the other end.

We built all the setups, keeping the maximum flexibility in mind to easily replace and change each component. This has been useful for developing the different prototypes, substituting the different components for more advanced ones (such as the positioning stages) or more compact devices for improved integration, as shown in further chapters.

The critical elements of the setups, the LED array and the SPAD sensor, are controlled by an FPGA which generates the control signals and interfaces with computers where data will be processed and displayed. The interconnections between boards, which are already summarized in figure 3.8, are shown with more focus on figure 3.9. In that figure, connected to the Zedboard development board with the FPGA, the Daughter Card holds the auxiliary electronics and power stages. To it connect the SPAD PCB, which holds the 16 x 16 10 μm SPAD array camera chip as well as the LEDs drivers PCB, which at its turn connects to the LED chip.

The SPAD PCB and the LEDs driver PCB are connected to the Daughter Card by coaxial cables with 50 Ω impedance for more flexibility during the microscope assembly. The LEDs array Chip PCB is attached directly to the LEDs discrete driver PCB with a board to board connector or ball bonded on it.

3.4.1. FPGA based system controller

The system controller for the first prototype has been implemented on a Xilinx Zynq@-7020 All Programmable SoC, integrated into a commercial development board. The Zynq 7020 SoC was chosen for its flexibility since it combines a processing system (PS) based on a dual-core Cortex-A9 ARM processor with plenty of communication peripherals and which is directly connected with a programmable logic (PL) part, based on Artix-7 FPGA. This allows a fast development cycle, with plenty of options to reprogram and change the system as required while developing the microscope prototypes. Additionally, the Zynq 7020 architecture allows the inclusion of internal TDCs, useful for example for using SPADs for time-of-flight

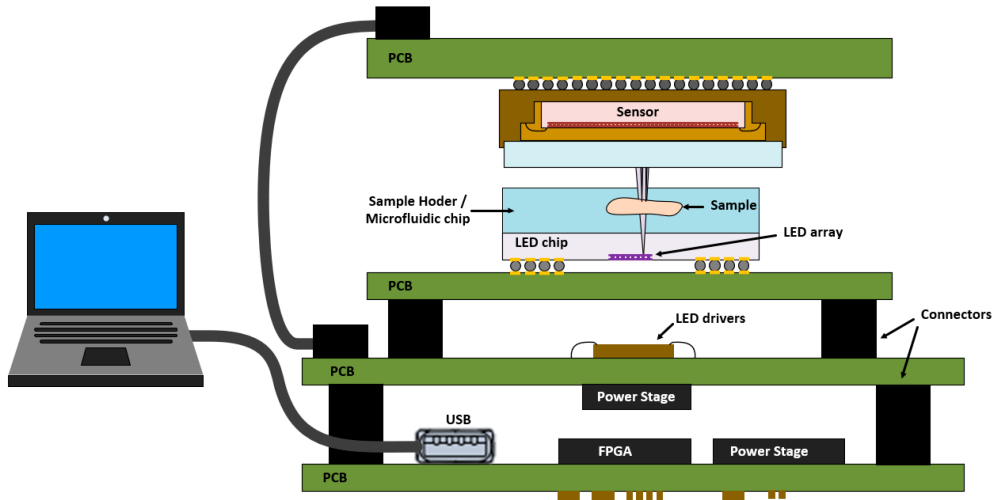


Figure 3.8: General schematics of the setup of the NIM microscopes. The LED array is ball-bonded over the driver PCB. The sample is placed over the LEDs as close as allowed by the sapphire substrate of the LEDs. The light transmitted through the sample reaches the SPAD sensor opposite the LEDs.

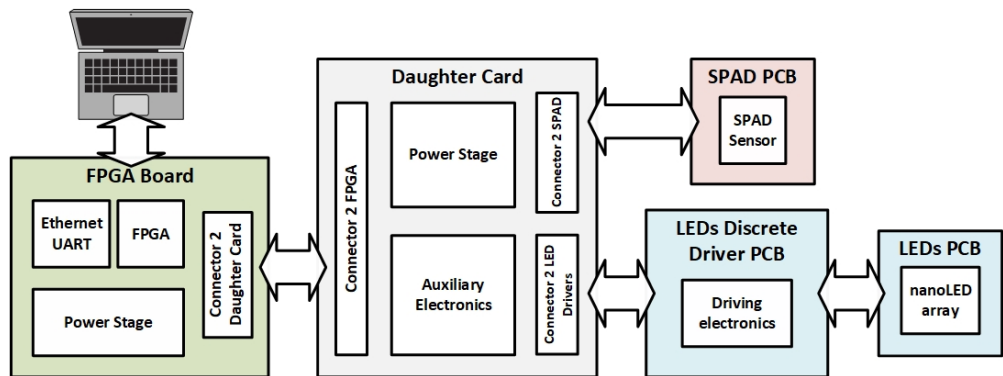


Figure 3.9: PCB level schematic of the architecture of the NIM system, with the components contained within each PCB detailed.

measurements [5].

Initial iterations operated with software programmed in C language running directly on one of the ARM cores and interfacing with an external computer through a UART - USB port. Data and control commands were sent through this connection. However, we soon realized a system running a Linux distribution on the ARM cores would be more flexible and would be able to run some initial data treatment, compressing them and reducing the amount of data sent externally. Therefore, we incorporated a Petalinux distribution from Xilinx on the PS of the FPGA, using the memory and peripherals included in the development board. This Linux distribution comes with the software drivers required to interface with the onboard Ethernet, which substituted the USB as the communication system with the PC by implementing a server/client TCP-IP protocol. Python was used to run the necessary scripts on the hosted Petalinux, as well as on the client computer to plot the results and offer a GUI to the user to control the microscope setup. The Python scripts also interfaced at a low level with the memory-mapped system control hardware in the FPGA, serving as a bridge for communicating data and control signals between the computer and the microscope.

The PL implements the measurement controller, which includes SPAD controller and the LED array addressing.

The basic block diagram of the control system implemented on the Zynq SoC can be seen in figure 3.10, consisting on:

1. SPAD array controller, generating the control signals to operate the SPAD array chip.
2. LED array controller, similarly generating the driving signals for the LED drivers.
3. Control Unit, a Finite State Machine in charge of controlling the measurement procedure, activating and keeping synchronized the SPAD and LED controllers, and allowing the communication with the PS parts of the system.
4. Delay chain based TDC with 68 ps resolution. Using a coarse counter extends the measurement range up to 433 ns in the implemented version, though it would be easy to extend it further.
5. Encoder and histogramming logic, which translate the TDC measurements into a histogram of times of arrival to offer a TCSPC result. If the arrival time is of no interest, the memories can instead accumulate the counts received by the sensors, operating as a conventional camera for intensity measurements.
6. Configuration registers implemented to interface with the microscope control logic implemented in the PL. They are used to select between operation

- mode and set measurement parameters such as the total number of SPAD measurements, the delay between them...
7. ARM CPU cores, which run the operating system as well as the scripts to receive the configuration and control parameters of the experiment and process the results to send them to the client PC. The PS interfaces with the faster logic implemented in the PL through the Advanced eXtensible Interface (AXI) bus.
 8. Interface with the external PCBs of the setup through the FPGA Mezzanine Card (FMC) included on the Zedboard. This connector allows high-speed signals of up to 2 Gbit/s, and the main Zedboard PCB supplies 1.8 and 3.3 V power lines through it.

3.4.2. Software

Both the back-end and GUI were fully developed in Python3. The GUI interface shown in figure 3.12 as well as those used in later versions of the microscope, were developed using the QT5 toolkit for Python3 programming language. The flexibility of Python and the implementation using object-oriented programming allowed the addition of new features into the software when required.

The software is capable of using two operation modes to produce the images. The first one is a camera mode, which uses either the SPAD array or any other CMOS camera as a traditional image sensor, which helps explore the sample as in a conventional shadow imaging setup, allowing to localize the areas of interest. The second mode of operation is the NIM mode, in which the images are generated by switching on the different LEDs. Figure 3.11 shows how the final image is built from the light measured from each LED: the sample is scanned by alternatively turning on the LEDs of the array. Each one projects the shadows from the sample into the sensor. Finally, the intensity of light measured in the region of interest on the sensor is stored, and the values are distributed on an 8×8 array in which each intensity value is the intensity of light reaching the sensor when the corresponding LED has been turned on, as shown in figure 3.11 c).

The software can get snapshots or stream video in both its operation modes. It also includes the motion control of the piezo-motorized stages used to move and position the microscope parts for the later setups with automatized positioning stages. Other features are access to all the control parameters of the cameras and LED array, SPADs and LEDs equalization, saving and loading calibration files for LEDs, SPADs and control of the piezo-actuators.

Figure 3.12 shows a screenshot of the implemented Graphical User Interface (GUI) frontend for the microscopes using the SPAD camera. The main part of the window shows the image from the 16×16 pixels sensor, with the colour bar indicating the number of counts. The frames per second are also shown above the acquired

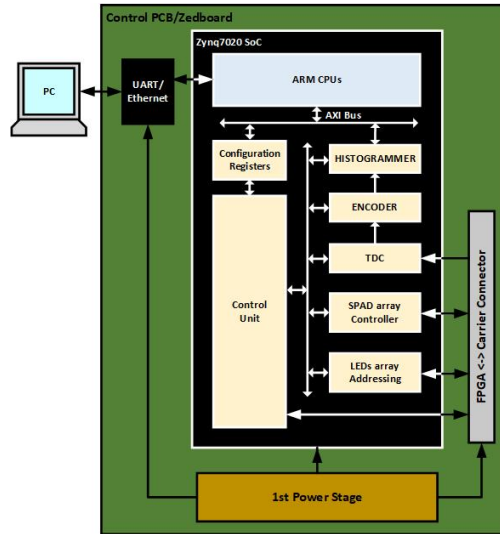


Figure 3.10: Simplified block diagram of the System Controller Implemented in the SoC.

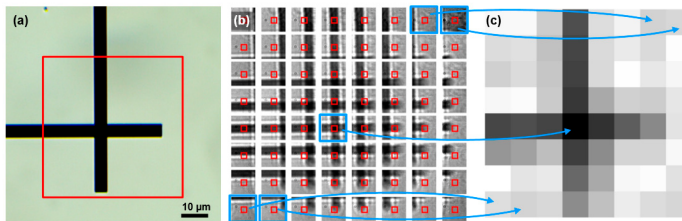


Figure 3.11: Algorithm for the construction of a NIM image: a) shows the image of the intersection of two $5\ \mu\text{m}$ lines from the target sample presented later, obtained with a conventional optical microscope. b) shows a mosaic of images captured by a NIM setup when that sample is illuminated by each LED of the 8×8 array. From each of those shadow patterns, the intensity of the area shown in red is stored. Then, this value is used to build the pattern in c), which is the NIM shadow image showing the intersection of the metallic lines as expected.

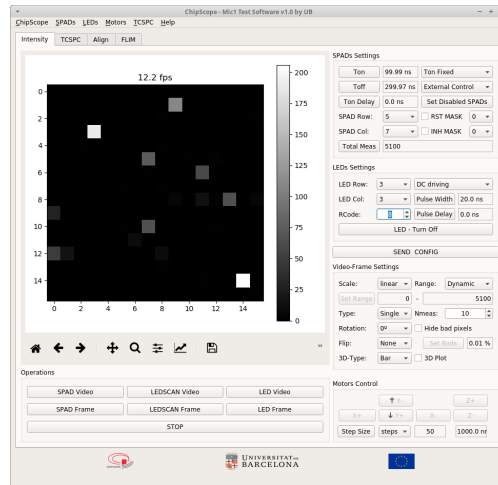


Figure 3.12: GUI interface for the microscope control software developed to test the prototypes.

image. Below this image, the array of buttons labelled as “Operations” control the acquisition method: using the whole SPAD array for conventional shadow imaging or scanning with the LEDs for NIM microscopy. Finally, at the right side of the GUI, the buttons and text field control the acquisition parameters and the motor movement.

Before acquiring images, it is necessary to equalize the emission of the LEDs, which present considerable variations on emission despite being driven by the same current due to the technological process [6]. This affects the contrast of the resulting image of the sample, as can be seen in the raw image in figure 3.13a. For the experiment to produce the image, we applied the same current to all LEDs without introducing any sample in the microscope. As can be seen, very different count levels are present in the image, while we would expect all pixels to measure the same amount of counts in the absence of a sample.

The calibration process has two steps: the first is a hardware calibration, switching each LED on and modulating the current on each until we measure the same light intensity on the SPAD sensor without any sample placed in the microscope. This hardware calibration reduces the relative variations between the light reaching the sensor from each LED to less than 10%, as can be seen in figure 3.13b which shows the result of applying this correction to the LED array shown previously.

The second calibration step is done by software by taking the intensity applied to one of the LEDs and the number of counts it triggered on the SPAD sensor as a reference and scaling the rest of the measured values to obtain the same intensity on each without any sample. With software calibration, the relative variations are reduced to below a 3%, shown in figure 3.13c.

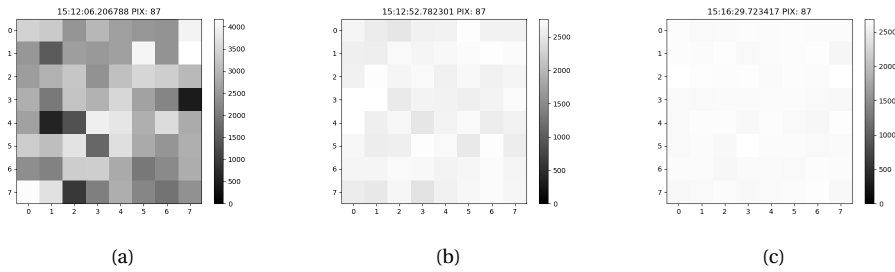


Figure 3.13: LED equalization sequences showing (a) a RAW LED image without any sample present, applying the same current to each LED, (b) image after hardware calibration and (c) image after software calibration applied on top of the hardware values.

3.5. The first microscope prototype

3.5.1. Design

The first microscope setups consisted of off-the-shelf positioning stages and optical bench elements from Thorlabs, which allowed to study image formation in the microscope and offered plenty of flexibility to explore the required characteristics of the setups.

3.5.1.1. Daughter PCB Card

The daughter card, drawn in grey in the schematic of figure 3.9, serves as the interface between the Zedboard and both the SPAD Chip PCB and the LEDs Discrete Driver board. This PCB supplies power to both the sensor and the light sources. To make testing the system easier, power levels are made available in several test points, and additionally, a selector allows switching between using an external power supply unit or the internal circuit.

The internal power is drawn from the 3.3 V level provided by the FPGA board, and a step-up converter is used to convert those 3.3 V to 25 V, which are to be used as the HV for the SPAD array. Before that, this high voltage is filtered through two regulable low-dropout regulators. Besides providing a stable voltage level, critical to ensure a constant response in time from the SPADs, these allow adjusting the voltage between 4V and 24V.

Since the final aim of the microscope is to observe living biological samples, temperature control elements were included. While the temperature itself was to be set through a hydraulic temperature stabilizer, such a system requires feedback from as close as possible to the sample to ensure the correct temperature was set. To do so, the LED boards included a PTC thermistor. Its output is read on the daughter PCB Card by the included ADC.

As explained when introducing SPADs, temperature plays an important on the noise figure of these sensors, significantly increasing it. In order to mitigate it, the SPAD boards were designed with a Peltier TEC module to lower the temperature of

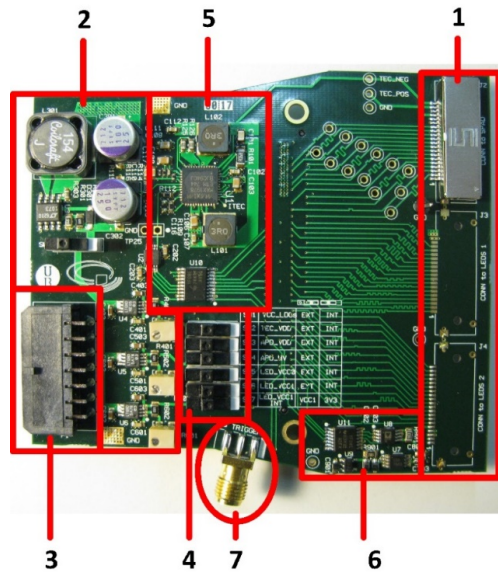


Figure 3.14: Top view of the daughter PCB board, with the important components highlighted and numbered

the chip. This Peltier module is also driven from this daughterboard.

The board itself can be seen in figure 3.14, with the parts highlighted and detailed below:

1. The connectors for the SPAD array and the LEDs discrete driver boards. All lines are 50 Ω impedance with controlled delay.
2. Power stage to generate the bias voltages required by the SPAD ASIC and LEDs drivers.
3. Power Supply connector to supply the required voltages from external sources.
4. Power switches to select if a voltage is biased by internal power stage or external power source.
5. The MAX1978, an integrated temperature controller for a Peltier TEC module on the SPAD board.
6. ADC to measure the temperature on the LEDs board.
7. SMA connector for a general propose with 50 Ω impedance line.
8. FMC connector to Zedboard positioned at the bottom side of the board.

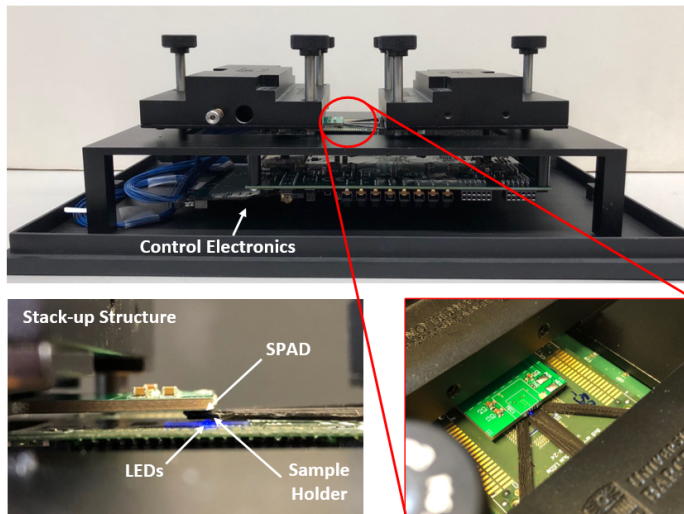


Figure 3.15: Picture of the improved custom microscope setup with all electronics integrated, with detail of the stack-up structure composed by SPAD sensor, Sample and LED array.

Once the requirements for the setup were better known, we were able to develop a more streamlined version for it which consisted of the same basic parts (8 x 8 5 μm LED chip, LED drivers, 16 x 16 10 μm SPAD camera, sample holder, control electronics and manual translator stages) but contained everything in a compact box of size 12 x 21 x 31 cm^3 . This dimensions are defined basically by the Zedboard development board and the positioning stages, as can be seen in figure 3.15. Not shown in the figure is the covering lid, which closes the setup into a box to remove any interference from external light sources. In this setup, the sample rests on the sapphire substrate and can be moved through the sample holder, while the camera on top has full three-axis of freedom for movement. The setup has been fabricated by 3D aluminium computer numeric control machining.

This system was designed to make it easy to change the sample holder in order to be able to adapt it to different kinds of samples to study. Figure 3.16 shows different sample holders designed and 3D printed in our installations, each aimed at supporting a different kind of sample, from the circular shapes of the mesh grids in figure 3.16 (A), the elongated but thin shape given to the wafers holding the EBL patterns used as test targets when cut in figure 3.16 (B), to a holder designed to accommodate an entire microscope glass slide in figure 3.16.

3.5.1.2. LED Drivers

The LED driving circuit is shown in figure 3.17 and consists of a current source, an analogic demultiplexer with eight channels that selects to which LED the current is directed, and a bipolar transistor that cuts or enables the selected LED. Each of these circuits drives a row of the array, and so it is replicated eight times to address

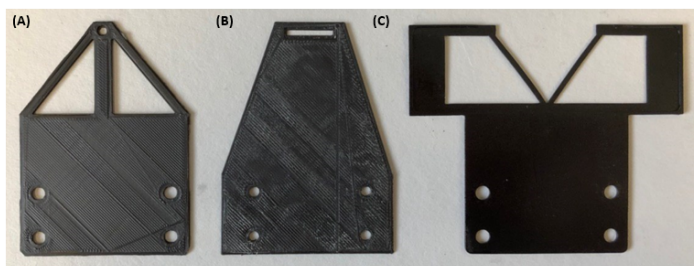


Figure 3.16: 3D-printed samples holder for (A) mesh 400 grid (B) EBL pattern and (C) microscope slide.

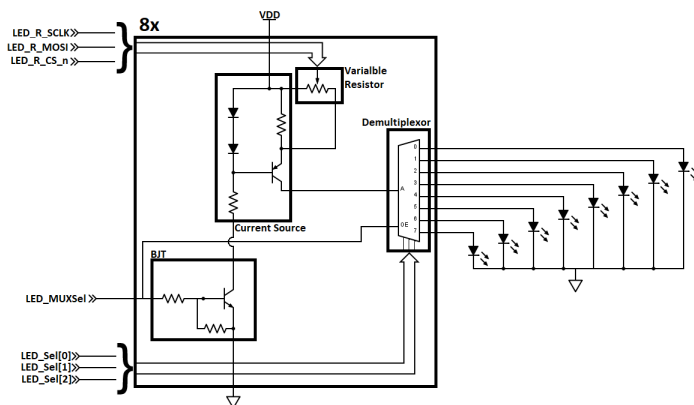


Figure 3.17: Schematic of the direct addressing LED driver circuit implemented for the first prototype. Note that the circuit addresses a row of the LED array, so it is replicated eight times. The control signals are driven from the FPGA.

the entire LED array. This would allow driving up to 8 LEDs, one at each row, at the same time if desired.

The current source provides a stabilized output current between 27 μA and 3 mA, selected by the value of the variable resistor (R_{VAR}), according to equation 3.5.

$$I_{\text{out}} = \frac{0.617}{R_{\text{VAR}}} + 15\mu\text{A} \quad (3.5)$$

This value of the variable resistor is digitally controlled and has 256 possible values, which are set from the FPGA board and allow for varying the current through each LED to, for example, compensate different emission levels, as shown previously in the Software section.

Figure 3.18 shows the two sides of the PCB fabricated to implement the circuit shown in figure 3.17. At the bottom side (left), there are most of the Integrated Circuits (ICs) of the circuit, as well as the connector for the coaxial cable to the daughterboard. The top side (right) shows the PCB with the smaller LED PCB holder con-



Figure 3.18: Picture of the implemented PCB with the LED driving circuit for the direct addressing nanoLED array. Left, bottom side with the different ICs. At the right, the top side with the nanoLED PCB connected.

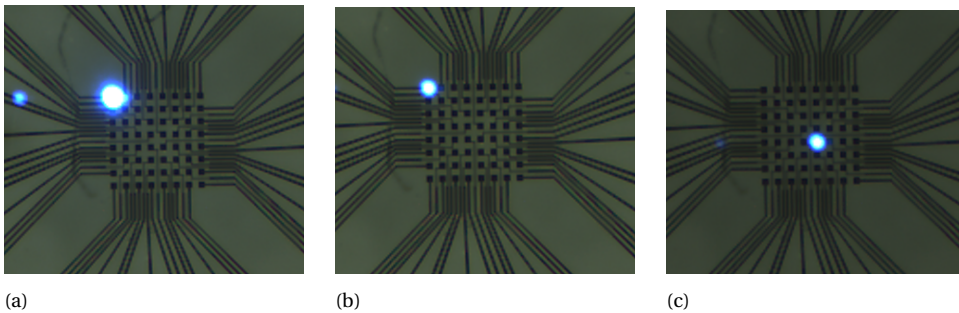


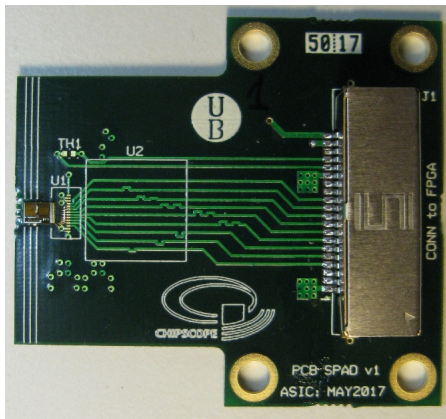
Figure 3.19: Picture of the μ LEDs being driven by the circuit at different currents. In a), the LED with coordinates A1 (first column, first row) driven by $500 \mu\text{A}$. In b), the same LED being driven by $27 \mu\text{A}$. In c), LED E5 is driven with the same current.

nected on top, in the final structure that is used in the prototype. The metallic pads at the side of the LED PCB allow access to each node to test for voltage levels and the driving pulses.

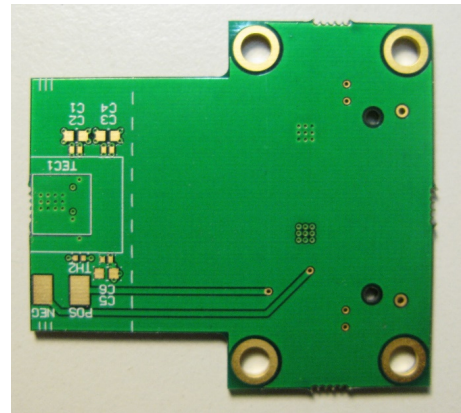
Examples of the resulting LED emission are shown in figure 3.19, in which three μ LEDs are driven at different currents: in figure 3.19a, the first LED of the array is driven with $500 \mu\text{A}$. Figure 3.19b shows the same LED when conducting $27 \mu\text{A}$, which is the same current used in figure 3.19c to drive another LED of the array.

3.5.1.3. SPAD PCB

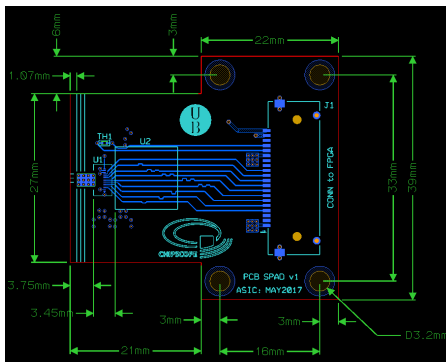
Meanwhile, figure 3.20 shows the PCB designed to hold the SPAD camera. On the top side, at the very left of the image, SPAD array ASIC can be seen, with the three white lines added to help in alignment procedures. Additionally, the connector to FPGA (J1) and an NTC thermistor to monitor the temperature (TH1) of the PCB are shown. Furthermore, on the bottom side, there is a Peltier TEC module with a



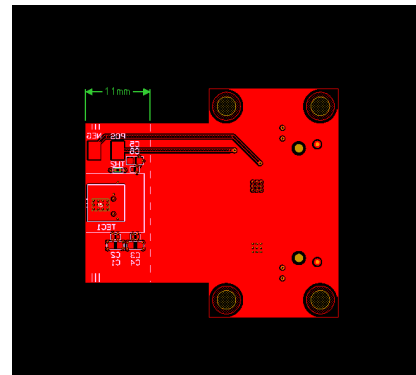
(a) Top picture



(b) Bottom picture



(c) Drawing with PCB dimensions, top



(d) Drawing with PCB dimensions, bottom

Figure 3.20: Pictures and drawings of the PCBs designed for testing the SPAD camera

heatsink grating (TEC1) and the decoupling capacitors required by the ASIC. The PCB was designed to be inserted easily into the microscope, offering a small and thin profile on the detector zone and leaving the interconnections and thick components on the outer side, which will not be introduced into the microscope.

3.6. Results of the first prototype

As a scanning transmission microscopy technique, NIM setups offer information about the first surface light encounters on its way from the LED to the sensor. This means that thick samples should be avoided since the first layers of material would block all light. As a result, the samples should be either highly transparent or, at the very least, thin enough so that no relevant information is lost.

To begin with the validation of the microscope, we designed a set of target patterns. It has structures ranging from some optimistical 50 nm up to 20 μm . They

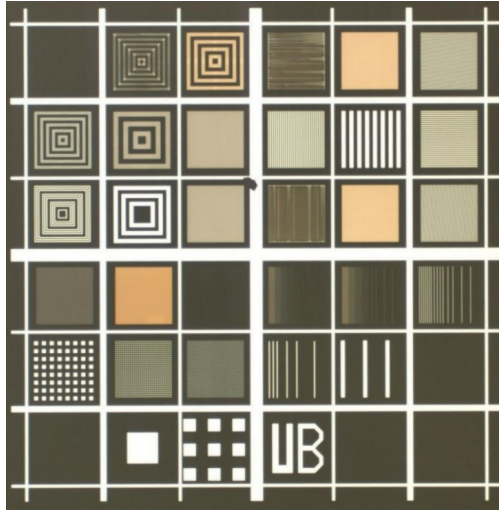


Figure 3.21: Picture of the EBL patterns. The pattern is divided into square sections holding the different designs and loosely grouped in families by quadrants.

were etched on aluminium through Electron Beam Lithography (EBL). A fused silica wafer was used as a substrate for the pattern (0.525 mm thick). After a process of dehydration, a 20 nm thick layer of aluminium was evaporated onto the wafer, then covered by a positive photoresist and spun and cured. A 2 nA electron beam was used to carve the patterns, and the loose aluminium was then removed with a single bath of tetramethyl-ammonium hydroxide solution. The sample was at last protected with the deposition of a chromium layer.

The resulting patterns can be seen in figure 3.21, and is a square containing all the targets in is $800 \times 800 \mu\text{m}^2$. Each target pattern family is enclosed within each of the $110 \times 110 \mu\text{m}^2$, the most evident of which shows etched the “UB” letters for Universitat de Barcelona.

At the lower-left quadrant of the EBL chip shown in figure 3.21 are contained groups of squares of different, decreasing sizes. At the top left quadrant, lines with different widths form concentric squares at varying frequencies. The patterns on the right half consisted of straight lines of different sizes, some with different pitches in the lower-right quadrant.

3.6.1. Results

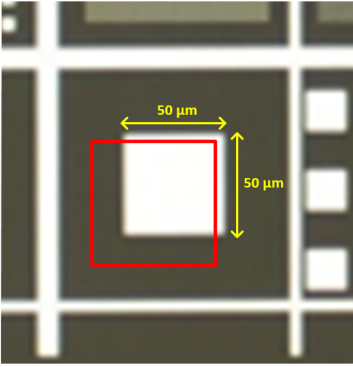
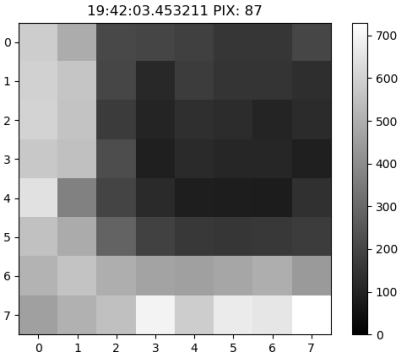
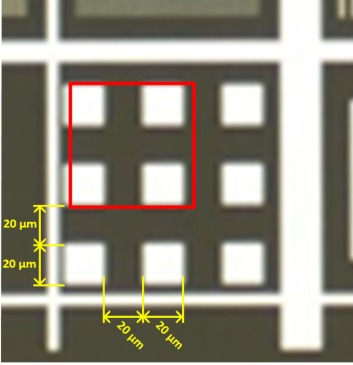
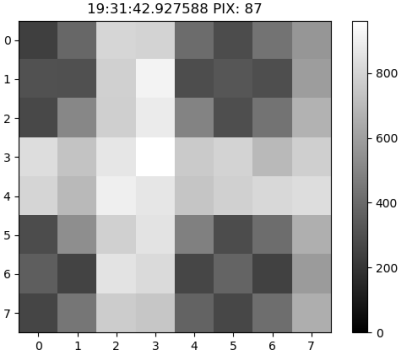
Table 3.1 shows the images obtained from different regions of the EBL pattern used as the sample, comparing between the one acquired with an optical microscope (on the left, with the relevant section highlighted in red); and the NIM image taken by measuring the light arriving on a single SPAD of the array, using the first prototype setup.

Since NIM is a transmission method, the metallic parts block light and appear

dark as opposed to the conventional microscope setup, which reflects light on the sample and thus shows the metallic parts brighter.

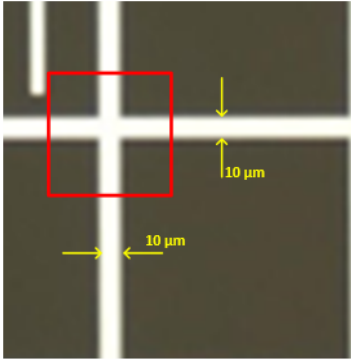
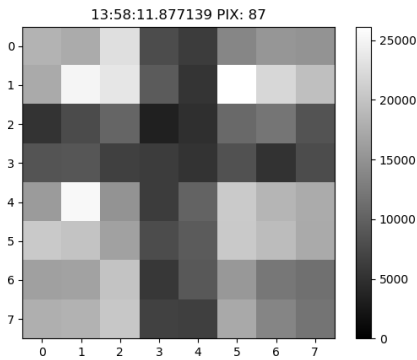
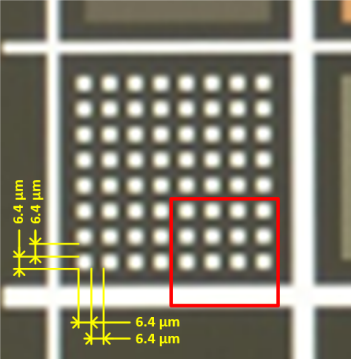
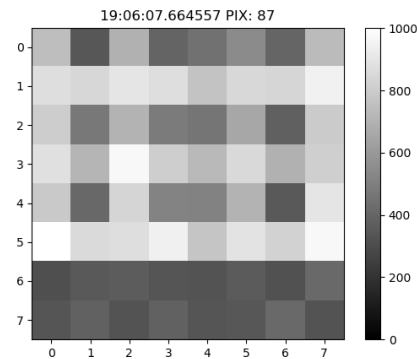
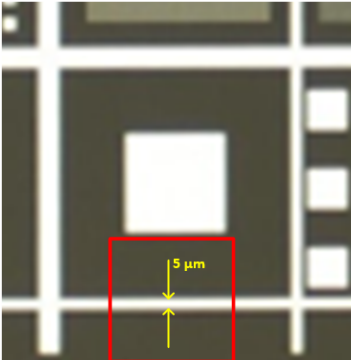
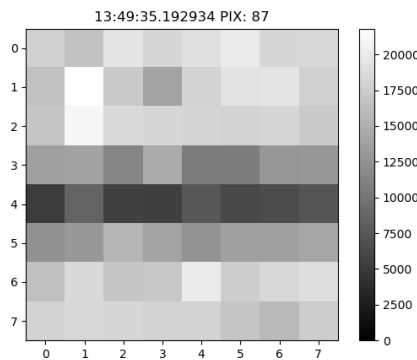
The number of pixels of the NIM images is low since that is the form factor of the LED array. As such, the images have only 8×8 pixels. Nevertheless, some shapes can still be observed, allowing the microscope to be validated. An example would be image 3.1, which shows the aliasing of the samples under the scanning exactly as the simulations predicted.

Table 3.1: Comparison of the same regions of the sample observed through an optical microscope (using reflection, so the metallic bars are bright since they are illuminated) and observed by NIM. Sizes of the zones of interest are indicated.

Optical microscope image	NIM microscope image
	
	

Continued on next page

Table 3.1 – *Continued from previous page*

Optical microscope image	NIM microscope image
	<p>13:58:11.877139 PIX: 87</p> 
	<p>19:06:07.664557 PIX: 87</p> 
	<p>13:49:35.192934 PIX: 87</p> 

3.7. Conclusions

In this chapter, we have established the theoretical principle for NIM microscopy and explored the guidelines for building an operational prototype. Finally, we show how that initial prototype has been constructed and take the first measurements with it, which allows us to validate the principle and better understand which areas require more work in further iterations of the technique.

We established that a NIM microscope has a field of view basically of the same size as the LED array used to illuminate the sample. So while the initial setup used a small array, there is plenty of potential to use large ones to explore larger fields of view.

The resolving power depends fundamentally on the pitch between LEDs since this is equivalent to the sampling period in time-based sampling theory. Confirming this makes the NIM technique interesting since the miniaturization of LEDs is an active field of investigation, and each new success on it directly improves the resolving power of NIM setups.

While the pitch between LEDs provides the sampling period over the sample, in a real application the resolving power must take into account the contrast of the image taken, which is significantly degraded when the sample is placed further away from the point of emission of light on the LEDs. The ideal case would be to have the sample directly over the zone of emission of the LED devices, but this is not possible due to the necessary connections and the passivation and protection layers necessary to give stability to the LED array chip. Therefore, it will be critical for this technique to develop to make this layer as thin as possible.

We have shown the setup of the first NIM prototype, using 5 μm LEDs with a pitch of 10 μm . Despite the limited number of pixels of the resulting images (the LED array is only 8×8), it allowed us to validate the principles and guided the construction of the more advanced versions, which will be covered in the next chapter.

References

- [1] Euan McLeod and Aydogan Ozcan. “Microscopy without lenses”. In: *Physics Today* 70.9 (2017), pp. 51–56. ISSN: 00319228. DOI: 10.1063/PT.3.3693.
- [2] Alex Von Diezmann, Yoav Shechtman, and W. E. Moerner. *Three-Dimensional Localization of Single Molecules for Super-Resolution Imaging and Single Particle Tracking*. 2017. DOI: 10.1021/acs.chemrev.6b00629.
- [3] H. Nyquist. “Certain Topics in Telegraph Transmission Theory”. In: *Transactions of the American Institute of Electrical Engineers* 47.2 (1928). DOI: 10.1109/T-AIEE.1928.5055024.

-
- [4] C.E. Shannon. “Communication in the Presence of Noise”. In: *Proceedings of the IRE* 37.1 (Jan. 1949), pp. 10–21. ISSN: 0096-8390. DOI: 10.1109/JRPROC.1949.232969.
- [5] N. Franch et al. “A low cost fluorescence lifetime measurement system based on SPAD detectors and FPGA processing”. In: *Journal of Instrumentation* 12.02 (Feb. 2017), pp. C02070–C02070. DOI: 10.1088/1748-0221/12/02/C02070.
- [6] Margaux Vigier et al. “Very High Brightness, High Resolution CMOS Driving Circuit for Microdisplay in Augmented Reality”. In: *2020 IEEE 63rd International Midwest Symposium on Circuits and Systems (MWSCAS)*. Vol. 2020-Augus. IEEE, Aug. 2020, pp. 876–879. ISBN: 978-1-7281-8058-8. DOI: 10.1109/MWSCAS48704.2020.9184480.

4

Pursuing the Limits of NIM with LED arrays

After studying the basics of NIM in the previous chapter, the logical next steps are to search for the limits of the technique. Furthermore, with the aim set at trying to reach super-resolution capabilities by reducing the sizes of the LEDs, we also wanted to improve other characteristics of the microscope, for example, making it more compact.

The microscope components remain the same as presented before, but the experience acquired on assembling the prototype presented in the previous chapter helped streamline them and adapt them to the challenges that appeared while preparing the new setups.

One of the significant changes in these more advanced setups is the substitution of the SPAD camera by a commercial CMOS camera as a sensing device. The higher number of pixels makes it easier to explore the samples and locate the targets of interest within them, although the frame rates it can offer are lower than those of the dedicated SPAD camera. Another change is the inclusion of much better positioning stages. The ones used for the first prototype were suitable for the LED sizes and the corresponding expected resolutions, but experimenting with samples nearing the diffraction limit required better devices. At the same time, we realized they could be used to expand the FOV of the microscopes.

This chapter begins with presenting the setup developed in order to study how to obtain images with smaller LEDs while using the same array of $5\ \mu\text{m}$ LEDs used in the previous chapter. This is done by artificially reducing the size of the LEDs by using lenses.

After that, we will present the last of the microscope setups built in this thesis, constructed with LEDs smaller than Abbe's limit for the wavelength of the light they emitted. This setup does not use any optical elements, following the same con-

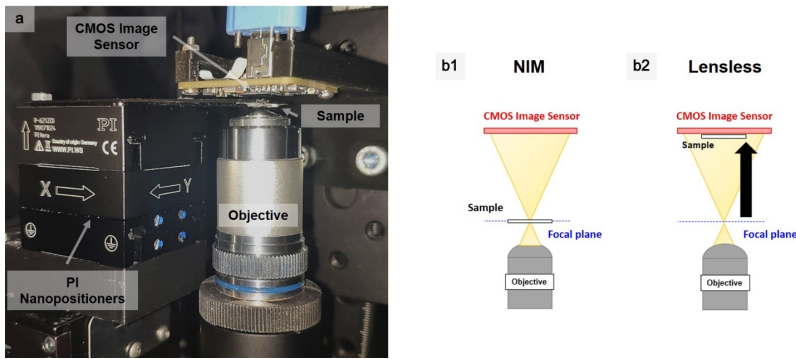


Figure 4.1: Light spot downscaling setup. a) Picture of the experimental setup built b) Schematic of the setup and its intents: figure b1 shows the setup operating in NIM conditions, while b2 shows the setup in conventional lensless mode for large FOV sample exploration.

cept as the one presented in the previous chapter but upgrading the components as necessary: more precise positioning stages are introduced in addition to the CMOS camera.

Finally, each section for the new setups includes the measurements obtained with them, and they are explained with the help of several simulations.

4.1. Reducing the light beam

To approximate how arrays of smaller LEDs would acquire images, we explored reducing the size of the light spot by using lenses. The intent remains to develop a lensless microscope, but the introduction of lenses to reduce the light spot is done with the intent of investigating potential new issues in the future microscope, as well as to kick off the work on extending the FOV of the microscope because since we downscale the LED array with the objective, the area scanned is reduced by the same scale.

4.1.1. Setup for light spot downscaling

4.1.1.1. Optical elements

The setup for optical downscaling of the light spot follows the same concept as the usual NIM approach but introduces an objective to create the reduced image of the LEDs that will act as the illumination source. This setup can be seen in figure 4.1 a). The x60 objective, with a NA of 0.85, is used to demagnify the LEDs as shown in figure 4.1 b).

The objective is placed (inverted) at 15 cm from the LED to produce the reduced image at the nominal focal distance. The 8×8 LED array used for this setup has a total size of $75 \times 75 \mu\text{m}^2$, which means that the reduced dimensions for the entire array are just $1.25 \times 1.25 \mu\text{m}^2$. Each $5 \mu\text{m}$ LED was expected to form a diffraction-limited spot of around 667 nm according to equation 4.1, where $\lambda = 465\text{ nm}$ and NA

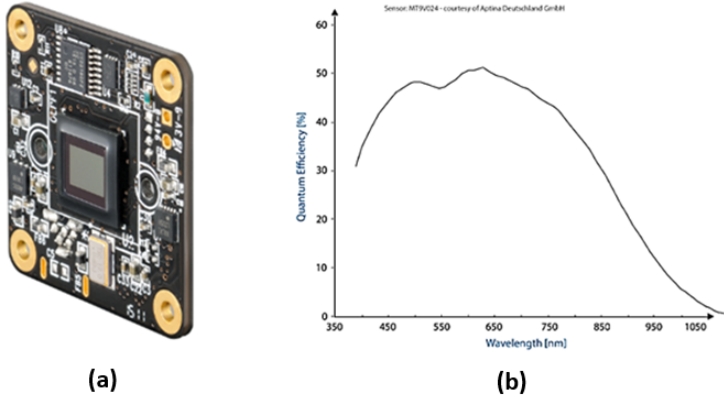


Figure 4.2: a), picture of the TIS-DMM-22BUC03-ML camera PCB. b) shows the spectral sensitivity for the MT9V024 sensor.

is 0.85 as told before.

$$D_{\text{spot}} = \frac{1.22\lambda}{NA} \quad (4.1)$$

4.1.1.2. CMOS camera

While the custom made SPAD camera had the best form factor for the setup and offered the best sampling speed, in order to have better flexibility when exploring the sample, we switched to a commercial CMOS camera. However, as previously explained, this should not be a critical issue since for NIM imaging, the requirements on the sensor are relaxed. So instead, we prioritized a more convenient form factor.

The camera used in further iterations of the microscope is a TIS-DMM-22BUC03-ML CMOS monochrome image sensor from the firm “The Imaging Source”. It integrates an Aptina MT9V024 sensor from OnSemiconductor, presenting a sensing area of $4.55 \times 2.97 \text{ mm}^2$ and a frame rate of 76 fps at a resolution of 744×480 pixels. It presents a quantum efficiency of 50% for the wavelengths of interest due to the LED emission. The pixel has an 8-bit dynamic range with a bit-serial data interface. Figure 4.2 shows the camera module in its low profile PCB as well as the sensor spectral sensitivity.

The high fill factor of the CMOS camera makes it easier to find the tiny light spot while scanning and exploring samples: the $70 \mu\text{m}$ separation between SPADs meant the light spot was easily lost while setting up and aligning the system. Furthermore, the high number of pixels makes the system even more flexible, easing alignment and capturing light from a wider area, which in the future can translate to new image acquisition strategies such as acquiring light from multiple LEDs at the same time without interference to accelerate acquisition.

4.1.1.3. Micropositioning stages

The addition of the demagnifying objective soon made evident that the previously used microscope setup had to be upgraded since it was very time consuming to locate the reduced light spot on the SPAD camera. This was done through a manual process susceptible to perturbations. In addition, exploring the sample by scanning and using the coarse positioning stages of previous microscope versions was also challenging.

The LED array is only $1.25 \times 1.25 \mu\text{m}^2$ in size when down-scaled through the system. This would be the total FOV of the setup, which is a very limiting value. However, the nanopositioning stages added to the setup help move beyond such limitation: larger LED arrays can be simulated by displacing the LEDs a known distance matching the LED pitch if the positioning stages have the required precision for it.

The piezo stages used for XY movement were the P-621.2CD from Physik Instrumente GmbH & Co, stacked on a vertical Z piezo stage P-621.2ZCD, also from Physik Instrumente. Both actuators have a resolution of 0.2 nm (though limited by a repeatability of 2 nm) and a total 100 μm travel range, with a positioning accuracy of 0.02%. We further expand the movement range using the same coarse positioning stage used in the initial setup.

The precision with which the stagers can be controlled opened the way also to simulate LED arrays with much smaller pitch distances between light sources. We do this by turning on a single μLED and moving it the desired distance, simulating the pitch between LEDs. Since the pitch is related to the microscope's resolving power, this immediately provides ways of testing the limits for the resolving power of these setups.

4.1.2. Measurements

The inclusion of the Z-axis piezo stage and the CMOS camera allows the setup to be switched from NIM to a conventional lensless setup as shown in figure 4.1. This eases the alignment procedure and exploring the sample to find the zone of interest: the entire camera, with that equivalent FOV, is used at first to explore in a conventional lensless setup. Once the zone of interest is located, the Z stage switches the system to the NIM version, placing the sample at the focal plane where the spot will have its minimum size, which might be diffraction limited.

As an example of the operation of the microscope, we observed the wing of a fly, shown in figure 4.3, which in a) shows a large part of the wing, using the large FOV of the classical lensless configuration (the sample was placed very close to the camera). Once the area of interest has been found and centred, the system can be switched into NIM configuration and used to scan the sample at higher resolutions. The results of doing so are shown in figure 4.3 b) and c): those are scans of the same area of the sample, highlighted in a). The images show how care has to be taken in placing the parts of interest of the sample on the same plane to take a proper image. This is not a surprise since it is a common problem in all scanning microscopy. The

difference between images b) and c) is a displacement of the sample of 2 μm on the z-axis, changing the focus of the image. The NIM images were obtained with a scanning step of 300 nm.

With this setup, we experimented with taking images from biological samples. One of the goals for the research project and this thesis always has been to study the suitability of imaging tissue or living samples. In this context, the team at the Medical University of Vienna provided us with lung tissue. This sample can be seen in figure 4.4 b), compared to a picture of the same tissue (but not the same zone) obtained with a confocal microscope in figure 4.4 a). They also identified the cell and its parts for reference and comparison between the two microscopes. As can be seen, our microscope can acquire images of biological samples. On the other hand, the image shown in figure 4.4 b) consists on 921600 pixels (distributed as 1920×480 pixels). The microscope's framerate is 26.7 FPS, with the main delay being the time required to activate the positioning stages and set them on the new location for each pixel. As a result, image 4.4 b) took above nine hours to be captured. This is slower than the optical alternatives but explainable because the focus has been on building an operating microscope to validate the technique without any optimization regarding speed.

The next logical step is to test for the limits of resolution of the technique, using smaller steps with the positioning stages while scanning the sample, to simulate an LED array with the light sources distributed with a smaller pitch. To do so, we recovered the EBL patterns previously presented. This time, we can scan smaller patterns thanks to the downscaling setup, and figure 4.5 shows the results of scanning the 800 nm square patterns at decreasing positioning stager steps.

Figure 4.5 a) shows the result of scanning with a step of 750 nm. As expected from previous work, the sample cannot be adequately acquired since the sampling step is of the exact dimensions as the sample itself (while Nyquist requires the step to be smaller than half the dimensions). The intensity measured will be heavily aliased: the squares appear to be sampled correctly along the vertical axis due to the scan's initial conditions and pure chance.

The image in 4.5 b) is almost correctly sampled, with a step of 400 nm. This step is precisely half the periodicity of the squares in the sample, which can all be distinguished with little detail. Figures 4.5 c) and d) use scanning steps of 200 and 100 nm respectively, showing how oversampling improves the image acquired. As a result, the squares are more easily recognized.

Imaging smaller samples using the customizable scanning step provided by the positioning stages was not successful. It was impossible to resolve smaller patterns than the ones shown. To understand why, we studied the limits of the system with the sharp edge test, imaging the edge of one of the square patterns in order to approximate sampling an ideal step function and obtain the Modulation Transfer Function (MTF) of the system.

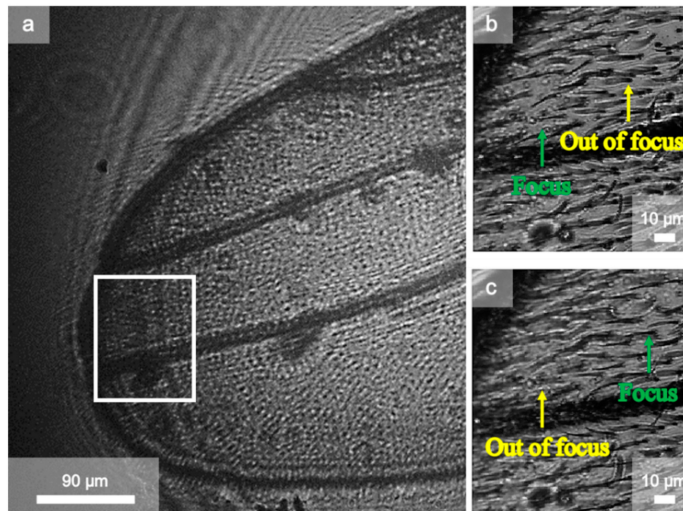


Figure 4.3: Images of the wing of a fly obtained with the spot downscaling setup. a) Image acquired in conventional lensless configuration. b) and c) images are detailed NIM scanning results of the area highlighted in a)

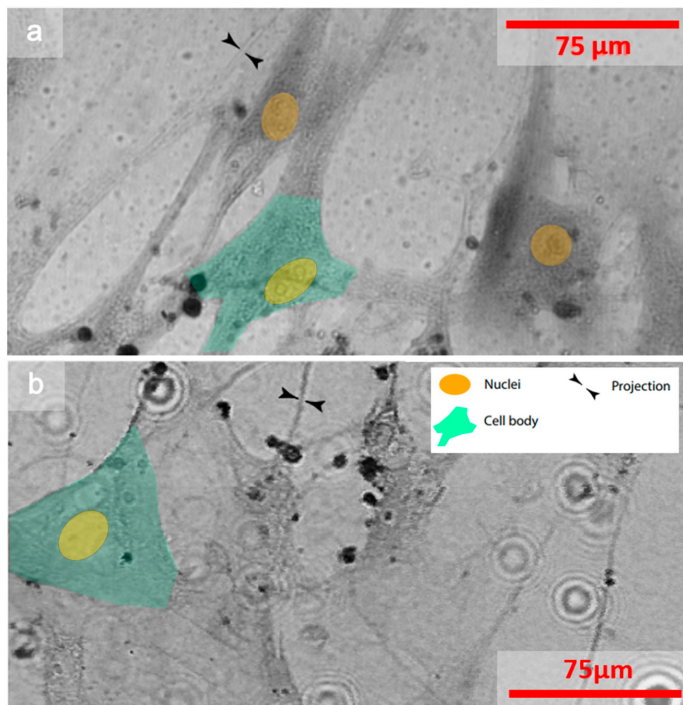


Figure 4.4: Picture of human lung fibroblasts obtained through (a) a confocal laser scanning microscope (CLSM) and (b) NIM setup with demagnification for comparison.

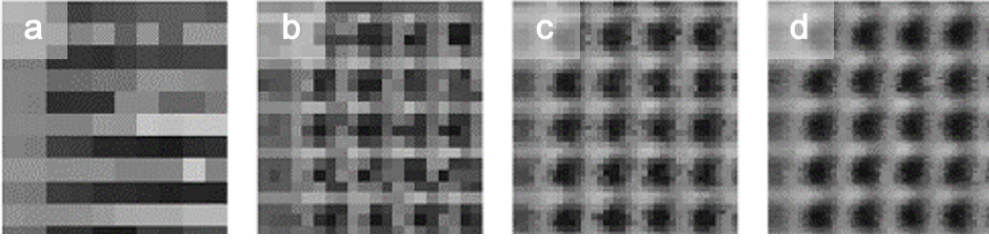


Figure 4.5: NIM images of the 800 nm squares with the downscaling setup. Images have been acquired with different scan steps: 750, 400, 200 and 100 nm respectively for a), b), c), and d).

4.1.2.1. Resolving power through Modulation Transfer Function

The resolution criteria have been introduced in the first chapter as guides to the limits of optical systems. As we have shown, both Sparrow and Rayleigh's criteria include the contrast of the image acquired through the instrument into the definition of the detail we can observe with it. The MTF of a system is a measurement of how well contrast is transferred from the object to the image, incorporating resolution and contrast into the same measurement.

Figure 4.6 shows an example of how contrast transfers from the object to the image formed. The contrast is transferred well to the image plane at the top row, with the objects more separated between them (and so lower frequency). The figures at the bottom row show how the contrast degrades for higher frequencies, with the image having reduced contrast.

Contrast can be defined, as a function of the spatial frequency s , as:

$$C(s) = \frac{I_{\max} - I_{\min}}{I_{\max} + I_{\min}} \quad (4.2)$$

From this definition, the MTF can be defined as:

$$MTF(s) = \frac{C'(s')}{C(s)} \quad (4.3)$$

In which $C'(s')$ is the contrast in the image plane while $C(s)$ is the contrast of the object. For a passive system, this function can take a maximum value of 1, meaning that for that given frequency, no information is lost.

An equivalent definition for MTF can also be obtained from diffraction theory and its relation with the Point Spread Function (PSF) of the system [1, 2]. Since it is difficult to obtain a PSF on a real optical system, a one-dimensional representation for it is used instead, the Line Spread Function (LSF), which measures the image formed by a line of infinite length but infinitesimal width. Since the condition of having a vanishingly narrow line (compared to its length) might also be difficult to accomplish in real objects, the LSF is often derived indirectly. The LSF can be obtained from the Edge Spread Function (ESF), which measures the response to a

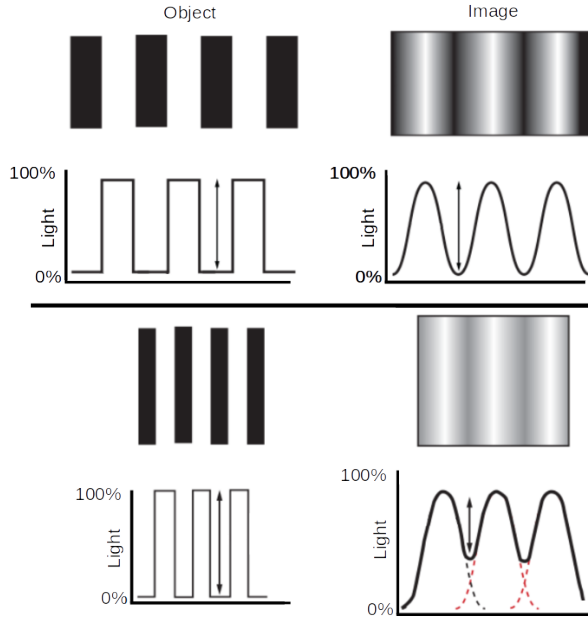


Figure 4.6: Comparison of the contrast of an object and its image through an optical system.

sharp edge separating a zone of total light transmission from another in which no light is transmitted. The ESF relates with the other Functions as shown in equation 4.4 [3].

$$\frac{d}{dx}[ESF(x)] = LSF(x) = \int_{-\infty}^{\infty} PSF(x, y) dy \quad (4.4)$$

Knowing that the LSF is a one-dimensional representation for the PSF, it can be used to obtain the resolving power of the setup by measuring the ESF. From that measurement, we can take the FWHM of the resulting LSF and apply Rayleigh's criterion for resolving two objects [4]. This allows us to evaluate the microscope on the images obtained from the EBL patterns presented before.

4.1.2.2. Application

The analysis based on the ESF is applied to the images shown in figure 4.5, and presented in figure 4.7. In it, the ESF is obtained by scanning into the squares of figure 4.5. Each dot of the figure 4.7 is the intensity of light received at each step of the scan. Each experiment using a different step is pictured in a different colour in the figure: red for steps of 400 nm, green for the experiment with the stepping of 200 nm and fuchsia for the 100 nm steps. To ease the visualization of the data, we apply an offset in the x-axis of the different datasets to separate them.

The dashed line shown in figure 4.7 is the result of normalizing and applying a moving average on the raw data to fit a profile, but to obtain the LSF the raw data

has been used. As explained before, the FWHM of the LSF provides the resolving power of the optical system, and in this case, as can be seen, that value remains constant for all three experiments despite the different step sizes used in the scan and is around 800 nm and shown in the inset legend of the figure.

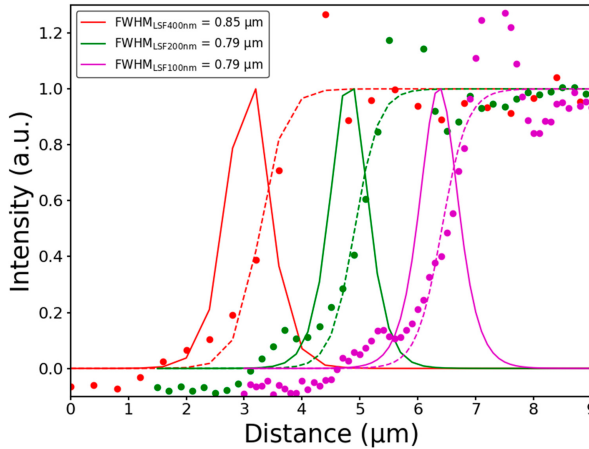


Figure 4.7: ESF measured on the EBL sample for different step distances, and LSF obtained from it. In red, data and results of scanning at 400 nm. In green, at 200 nm and in fuchsia at 100 nm. The data sets for different scanning steps have been offset for clarity, being at the same position before doing so. The inset of the figure shows the FWHM of the LSF for each measurement.

The step used in the scan simulates the pitch of a virtual LED array, so according to the theory presented in the previous chapter, we expect the resolving power to increase as we decrease the step distance. While the sampling frequency is improved by doing so, the system is not capable of transmitting the contrast beyond 800 nm, as shown in figure 4.7. Discussion of the reason behind this is offered later, after exploring the other approach to the resolution limits of this microscopy method: using smaller LEDs.

4.2. Reducing the size of the LEDs

The idea behind NIM is to ride on the possibility to produce smaller LEDs organized in dense arrays. As such, in the scope of the Chipscope European Project, new LED arrays were developed, pushing the size down and finding the technical limitations that have to be solved to drive this progress. This section is reported in the published reference [5].

In that context, the Braunschweig team developed the LED array shown in figure 4.8. This chip used a new methodology [6] which allowed the emission of light through the p-contact metal lines. This was done to reduce the distance between the LED and the sample in the microscope by avoiding the emission through the sapphire layer of the LED chip. As explained, reducing this distance is essential to

improve contrast and, with it, the resolving power of the device.

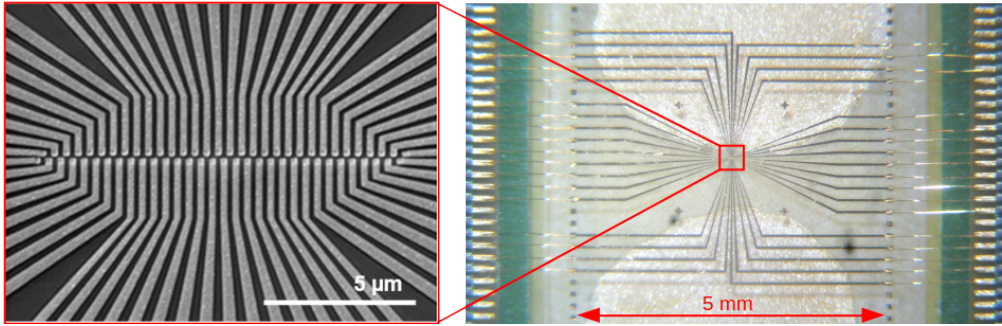


Figure 4.8: At the left, microscope picture of the 2×32 LED array of 200 nm and its connections towards the contacts, shown at the right image.

This LED chip was designed in the shape of a 32×2 array of 200 nm LEDs, separated 200 nm between them along the line axis. This design was done to test the limits of the LED fabrication capabilities without facing the difficulties added by routing a more complex array. Each LED is contacted directly to the driver PCB, avoiding the problems of having to connect an entire array with a single metal layer for routing. The design included two lines of LEDs. The distance between LEDs of the two lines is less than the 200 nm separating them along the longitudinal axis due to the relative displacement between the lines (visible in figure 4.8). As with the previous setups, the FOV is extended as necessary when taking an image by using nanopositioning stages.

4.2.1. Microscope Setup

The microscopes developed for using these LED arrays also evolved to a more streamlined presentation, building on the knowledge from the previous setups. These changes will be highlighted in the following sections.

4.2.1.1. System architecture

The size of the development board golding the FPGA to control the system defined the shape and size of the microscope presented in the previous chapter. The Zed-board included many peripherals that were not used, despite being convenient for fast prototyping and investigating additional aspects of the microscope, such as time-of-flight measurements.

With priority set on approaching small and cheap microscopes capable of being deployed in the field with ease, and fluorescence applications discarded for the moment, the control firmware of the system was ported to a smaller FPGA based on the much more compact DE0-Nano board.

The microscope system architecture has been kept entirely modular to ensure its flexibility so that each subsystem can be tested and even redesigned indepen-

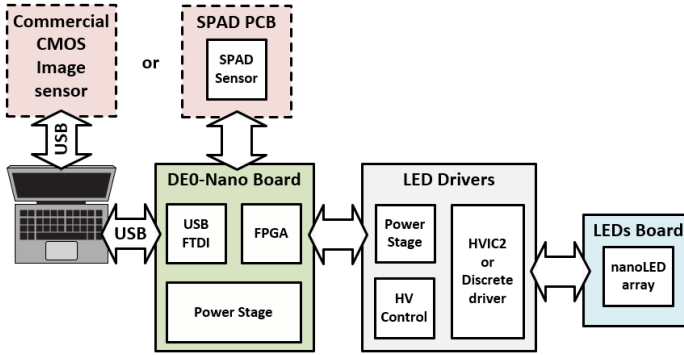


Figure 4.9: Schematic overview of the architecture of the new compact setup system at PCB level, with their interconnections.

dently and allow easy replacement of any part without compromising the rest of the system. The main components of the microscope on a board level and their interconnections can be seen in figure 4.9, and are:

1. DE0-Nano is a commercial development board where the system controller is implemented in the integrated FPGA, a Cyclon IV from Altera.
2. LEDs Drivers and auxiliary electronics such as the USB interface and the required bias stages.
3. LEDs board, which holds the nanoLED array chip from TUBS.
4. CMOS sensor. Efforts have been made in order to retain complete compatibility. The sensor can be either the integrated SPAD Camera or a board-level CMOS camera. In the case of using the SPAD camera, an additional auxiliary board is required to connect it to the DE0-nano, just as was the case with the microscope presented in the previous chapter.

The amount of control in the FPGA firmware depends on the sensor used. The SPAD camera is entirely controlled by the FPGA firmware. On the other hand, the CMOS camera has to be controlled from its proprietary driver software, from a PC connected to the board. LED control remains on the FPGA in all cases.

4.2.1.2. DE0-Nano overview

The DE0-Nano board, shown in figure 4.10, is a compact-sized FPGA development platform featuring an Altera Cyclone IV FPGA with 22,320 logic elements as well as 32 MB of SDRAM, 2 Kb EEPROM, and a 64 Mb serial configuration memory device. Other features included in the board are an 8-channel 12-bit A/D and a 3-axis accelerometer, both not used in this work.

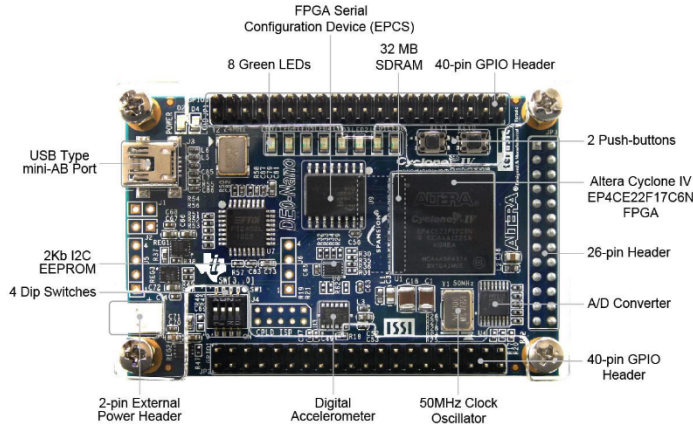


Figure 4.10: DE0-Nano Board PCB and component diagram

The board includes a built-in USB Blaster for FPGA programming and can be powered either from this USB port or by an external power source. For I/O connection, the board includes expansion headers that are used to attach daughter cards such as the ones designed for the microscope: the two 40-pin Headers (GPIOs) provide a total of 72 pins, 5 V power pins, two 3.3V power pins and four ground pins, with an onboard 50 MHz oscillator.

4.2.1.3. Discrete LED driver

The sub-micron LED array operated with a maximum current of $5\ \mu\text{A}$ and required nA precision steps for proper equalization while presenting a considerable dispersion of I/V characteristics, which further complicated setting the operation point and biasing of the LEDs.

While fully integrated CMOS LED drivers to use with these LED arrays were designed and fabricated within the context of the Chipscope project, they lacked the flexibility to incorporate external biasing or Pulse Width Modulation (PWM) for fine control and equalization of the LED emission.

Since the number of LEDs to drive is small (only 64), a discrete driver board operating in current mode was designed. This driver consists of a current sink composed by an operational amplifier and controlled with a Digital to Analog Converter (DAC), nMOS transistor and a resistance, and on eight demultiplexers to choose which anode is being driven, as can be seen in the schematic of figure 4.11. The driver allows controlling the current from 50 nA up to $12\ \mu\text{A}$ in 214 steps. In addition, the PCB was modified to drive at a voltage of 20 V. This was necessary to perform the annealing process required to lower the resistance of the LEDs. This annealing process requires increasing the voltage above 10 V while keeping the current below $5\ \mu\text{A}$ to avoid damaging the LEDs.

The fabricated driver PCB can be seen in figure 4.12. On the top side, the power

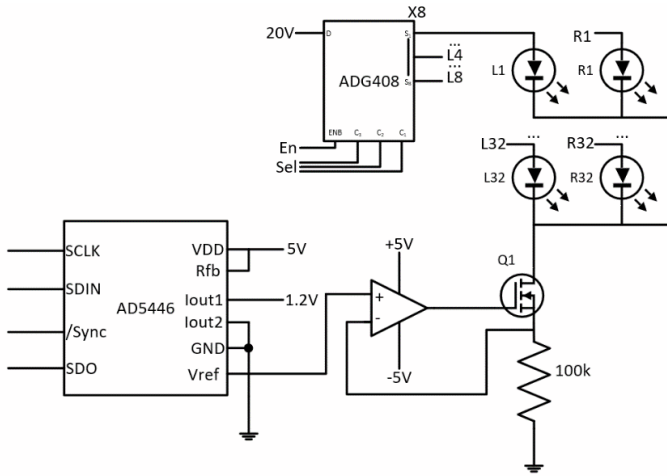


Figure 4.11: Discrete driver schematic. The driver consists of a current sink formed by the operational amplifier and the transistor Q1, which the DAC AD5446 controls. Since the array is directly addressable, eight demultiplexers select one of the 64 LEDs to control which LED is turning on.

stage area is marked in blue. It consists of a Linear Dropout Regulator (LDO) to set the input voltage from 2 V to 20 V, another LDO which provides the 5 V power line for the FPGA, and a circuit that generates the -5 V for the current sink operational amplifier supply. The PCB also contains an FTDI chip to communicate with the FPGA, marked in red, the electronics required to read the temperature sensor in the LED PCB (orange), the demultiplexers (purple) and the current sink itself (white). At the bottom side of the PCB, there are only two components of the power stage area (blue), test points (yellow) and the LED connector (green).

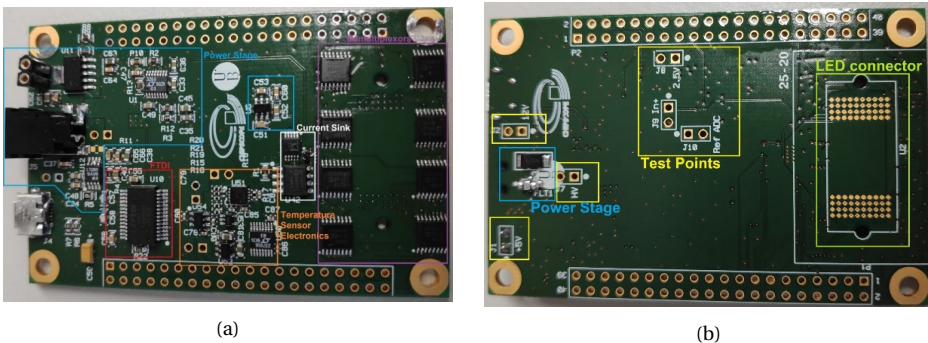


Figure 4.12: Pictures of the top and bottom sides of the implemented LED driver PCB for the LEDs used in the minimum sized LED microscope.

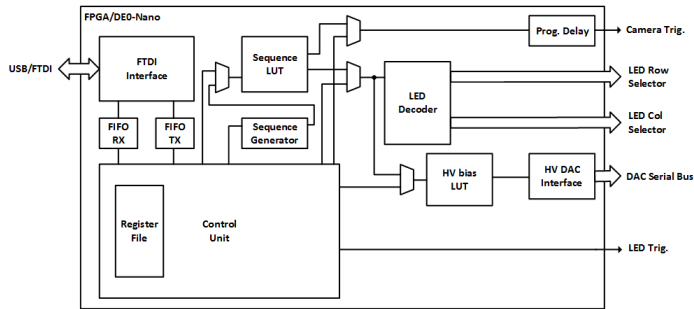


Figure 4.13: Block diagram of the control firmware implemented in the onboard DE0-Nano FPGA for the 200 nm microscope setup.

4.2.1.4. FPGA hardware

Figure 4.13 shows a simplified block diagram of the hardware controller implemented in the Cyclone FPGA on the DE-0 board. It includes programmable Look-Up Tables (LUTs) to upload predefined operation points, such as the HV bias for each LED of the array. This implementation is useful to reduce the number of bytes in the instruction codes necessary to change from one LED to another. The controller also includes a LUT where predefined LED turn-on sequences can be defined while keeping each LED’s on-time and turn-on delay independently programmable to give absolute flexibility to the tests. The system also has a trigger output to synchronize the camera acquisition with the LED switching on.

4.2.1.5. Software

The software from the microscope has been developed over the one created for the previous versions. We upgraded the functions and changed the GUI to draw the image from the commercial CMOS camera drivers. In addition, we added controls for the new options of the microscope, such as the annealing process. Figure 4.14 shows the GUI for this microscope as well as the following ones. The image areas dominate the right side of the window: the top part shows the raw frame captured by the CMOS camera, while the lower one shows the reconstructed NIM image. On the left side, the main control parameters can be accessed.

The implemented GUI provides access to the functionalities shown in table 4.1, which allow to control the microscope, save the configuration parameters and recover them later and do the same with the measurements taken.

4.2.1.6. Microscope setup

The microscope implemented uses the 32×2 directly addressable LEDs of 200 nm, and the CMOS sensor camera presented previously. The nanopositioner stages are a central part of the setup.

The microscope assembly consists of a stacked “sandwich” structure with the sample laying over the LED array chip and the optical sensor on top facing them, as

Table 4.1: Main microscope control functionalities implemented.

Function	Description
Real-time Image	Visualization of real-time video in either lensless shadow imaging or Chipscope modes.
Image capture	Single lensless and Chipscope image capture.
CMOS sensor settings	Control panel with the CMOS sensor parameters such as gain and exposure time.
LED settings	Control panel with the LEDs driver configuration parameters and to select how the LED are operated: with all the parameters set and controlled manually through the software or automatically loaded from included look-up tables.
Calibration	Equalize the emission of the LEDs. Three equalization factors can be enabled independently: HV bias, PWM modulation through period and duty cycle parameters or software scaling.
Save configuration files	Save the current state of all the control parameters of the microscope (camera settings, LEDs parameters including LUT data and image representation settings) in a configuration file.
Load Configuration files	Load a microscope configuration file with the camera settings, LEDs operation settings and LUT tables, and image representation settings.

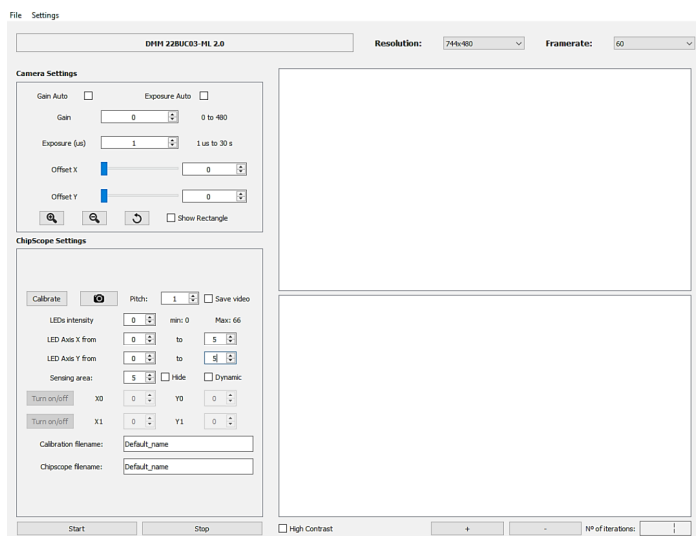


Figure 4.14: GUI interface for the software developed to test the microscope prototypes with the CMOS camera.

shown in figure 4.15. Solid samples can be placed directly on the LED array chip, minimizing the distance to the light-emitting sources held by the custom made sample holders. For increased precision, instead of using 3D plastic printed holders, we designed and fabricated the ones used in this setup in 3D aluminium CNC machining. The final dimensions of the microscope setup shown in the figure are $110 \times 87 \times 74 \text{ mm}^3$.

While having the same stack-up structure as the previous prototype, the PCB to hold the LED chip included a recess where that chip is inserted, providing an entirely flat surface to avoid bumps for the sample holder. Since the connection between LED and driver PCB is made through a low profile compression connector, the LED PCB has no other components than the array.

A relevant addition to the setup is the inclusion of the nanopositioners inside the microscope box and a micropositioning stage for manual coarse alignment of the sample with the system.

Table 4.2 details the components of the microscope with its characteristics, such as the size and their function.

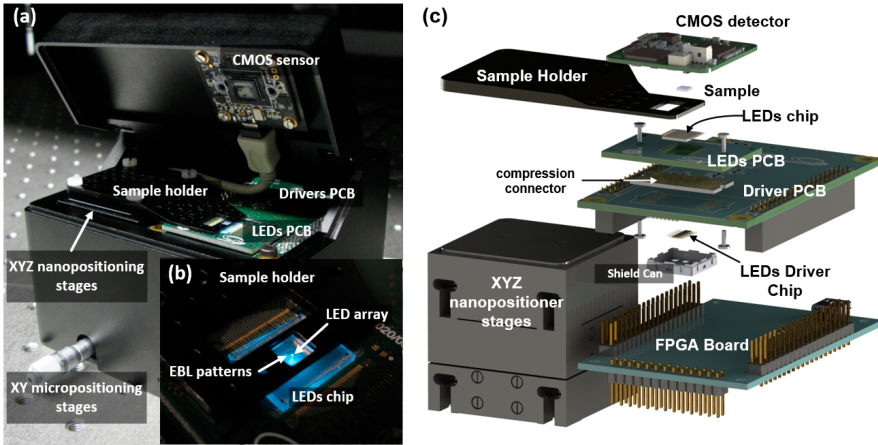


Figure 4.15: Setup for the 200 nm LED microscope. a) shows a picture of the microscope fabricated. b) shows a detail of the LEDs in use and sample placement. c) shows an exploded schematic of the setup pictured in a), detailing the parts.

Table 4.2: Overview of the microscope components

Component	Dimensions	Detail	Provider	Function
LED array	$12.8 \times 0.4 \mu\text{m}$	2×32 LEDs of 200 nm with a pitch of 200 nm and $\lambda = 525 \text{ nm}$	TU Braunschweig	Illumination of the sample with regular spacing, providing the sampling for the microscope
LED drivers	$49 \times 75.2 \text{ mm}$	Discrete drivers for 64 LEDs, min current = 50 nA, max current = 12 μA , max V = 17.5 V, Min t = 1.2 μs	UB	Driving and biasing of the LEDs with fast switching capabilities.

Continued on next page

Table 4.2 – continued from previous page

Component	Dimensions	Detail	Provider	Function
Camera	$4.55 \times 2.97 \text{ mm}^2$	Aptina MT9V024, 744×480 pixels, max 76 fps	Aptina / Onsemi	Measurement of the intensity of light from each LED, transmitted through the sample / shadow imaging for positioning
Micropositioning stages	$40 \times 40 \times 25 \text{ mm}$	P-621 2CD/2CL PIHera XY Piezo Stage, $100 \mu\text{m}$ travel range, 0.2 nm resolution	Physik Instrumente	Emulation of larger LED arrays, extending the FOV of the microscope. Sample positioning.
Case	$110 \times 87 \times 74 \text{ mm}^3$	Aluminium Computer Numerical Control (CNC) machining	UB	Protection and holding of components, light blocking
DE-0 Nano Board	$49 \times 75.2 \text{ mm}$	Using the USB interface for PC comms and connection headers for LED chip signals	Terasic	Control of the driving chip

Continued on next page

Table 4.2 – continued from previous page

Component	Dimensions	Detail	Provider	Function
PC	External to the microscope	Custom programmed software for measurement control	- / Custom software	Operation of the microscope, data storage/processing

4.2.2. Measurements

Despite the limited form factor of the 32×2 LED array, the precise movement of the nanopositioning stages allowed to simulate extended LED arrays with the same virtual LED pitch or even better. This was the strategy followed with this microscope version to obtain images and test its capabilities.

Figure 4.16 shows the image of a part of the EBL sample taken with an optical microscope. Shown at the right side of the image is the section with $6.4 \mu\text{m}$ squares, separated from the region of $1.6 \mu\text{m}$ squares at the right by a $10 \mu\text{m}$ line. Substituting the microscope image, the inset at the centre is the image taken with the microscope scanning the zone. This image was obtained by scanning with a step of 200 nm on both axes.

The contrast of the $1.6 \mu\text{m}$ squares of image 4.16 is poor compared to the images of smaller samples shown before (for example, the 800 nm squares of figure 4.5). These images were also obtained scanning with even larger steps of the nanopositioning stages, and so with theoretically lower resolving power.

To confirm this problem, we calculate the LSF and ESF of the image obtained by the microscope shown in figure 4.16, with the results shown in figure 4.17. The procedure is the same as in previous sections. The light intensity acquired has been normalized, and the LSF, shown as the red line in the figure, is calculated as the derivative (difference) between each data point measured (triangular dots in the figure). The FWHM of the LSF serves as resolution criteria for the setup, and the value obtained is $1.56 \mu\text{m}$. The value expected from only considering sampling theory would be of double the scanning step, 400 nm .

This considerable discrepancy has been traced again to the size of the light spot when reaching the sample [7]. This was also the issue in the light spot downscaling setup, and it limits the contrast and the resolving power of the microscope, something we further discuss in the next section.

4.3. Light spot shape

As shown in Chapter 2, the LEDs follow a cosine law in their emission, which means the cone of light increases in size rapidly when moving away from the emission point. This is why contrast (and so, resolution) cannot improve beyond a certain point despite lowering the sampling frequency provided by the pitch of the LEDs.

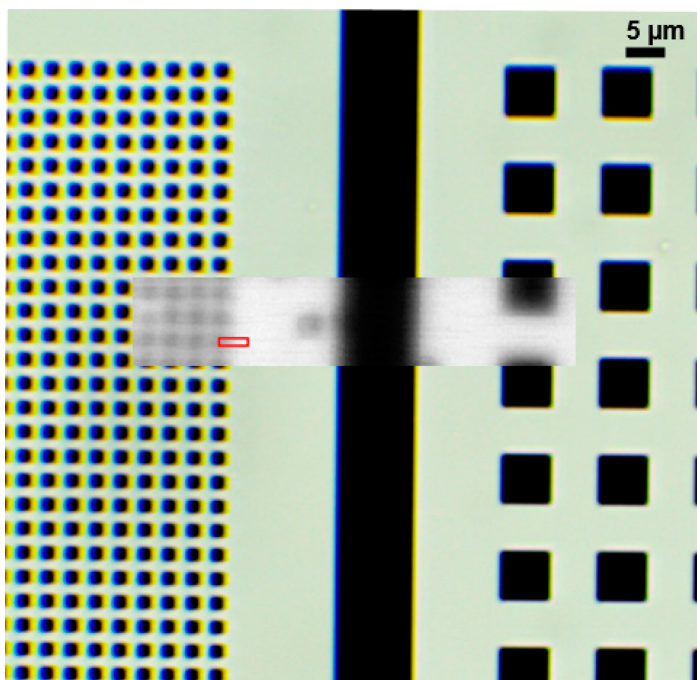


Figure 4.16: Optical image of the 1.6 μm (left) and 6.4 μm (right) squares of the EBL pattern, with the reconstructed image of the same region superposed.

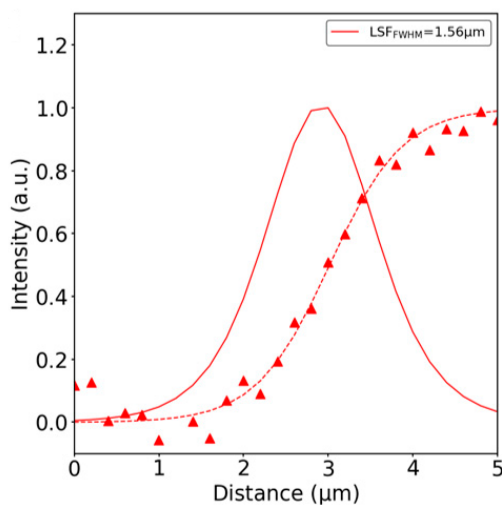


Figure 4.17: ESF and LSF at the region of interest of the 200 nm LED setup, marked in the previous figure by the red section. The red triangular dots are the light intensity measurements at each LED position. The dashed line presents a fitted ESF function, while the solid line is the LSF calculated as the difference between measurements. The inset legend shows the FWHM of the LSF.

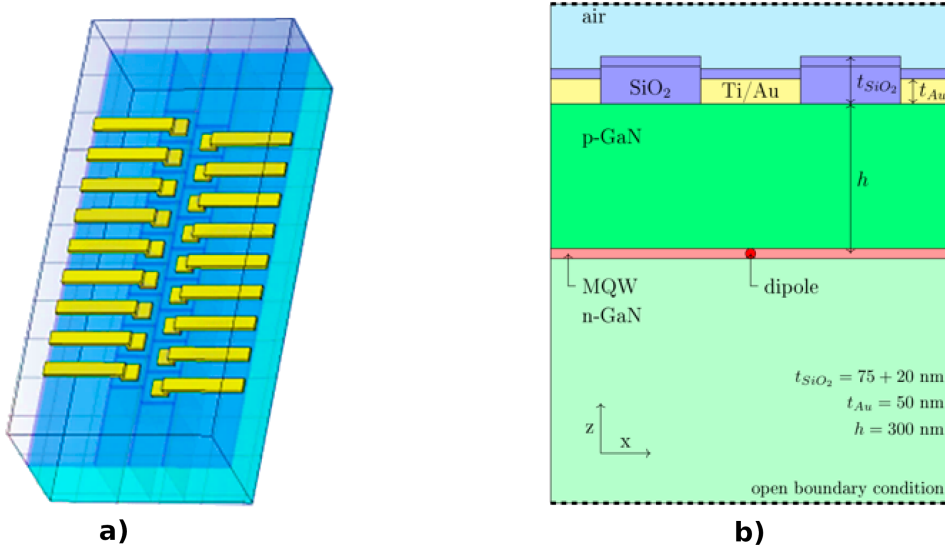


Figure 4.18: Schematic distribution of the 200 nm LED array simulations. In a), general perspective overview, with the metallic contact lines shown in yellow over the GaN. The distribution is detailed in b), which shows the different layers not at scale but with the distances indicated. Simulations used in [8].

To evaluate this limitation, the 200 nm LED chip was modeled [8]. Figure 4.18 a) shows the general scheme of the model, consisting of two lines of 200 nm LEDs with a pitch of 400 nm, just as in the corresponding LED array. Meanwhile, figure 4.18 b) shows a cross-section of the model, showing the materials and their widths. This model was simulated through a finite-difference time-domain algorithm of the CST Studio software by the team of Drs Di Carlo and Auf der Maur in the University of Rome “Tor Vergata”.

Light emission in the multi-quantum well is approximated as dipole sources placed in that layer, 300 nm under the surface of the array and centred under the titanium and gold metallic contact. The wavelength of the light emitted is 450 nm, and the values used for the different physical constants are taken from the literature to match the used in the construction of the LED array. The open boundary conditions at the edges of the simulated area are needed to avoid introducing reflections at the results, which would not appear in the real array.

The optical power emitted by the structure and seen from the top is shown in figure 4.19 a). It can be appreciated how the metallic contact at the top of each LED absorbs and reflects light, creating a minimum in power transmitted. This shapes the light spot, creating a ring-like emission profile around the contact, meaning that light is emitted mainly between contacts. The black lines show the profile of the FWHM emission at the surface interface. The same simulation is shown in a cross-

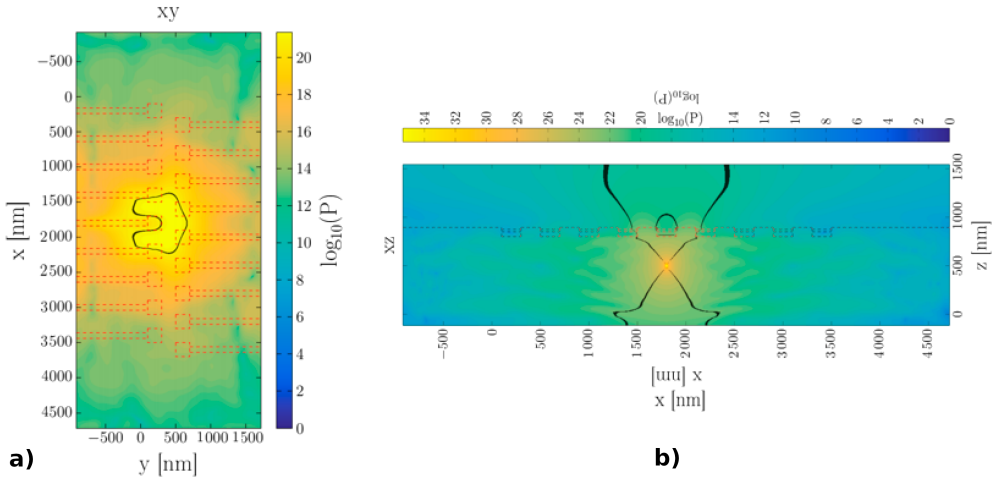


Figure 4.19: Results of the simulation of the 200 nm LED array. a) shows the logarithm of the power distribution on the XY plane 100 nm above the surface of the LED array. Black lines mark the FWHM of the power distribution in both figures. b) shows the logarithm of the power distribution on the XZ plane. From simulations used in [8].

section in figure 4.19 b). The dipole can be appreciated as the high power spot under the surface, shown by dashed lines. The black lines show the FWHM of the power emitted at a given height. These simulations confirm that the light spot is deformed into a less optimal shape than initially thought: since emission takes place as a ring around each LED, the resolving power will be immediately halved even before taking into account any further degradation in contrast due to losing contrast. This is because, for each LED, light is not emitted from the expected position but from the areas around it, which overlap for consecutive LEDs.

It is interesting to simulate how the emitted power distributes when propagating further away from the LED array. Figure 4.20 shows the size of the FWHM of the power emitted by the LED at different heights (z -axis), with the dipole at $z=500$ nm. The LED surface is at the SiO_2 interface, 400 nm above the dipole. As shown, even with a sample placed perfectly flat and in immediate contact with this interface, the light spot is already around 800 nm in size, and so details of smaller size will be lost.

The setup without lenses presented a minimum resolving power of 1500 nm, which could be explained by the EBL shape not being placed immediately at the interface with the LED chip. This happens because the wafer holding the metallic pattern can present irregularities raising it 500 nm from the LED surface. Another aspect to consider is that the actual emission of the LED is worse than simulated due to process variations, which there is no way to control and is a natural consequence of pushing the technological limits and developing an entirely new method of building LED arrays. Process variations caused the failure (complete lack or irregularity of emission) of several of the LED arrays tested.

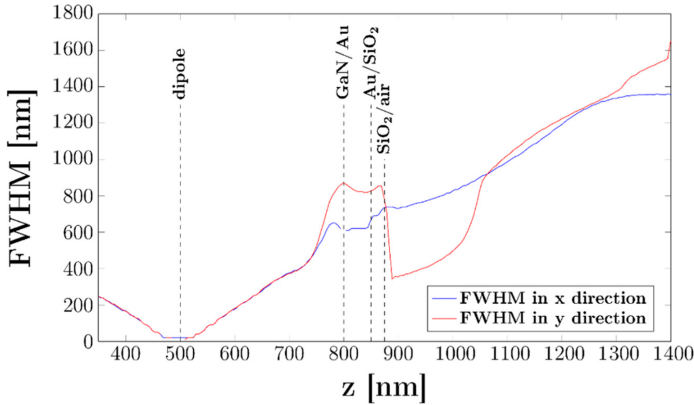


Figure 4.20: Simulation of the FWHM size in nm beyond the LED array surface, as a function of the height (z axis), with the interfaces between materials indicated.

The problems caused by a suboptimal sample placement or faulty LEDs are partially alleviated by using the objective in the downscaling setup. The aperture of the objective naturally selects the axial rays while discarding the ones at the outer side of the light cone, compressing the shape of the image. In addition, the image forms at the focal plane, which can be arbitrarily positioned as necessary. The sample can be placed directly on that plane, as if in direct contact with these virtual LEDs. Since focusing the image involves searching for the plane where the spot is minimum, finding the optimal placement is automatized. This method allows obtaining the best images and confirming where the problems are, but it also excludes the possibility of obtaining super-resolution images since the spot is diffracted through a lens, so Abbe's law will limit its size.

4.4. Discussion of super-resolution capabilities

The aim of the Chipscope project was to investigate NIM as a new approach to super-resolution by producing LEDs with less pitch than the distance specified by Abbe's limit. While current technical limitations of the LED process make it extremely challenging, simulations were carried out to investigate the feasibility of this approach, also shown in reference [7].

Full-field electromagnetic simulations on the range of the hundreds of nanometers were calculated. These simulations, carried out by the Nano and Optoelectronics group at the University of Rome "Tor Vergata" under Prof. Dr Aldo di Carlo, used the Finite Difference Time Domain method (FDTD) implemented in software CST studio. A schematic of the simulated array and sample can be seen in figure 4.21. Al bar periodicities (P_b in figures 4.21 and 4.22) were changed between 100 nm and 300 nm and distances between bars and light spots (D in figures 4.21 and 4.22) from 50 nm to 400 nm. The pitch of the LED array was kept constant at 100 nm, and

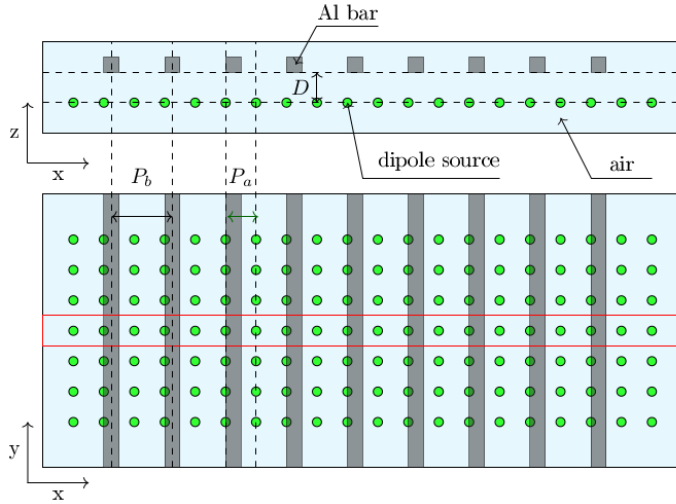


Figure 4.21: Schema of the near field model for electromagnetic simulations. The rectangle limited by red lines indicates the part of the array presented in the simulations. In all cases the LED array period is $P_a = 100$ nm, and P_b is the period of the Al bars.

the width of the Al bars is $W = P_b/2$ at each simulation. As expected, the simulations show a lack of contrast when the Al grating pitch is equal to the LED pitch due to aliasing. Figure 4.22 presents the intensity of the z component of the Poynting vector integrated over the surface above the Al bars and normalized to the corresponding intensity without bars present. The dielectric function for Al was taken from [9].

Simulations also show the distance between LEDs and sample to be essential for the contrast of the received signal, as expected and explained before. In figure 4.22, the simulated far-field intensity from each dipole -simulating a nanoLED as an ensemble of 8 nm dipoles- is drawn over the representation of the aluminium bars. The bars have a periodicity of 210 nm and are properly sampled, as shown by the different responses for polarization perpendicular or parallel to the bar axis. The contrast of the received signal depends on the distance between the light sources and the sample. This is in agreement with the far-field considerations done in the previous chapter. These simulations confirm that NIM could resolve objects below the Abbe limit, achieving super-resolution capabilities at least in theory.

To better approximate realistic sizes for the future LEDs, simulations were also carried out with bigger ensembles of 50 nm dipoles. The simulations in figure 4.23 show how the size of the dipole ensembles (and thus the simulated nanoLEDs) is not a critical influence on the contrast of the NIM setup, with differences only showing up at distances closer than 100 nm. This supports the idea that for NIM microscopes, the performance is mainly affected by the distances and the LED pitch, more than the actual LED sizes. The contrast is defined by equation 4.5.

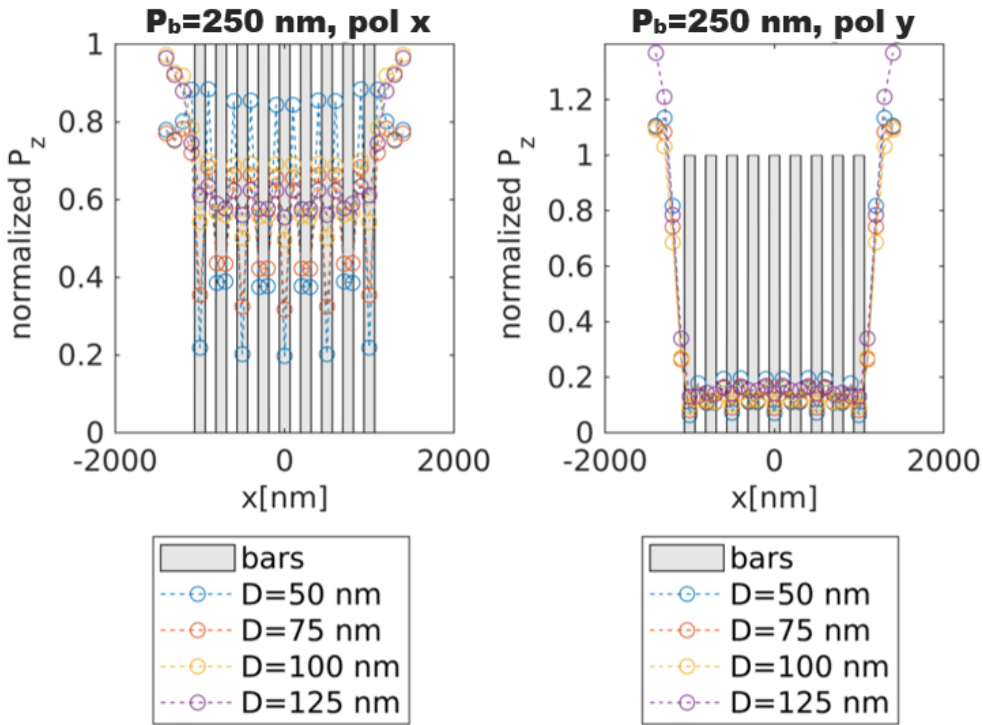


Figure 4.22: Far-field light intensity outgoing from an Al bar grating for a dipole array spaced 100 nm normalized to the intensity of a single dipole source. Different distances between bars and dipoles (D) are simulated using FDTD for a periodicity P_b of the Al bars of 210 nm. The dipole source is polarized in the x direction (perpendicular to the bar axis) in the left image and the y direction (along the bar axis) on the right side. The grey areas indicate the positions of the Al bars.

$$C = 100 \cdot \frac{I_{max} - I_{min}}{I_{max} + I_{min}} \tag{4.5}$$

4.5. Conclusions

In this chapter, we built microscopes seeking the limits of NIM, building on the principles as well as the experience of the initial prototype introduced in the previous chapter.

The challenges found by the Technische Universitat of Braunschweig to develop LEDs small enough to have a pitch below Abbe’s limit for the light they emit moved us to try to simulate them by using lenses to reduce the size of the LED array of the first prototype. This setup helped see critical aspects of the microscope construction and operation, such as stability considerations and location of the light spot and the zone of interest of the sample. Since this last aspect is done by tak-

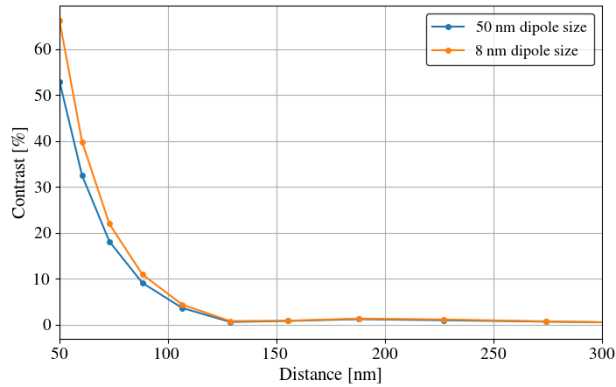


Figure 4.23: Contrast obtained by the different dipole models, ensemble of 8 and 50 nm dipoles forming square patterns to simulate the nanoLEDs. Results obtained from the FDTD simulations.

ing the shadow image of a large part of the sample, the limited pixel count of the SPAD camera made the exploration of the zones of interest more difficult. Thanks to the flexibility on the sensor explained in the previous chapter, the SPAD chip was switched with a CMOS camera, solving the issue.

The light spot downscaling setup obtained the images with the best resolution of the setups presented, with resolutions of 800 nm. This is thanks to the filtering effect of the objective used to reduce the light spot of the LED array, but using lenses, while very useful to understand the setup and detect its critical aspects, is a dead-end: the light spot diffracting through the lens cannot be smaller than Abbe's limit, and so super-resolution cannot be attained.

The intended way of obtaining super-resolution is through LEDs smaller than Abbe's limit. This was finally tested using arrays of 32×2 LEDs of 200 nm emitting at 525 nm. The maximum resolving power obtained in this experiment was 1.56 μm , much worse than expected and than the previous setup. This discrepancy was understood thanks to the EM field simulations of the LED and sample interfaces. We saw that the distance between the point of emission of light within the LED and the sample is a critical parameter.

While the prototypes developed focused on obtaining the best resolutions, other critical aspects of the setup were also detected. For example, the FOV, limited in principle by the size of the LED array, was artificially extended using precise positioning stages. However, this did not add any new complexity to the setup since the positioning stages were already necessary for the components' positioning.

References

- [1] Joseph Goodman. *Introduction to Fourier Optics 4ed.* 4th. 2017.

-
- [2] Syed Naeem Ahmed. *Physics and Engineering of Radiation Detection*. Elsevier, 2015. ISBN: 9780128013632. DOI: 10.1016/C2013-0-15270-1.
- [3] Bong-Soo Lee. “Measurement of Spatial Resolution in Fiber-optic Image Guides”. In: *Journal of the Optical Society of Korea* 5 (2 June 2001), pp. 33–36. ISSN: 1226-4776. DOI: 10.3807/JOSK.2001.5.2.033.
- [4] Qian Chen et al. “Label-free photoacoustic imaging of the cardio-cerebrovascular development in the embryonic zebrafish”. In: *Biomedical Optics Express* 8 (4 2017). ISSN: 2156-7085. DOI: 10.1364/boe.8.002359.
- [5] Joan Canals et al. “A Novel Approach for a Chip-Sized Scanning Optical Microscope”. In: *Micromachines* 12.5 (May 2021), p. 527. ISSN: 2072-666X. DOI: 10.3390/mi12050527.
- [6] Daria D. Bezshlyakh et al. “Directly addressable GaN-based nano-LED arrays: fabrication and electro-optical characterization”. In: *Microsystems and Nano-engineering* 6.1 (2020). ISSN: 20557434. DOI: 10.1038/s41378-020-00198-y.
- [7] K. Kluczyk-Korch et al. “Optical design of InGaN/GaN nanoLED arrays on a chip: toward: highly resolved illumination”. In: *Nanotechnology* 32.10 (Mar. 2021), p. 105203. ISSN: 0957-4484. DOI: 10.1088/1361-6528/abcd60.
- [8] Sergio Moreno et al. “Pursuing the diffraction limit with nano-led scanning transmission optical microscopy”. In: *Sensors* 21.10 (2021). ISSN: 14248220. DOI: 10.3390/s21103305.
- [9] Aleksandar D. Rakić. “Algorithm for the determination of intrinsic optical constants of metal films: application to aluminum”. In: *Applied Optics* (1995). ISSN: 0003-6935. DOI: 10.1364/ao.34.004755.

5

Conclusions and Future outlook of the NIM technique

The work presented so far shows that NIM does operate as a scanning microscopy technique, but as with any new technology, it requires further development in order to reach its full potential. In this chapter, we will discuss the possibilities of this technique.

5.1. Conclusions

Both science and technology are constantly pursuing to bring the smaller detail of the Universe to a plane where humans can study them. One of the tools to do so are microscopes, with which we obtain images from those details. Their appearance went hand in hand with the scientific revolution, which began in the 16th century, and never ceased to evolve.

For a long time, microscopes used visible light, shaping the images through lenses to amplify the microscopic world into the eyes of the one using them. The first optical devices around the year 1600 discovered bacteria, yeast, blood cells, and many tiny animals living in a drop of water. This opened the door to new fields of study on how those lived and interacted.

Ernst Abbe studied the physics behind lens construction and laid out its laws. His contributions showed the limits lens-based microscopes had, and his improvements on the technology to build them made the devices reach them: by the end of the 19th century, optical microscopes were capable of resolving at the limit of the technique, that is, objects with sizes on the order of half the wavelength of the light used to illuminate them.

Lens-based optical microscopes have kept improving since then. However, those improvements were mainly in techniques aimed at solving specific problems, such

as phase contrast or confocal microscopes, and it was not until computers were incorporated in processing the images that they challenged the fundamental limits set by Abbe, for example, with ptychography techniques.

One of these improvements to optical microscopy was lensless microscopy. Lenses tend to be expensive and delicate devices, difficult to fabricate. Compound microscopes are often cumbersome and delicate, keeping them in laboratories. Lensless microscopes removed that element, also using computers to create the images while being cheap and sturdy.

The idea behind the NIM introduced in this work is built upon lensless microscopes, trying to move beyond a fundamental limitation in their design. Where lensless microscopes built the image by using an array of ever so small light sensors in CMOS cameras, NIM tries to do it by using an array of small light sources. This is done to decouple the microscope from the sensor used since sensor pixel sizes cannot be reduced much below the micron, while recent advances in LED fabrication allow doing so.

Nowadays, we see a strong push towards smaller LEDs, driven by incorporating devices into many aspects of our lives. Initially, larger displays with smaller pixel sizes for TVs guided the development of technologies such as LCD and later OLED, and at the moment, GaN LEDs are solid contenders for displays of small pixel size to be used in new applications such as virtual reality. Therefore, arrays of GaN LEDs developed by the Technische Universität Braunschweig have been used to develop the microscopes presented in this work.

As a sampling device, NIM microscopes need a sensor. To keep the microscopes flexible and cover for the possibility that very little light could be emitted from the LEDs, and given the expertise of the VLSI group at UB in which this thesis has been developed, CMOS integrated SPAD sensors were initially chosen as the sensing devices. A 16×16 pixel camera with time-of-flight measurement capabilities was developed and is introduced.

The two previously introduced components need to be held in opposition in the NIM microscope, with the sample sandwiched in between. To do so, another fundamental aspect of the microscope will be the structure and the positioning stages, which control what area of the sample is being studied and its position relative to the other elements.

With these fundamental components, the first microscope was built, and after much testing to understand image formation, the first NIM images were obtained. This informed and helped develop the requirements behind the microscope: to avoid deteriorated contrast, the sample has to be kept as close as possible to the light emission, which in this kind of microscope is where the sampling takes place. However, the sensor requirements are quite relaxed compared to conventional lensless microscopy since NIM only needs to collect the shadow pattern created by the sample as it covers or lets the light pass.

The first prototype used an array of 8×8 LEDs, which was the format of the

images obtained. The LED pitch on that device was $10\ \mu\text{m}$, and in accordance with sampling theory, that meant the resolving power of the microscope built was $20\ \mu\text{m}$.

Building the microscope required the development of an entire platform of boards to support it: a central FPGA board that controlled the LED drivers and the SPAD camera chip, also providing the different power levels. In addition, the System-on-Chip device containing the FPGA also included a microcontroller and allowed to set up and run a Linux system which served as an access interface to the microscope, sending the measurements to a computer and receiving the control instructions from it.

This first prototype showed that the LEDs were emitting enough light to use more mature CMOS cameras. So the next microscopes built switched to those for their much higher pixel count, removing the possibility of fluorescence-based experiments for the moment but gaining the capability to take high-resolution images to help align the stages of the microscope. Meanwhile, the difficulties in developing larger LED arrays of smaller sizes moved us to seek ways to simulate the desired devices.

With the availability of positioning stages with precisions of a dozen nanometers and the possibility of using a small number of LEDs well below the micron size, we tried to simulate larger arrays by scanning with a single light source, moved under the sample to scan it and create the light and shadow patterns of a NIM technique. From this, we explored two paths to develop the technique further and test its capabilities: in one, lenses were introduced to simulate arrays of ideal light sources with very small pitches. The other aspect explored was to use smaller LEDs. Both experiments informed one another and helped realize the limits of the NIM technique.

The objective was used to create a reduced image of the LED array at the image plane of the lens. At the same time, it concentrated the rates by selecting them from the diverging pattern of the LEDs. This means that an almost ideal array of light sources appears on the image plane, where the sample can be placed directly. The images with higher resolution, $800\ \text{nm}$, were obtained with this technique.

Meanwhile, scanning with the actual LEDs without lenses allowed us to find a fundamental limitation of the technique: given the way the LEDs are built, there is always present a layer of material used to support the devices, which in reality limits how close the sample can be from the point of emission of light. Other relevant aspects were the technical difficulties in closing that distance while still moving the LED array to scan without damaging the sample.

In conclusion, we have taken the initial steps in developing a new kind of microscope. The work in this thesis shows that the principle is sound and that microscopes can indeed be built, and we present the first proposals to do so. In the next section, we present some of the possibilities of the technique.

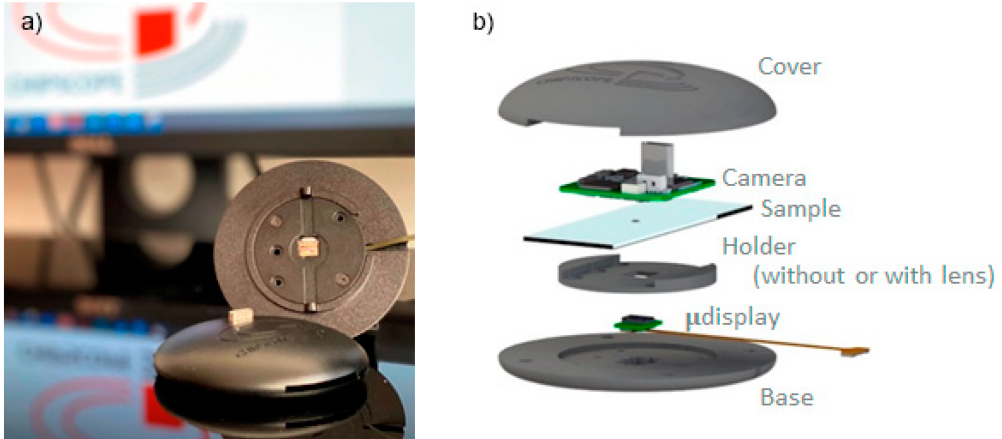


Figure 5.1: Appearance (a) and schematic (b) of the next generation NIM microscope from [7]. The entire structure is only 1.26 cm in height, with a significant contribution from the non-custom camera connector.

5.2. Microscope improvements

An immediate way of increasing the microscope resolving power is to increase the pixel density: reduce the LED size and the pitch with it. This will happen as a natural consequence of current technology trends, which are being driven by the demand for higher density displays for virtual reality or heads up displays [1]. Nowadays, the state of the art reports arrays or the capabilities for building them, with Dots Per Inchs (DPIs) on the range of several thousands [2–6].

Commercial OLED displays with such pixel densities are already commercialized, and two have been used to build further miniaturized versions of the microscopes developed within this thesis [7], as can be seen in figure 5.1. The results agree with the work shown in this thesis, with similar resolutions obtained. The custom LED arrays make obtaining high resolutions without lenses easier but have a much smaller number of pixels (sampling points).

While testing these commercial LED arrays, we found similar limitations to the ones shown in Chapter 4: even if simulating smaller LED pitches, other factors limit the resolving power. The main contribution to that limitation is the separation between LED and sample, which in the ideal case should be 0, or kept vanishingly small compared with the distance between sample and sensor. In addition, the interface between mediums in the GaN chip and air in that space also degrades resolving power, limiting it below what could be possible theoretically.

This reinforces the argument that while the research on miniaturization of LED arrays will help, building NIM microscopes with resolving powers well below the micron will require a custom LED fabrication process, with special care placed in reducing the separation from the point of emission of light in the LED and the sam-

ple or make the emission of light more focused by micro-engineering the material at the interface.

Perfecting the LED fabrication process is the main requirement to integrating NIM microscopes in highly compact and lightweight systems. Plenty of the required electronics have already been integrated during this thesis: cameras and the LED driving circuits. The next stage for further integration is to replicate what is already offered in commercial OLED displays like the one shown in [7], which would mean including the control and communication interfaces into a single board or even chip. Hence, the possibility of building small microscopes devices with minimal moving parts is open and feasible.

Beyond the engineering improvements, another way of obtaining improvements in the resolving power remains open in exploring the techniques applied in conventional lensless imaging to obtain sub-pixel resolution. The image acquisition done so far has been direct, with the only processing being compensation for brightness calibration. However, there is plenty of potential in applying more complex data processing and on different setups aimed at applying sub-pixel techniques.

5.2.1. Applications

A high-resolution microscope with minimal optical components that can be carried in the same package as the laptop that might be used to control presents immediate advantages, for example, allowing specialists tending to illness outbreaks in remote regions to conduct initial assessments or for ecological related studies. At the same time, the high large scale production of such devices can make them accessible to low-income communities.

A miniaturized NIM-based microscope could enable large-scale parallel image acquisition for other applications. This could have applications in distributed sampling, for example, receiving data from several microscopes within a large liquid medium, or maybe working in tandem within more complex devices such as a microorganism incubator, sampling the culture medium to monitor its status. In vivo microscopy with other miniature, chip-based microscopes has already been demonstrated, and NIM would add its high-resolution to such experiments.

The high resolution and low weight could make these microscopes especially useful in space-related applications, where mass is a critical aspect to account for. For example, NIM microscopes could be used in probes sent to study asteroids or maybe even other planets and moons in the solar system.

It is worth noting that the samples that such microscopes could study require specific characteristics in order to be adequately scanned. As with any scanning optical microscope, it would be challenging to study irregular materials not laying flat, in this case, over the LEDs. Non-transparent materials or thick samples could also pose a problem. The approach that could work best with minimal sample preparation would be to study particles suspended in a liquid, circulated through the microscope in a microfluidic circuit. While initially we intended to include microfluidics

into the microscope, and indeed a prototype was prepared for it, the difficulties faced did not allow for any significant experimentation with it. Nevertheless, it is something added to the ideas to keep expanding the NIM technique.

References

- [1] Tao Zhan et al. “Augmented Reality and Virtual Reality Displays: Perspectives and Challenges”. In: *iScience* 23.8 (Aug. 2020), p. 101397. ISSN: 25890042. DOI: 10.1016/j.isci.2020.101397.
- [2] Fang Ou et al. “P-125: Monochromatic Active Matrix Micro-LED Micro-displays with >5,000 dpi Pixel Density Fabricated using Monolithic Hybrid Integration Process”. In: *SID Symposium Digest of Technical Papers* 49.1 (May 2018), pp. 1677–1680. ISSN: 0097966X. DOI: 10.1002/sdtp.12309.
- [3] Yoann Seauve et al. “Exploring 3D Pixel Circuits for Small Pitch and High Brightness GaN Microdisplays”. In: *2019 15th Conference on Ph.D Research in Microelectronics and Electronics (PRIME)*. IEEE, July 2019, pp. 209–212. ISBN: 978-1-7281-3549-6. DOI: 10.1109/PRIME.2019.8787842.
- [4] Hidenori Kawanishi et al. “High-Resolution (1,000 to over 3,000 ppi) Full-Color “Silicon Display” for Augmented and Mixed Reality”. In: *Proceedings of the International Display Workshops 2* (Nov. 2019), p. 641. ISSN: 1883-2490. DOI: 10.36463/IDW.2019.FMC4_LCT4-1.
- [5] Steffen Bornemann et al. “Processing and Characterization of Monolithic Passive-Matrix GaN-Based MicroLED Arrays With Pixel Sizes From 5 to 50 μm ”. In: *IEEE Photonics Journal* 13.5 (Oct. 2021), pp. 1–9. ISSN: 1943-0655. DOI: 10.1109/JPHOT.2021.3106584.
- [6] Yongzhou Zhao et al. “2000 PPI silicon-based AlGaInP red micro-LED arrays fabricated via wafer bonding and epilayer lift-off”. In: *Optics Express* 29.13 (June 2021), p. 20217. ISSN: 1094-4087. DOI: 10.1364/OE.428482.
- [7] Anna Vilà et al. “A Compact Raster Lensless Microscope Based on a Microdisplay”. In: *Sensors* 21.17 (Sept. 2021), p. 5941. ISSN: 1424-8220. DOI: 10.3390/s21175941.

A

Resum

A.1. Introducció a la Microscopia

L'aparició de l'ull durant el període Cambrià va ser tant important que avui dia el 95% dels animals multicel·lulars en tenen, i és el sentit que els humans utilitzem de forma principal per percebre el món que ens envolta. L'ull humà va evolucionar per capturar i enfocar llum en el rang visible en la retina, però és un mecanisme no exempt de limitacions: objectes massa llunyans o massa petits no es poden distingir, cosa que aviat va motivar el desenvolupament de tecnologies que intenten corregir aquests problemes, així com l'estudi de la naturalesa i comportament de la llum en sí mateixa.

A l'antiga Grècia, Euclides ja va teoritzar que la llum viatjava en línia recta en un medi homogeni i va formular correctament la llei de la reflexió, i Claudi Ptolomeu va proposar als voltants de l'any 170 una aproximació per la llei de la refracció que tardaria 1500 anys a ser millorada.

Després de la caiguda de l'Imperi Romà els científics del món musulmà estudiaven la naturalesa de la llum millorant les teories prèvies, però no fou fins a finals del segle XIII que tenim constància de la fabricació de les primeres lents, fetes per corregir problemes de vista. Tot i això, no tenim constància de que els científics de l'època els prestessin molta atenció i les estudiessin.

Fou Galileo Galilei, a principis del s. XVII, qui va millorar dissenys previs tant de telescopis com de microscopis en adonar-se de la rellevància que aquests instruments tindrien en el progrés científic. La revolució científica que va seguir a partir del Renaixement va permetre el desenvolupament tant dels instruments com del coneixement teòric sobre la llum de forma interrelacionada. Podem considerar que fou Abbe el s. XIX qui va perfeccionar de forma definitiva els microscopis òptics basats en lents i en va descriure el funcionament i límits a nivell fonamental amb la llei del *límit de difracció d'Abbe*, que diu que és impossible distingir mitjançant un

microscopi òptic objectes més petits que aproximadament la meitat de la longitud d'ona de la llum que els il·lumina.

Aquest contratemps però no va frenar la curiositat ni l'impuls de millora de les tècniques. Avenços en altres camps tals com la mecànica quàntica van obrir noves oportunitats, com l'aparició dels microscopis electrònics, i més recentment els diversos mètodes de super-resolució que permeten sobrepassar les limitacions dels microscopis òptics basats en lents pel que fa a la resolució.

La microscopia òptica de super-resolució va ser un avenç tant revolucionari que va ser premiat amb el Premi Nobel de Química l'any 2014 al possibilitar la observació de l'estructura interna de les cèl·lules en viu en contraposició a les tècniques ja existents que ofereixen resolucions similars o millors però al preu d'immobilitzar i fixar la mostra de forma letal.

El límit d'Abbe suposa que la llum és adquirida mitjançant un objectiu on la llum es difracta. En canvi, les tècniques de super-resolució empenen aproximacions diferents: STED i SIM fan servir patrons d'il·luminació i efectes òptics no lineals com la saturació en l'emissió de fluorescència per modular la funció de dispersió de punt. Altres tècniques s'allunyen de l'estructura de la microscopia tradicional per millorar-ne els resultats, com les tècniques 4Pi o bé I^5M que adquireixen llum des d'ambdós costats de la mostra. Finalment, un conjunt de tècniques estan basades en la localització de molècules fluoròfores individuals, tals com STORM, PALM o FPALM. La taula A.1 compara breument les diferents tècniques de microscòpia de super-resolució.

No obstant la revolució que suposen les tècniques de super-resolució, segueixen sent muntatges complexos i costosos que requereixen personal especialitzat en laboratoris dissenyats específicament. En contrapartida a aquestes tècniques, la miniaturització dels components electrònics així com l'increment de la seva capacitat de procés va permetre el desenvolupament de microscopis sense lents, molt atractius perquè permeten construir microscopis senzills, barats, en miniatura i que mantenen unes bones capacitats òptiques. La figura A.1 mostra un esquema simplificat d'un microscopi sense lents: en ell, la mostra es posiciona molt a prop d'una càmera, i s'il·lumina amb una font de llum prou allunyada com perquè la il·luminació sigui coherent. La resolució d'aquest muntatge ve donada per la mida i separació dels píxels de la càmera: cadascun registra l'ombra generada per la mostra just damunt seu.

El desenvolupament d'aquestes tècniques va motivar als membres que han acabat component el projecte Europeu Chipscope a explorar si podíem aproximar-nos a la super-resolució en muntatges sense lents, construint un microscopi compacte i de baix cost com a alternativa als mètodes existents. Això s'ha materialitzat al llarg del projecte europeu i en la feina presentada en aquesta tesi, en la que desenvolupem un nou tipus de microscopia.

Anomenem el mètode desenvolupat en aquestes pàgines Microscopia de Nano Il·luminació (MNI), perquè es basa en il·luminar la mostra mitjançant fonts de llum

Tècniques	STED	SIM	PALM / STORM / FPALM
Resolució Lateral	40 nm	100-130 nm	20-50 nm
Resolució Axial*	500 / 20-100 nm	250 / 100 nm	100 / 20 nm
Detecció	Escaneig	Camp ampli	Camp ampli
Ventall de fluoròfor disponible	Limitat (compatibles amb STED)	Ampli	Limitat, han de ser compatibles amb STORM
Veolcitat de formació d'imatge	Segons	Mil·lisegons to segons	Segons
Requereix processat de les dades adquirides?	No	Si	Si
Complexitat del muntatge	Alta	Mitja a alta	Baixa a Mitja
3D	Si, isoSTED	Si, 3D SIM, I5S	Si, 3D STORM, iPALM

Taula A.1: Comparació de tècniques de super-resolució. *La resolució axial es mostra tant en la quantitat normal com en l'obtinguda mitjançant la tècnica 3D, separat per /

de mida nanomètrica de forma ordenada, tal com es mostra en la figura A.2. En ella, una hipotètica mostra biològica es posiciona sobre una matriu de nano-LEDs de Nitrur de Gal·li (GaN). En un muntatge com el proposat, la resolució del microscopi depèn dels nano-LEDs i la seva distribució en comptes del dispositiu de sensat utilitzat en el cas del mètode de microscopia sense lents esmentat prèviament.

Al dependre de la distribució i mida dels LEDs en la matriu, aquest mètode obre la porta a obtenir imatges de super-resolució si els LEDs es miniaturitzen fins a tenir una mida inferior a la del límit d'Abbe. En el cas de LEDs de llum blava ($\lambda \approx 400$ nm), això implica una mida d'uns 200 nm. Si bé ja hi ha LEDs individuals d'aquesta mida en laboratori, la MNI requereix que n'hi hagi un nombre el més elevat possible controlats externament com a matriu de LED, cosa que no s'ha aconseguit mai abans d'aquest projecte.

El projecte europeu ChipScope és un esforç conjunt d'un consorci multidisciplinar que consisteix en:

- Technische Universität Braunschweig (TUBS), encarregats de desenvolupar les matrius de nano-díodes emissors de llum (nanoLEDs) pel microscopi.

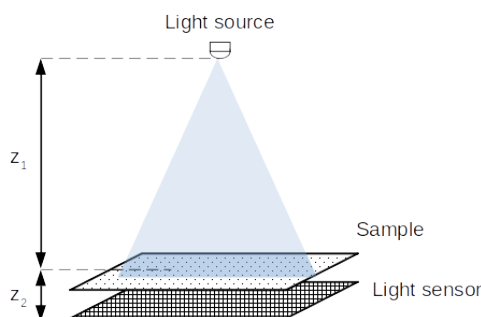


Figura A.1: Esquema d'un muntatge de microscopia hologràfica sense lents

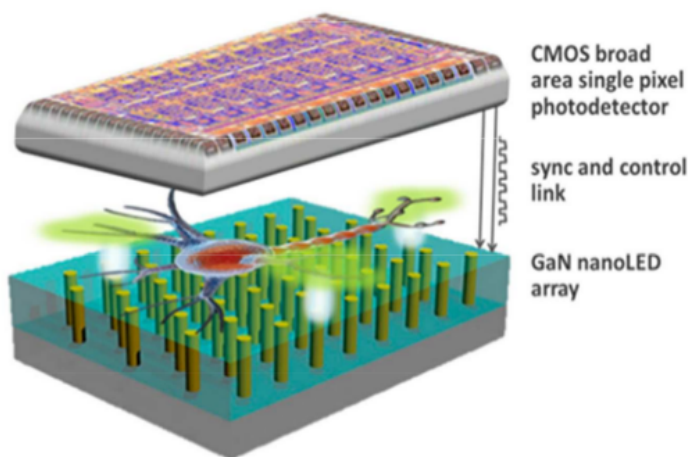


Figura A.2: Esquemàtic de l'estructura bàsica d'un MNI

- Univerity Tor Vergata Roma, que proporcionen les simulacions de camps electromagnètics i de la operativa dels LEDs.
- Austrian Institute of Technology, que fabriquen sistemes fluïdics d'alta precisió per posicionar les mostres en el microscopi.
- Ludwig-Maximilians-Universität München que s'encarrega de la calibració i caracterització de les capacitats del microscopi.
- Medical University of Vienna que ha estudiat possibles aplicacions pel microscopi en ciències mèdiques, i proporcionat mostres de teixit per a validar-lo.
- Swiss Foundation for Research in Microtechnology ha tingut al seu càrrec la difusió del projecte tant en cercles acadèmics com d'interès general.

- Universitat de Barcelona, responsables d'estudiar i desenvolupar els sensors, integrar els components en prototips funcionals del microscopi i coordinar el Projecte Europeu.

A.2. Components del Microscopi de Nano Il·luminació

Per obtenir una imatge amb un MNI s'escaneja la mostra il·luminant successivament amb els nano-LEDs que componen la matriu, mesurant la quantitat de llum de cadascun que arriba al sensor, que es troba situat en oposició a l'altre banda de la mostra. Això permet detectar la presència d'un objecte sobre els LEDs i altra informació com la transparència.

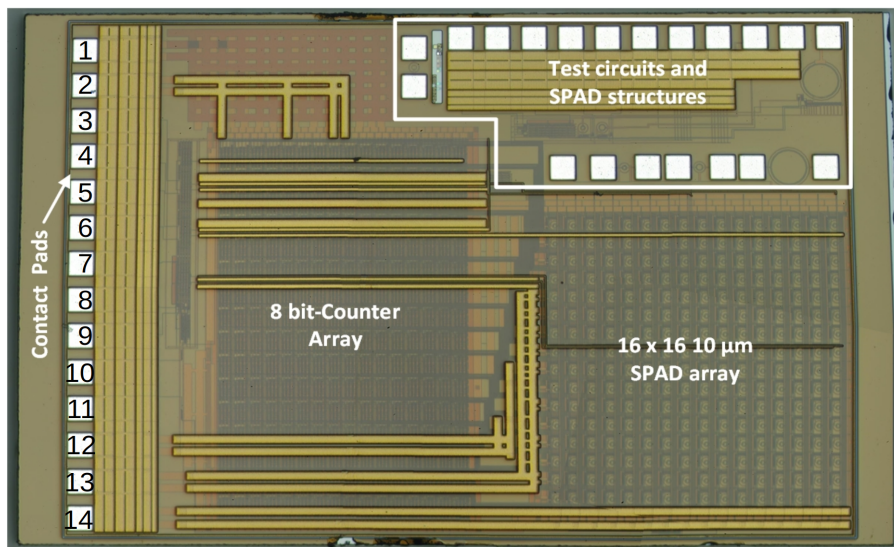
Així, els components centrals d'un microscopi de nano il·luminació són la matriu de nanoLEDs i l'electrònica requerida per escollir el LED a encendre i alimentar-lo; el sensor utilitzat per captar la llum emesa i no interceptada per la mostra; i la pròpia estructura del microscopi, amb posicionadors per poder explorar la mostra a voluntat.

En el si d'aquesta tesi s'ha desenvolupat una càmera SPAD (Single Photon Avalanche Diode, díodes d'allau activada per un sol fotó) com a dispositiu sensor per a mesurar la llum emesa. Els SPADs són dispositius flexibles que podrien fins i tot en un futur usar-se per mesures de fluorescència, i que es van triar perquè en ser sensibles gairebé a fotons individuals, assegurem que fins i tot si l'emissió de llum per part dels nanoLEDs desenvolupats és massa petita, la podem detectar igualment.

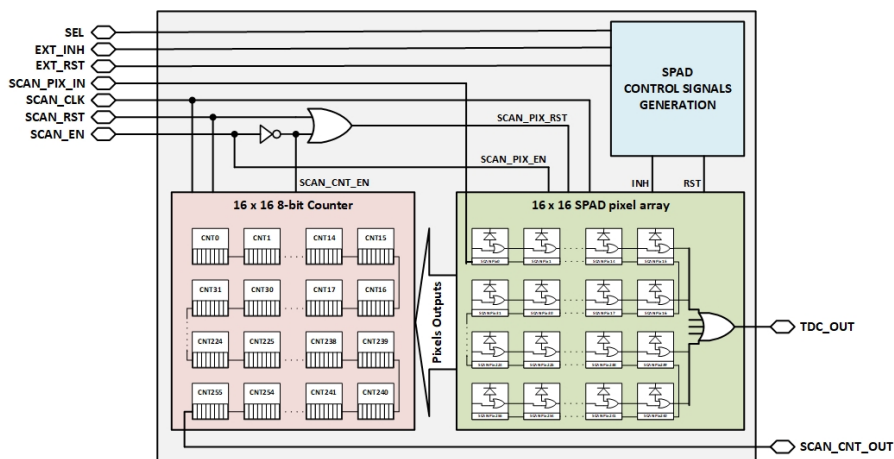
La càmera SPADs s'ha dissenyat en un procés CMOS d'alt voltatge, en el node tecnològic de 350 nm. Els sensors tenen 200 Hz de soroll en condicions de foscor i una eficiència de detecció de fotons del 30%, que s'adiu a la bibliografia per altres dispositius en el mateix node tecnològic. Els SPADs s'han agrupat en una matriu de 16×16 píxels, amb la intenció de facilitar la operació del microscopi en comparació a fer-la amb un sol píxel: una matriu ens permet utilitzar el sensor amb millors característiques del conjunt, així com capturar imatges de baixa resolució però que permeten recórrer i explorar la mostra per alinear-la amb més facilitat abans de passar a operar en mode MNI. Cal recordar que en MNI només s'utilitza un sol sensor, ja que són els LEDs els que es van alternant per il·luminar la mostra.

La figura A.3 mostra una fotografia i l'esquemàtic de l'estructura de la càmera. Els píxels SPAD són circulars i de $10 \mu\text{m}$ de diàmetre, amb un pitch de $70 \mu\text{m}$. La sortida de cada píxel connecta amb un contador de 8 bits que augmenta el nombre cada cop que l'SPAD detecta un fotó, comptant així el nombre de fotons rebuts. Com es pot veure en la figura A.3 a), les connexions al xip es troben totes distribuïdes a l'esquerra, amb la matriu de detectors a la dreta. Això s'ha fet així per facilitar la integració del xip en sensors: permet introduir només l'extrem del microxip a l'interior del microscopi per fer les mesures.

La càmera té 4 modes d'operació, controlats des d'una FPGA Zedboard en aquest cas, on a més s'hi ha implementat un conversor de Temps a Digital que cronometra



(a)



(b)

Figura A.3: a) Fotografia del xip de la càmera d'SPADs fabricada, amb les parts indicades. El quadre blanc tanca SPADs i circuits de test. b) Esquemàtic general de l'arquitectura de la càmera, mostrant com els mòduls principals es connecten entre ells així com la lògica de les senyals de control. Cada circuit SPAD (a la part dreta de la imatge, en verd) connecta amb el contador corresponent (esquerra, en vermell).

l'arribada de fotons a la matriu mitjançant la sortida dedicada. Els modes d'operació són:

- Configuració: es carrega la configuració a la càmera (píxels actius).
- Operació TDC: en aquest mode s'ignoren els comptadors de la càmera. Normalment, només un sol SPAD està actiu en tota la matriu, ja que es realitza una operació OR amb les sortides de tots els sensors per dirigir-los cap a l'FPGA per poder cronometrar de forma directa la detecció dels fotons.
- Operació de càmera: en aquest mode els comptadors a la sortida dels píxels SPAD estan actius i s'incrementen cada cop que es detecta l'arribada d'un fotó.
- Lectura: mode d'operació que s'activa un cop s'han acabat les mesures per tal de llegir el nombre de deteccions guardat a cada comptador. Les dades es treuen bit a bit en sèrie, requerint 2048 cicles de rellotge per treure cap a l'FPGA les dades dels 256 comptadors de 8 bits.

Els LEDs per al microscopi no s'han desenvolupat a la UB, si no al Technische Universität Braunschweig (TUBS), per part de l'equip amb expertesa en la fabricació de dispositius de GaN. La UB s'ha encarregat de desenvolupar l'electrònica de control per fer funcionar les diferents matrius desenvolupades.

L'evolució de les matrius de LEDs es mostra en la figura A.4. Les primeres matrius de LEDs emprades en el treball no es mostren. Consistien en estructures de 75 μm que es van emprar per provar el muntatge del primer prototip, però la primera matriu de LEDs de GaN utilitzada en el microscopi tenia un format de 8×8 dispositius quadrats, amb una mida de 5 μm . Aquesta primera versió ens va permetre explorar el concepte del microscopi, obtenir les primeres imatges i informar tant del funcionament com de les limitacions que podia presentar. La més urgent, que el tipus d'interconnexionat fet servir per seleccionar quin LED s'hauria de canviar per treballar amb matrius més grans.

L'experiència amb la primera matriu de LEDs va informar els dispositius que vindrien a continuació. Per un costat es va fabricar una nova matriu lineal de LEDs el més petits possibles, amb la intenció d'explorar els límits tecnològics tant de la fabricació de matrius de LEDs com del propi microscopi. Això es va fer a canvi d'un pitjor factor de forma, ja que aquesta matriu consistia en 2 fileres de 32 LEDs, cadascun de només 200 nm. Aquest conjunt de LEDs va mostrar les dificultats de fabricar dispositius d'aquesta mida, especialment les interconnexions.

Per altra banda, es va desenvolupar una matriu de LEDs amb la intenció de validar un altre tipus d'interconnexió, l'adreçament per matriu (en oposició a l'adreçament directe que havien fet servir les anteriors). Aquesta matriu té un factor de forma de 6×6 , i els LEDs són també majors: la intenció amb ella era que l'equip

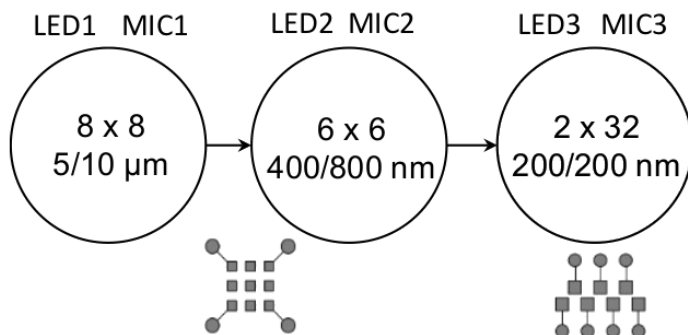


Figura A.4: Evolució dels LEDs fabricats i utilitzats en el projecte ChipScope (i aquesta tesi) per a integrar en els microscopis. Cada pas mostra el factor de forma de la matriu de LEDs així com les dimensions de cada píxel i el pitch entre ells.

de TUBS validés la tecnologia de fabricació de les interconnexions de cara a en un futur escalar-la a matrius amb major nombre de LEDs de menor mida.

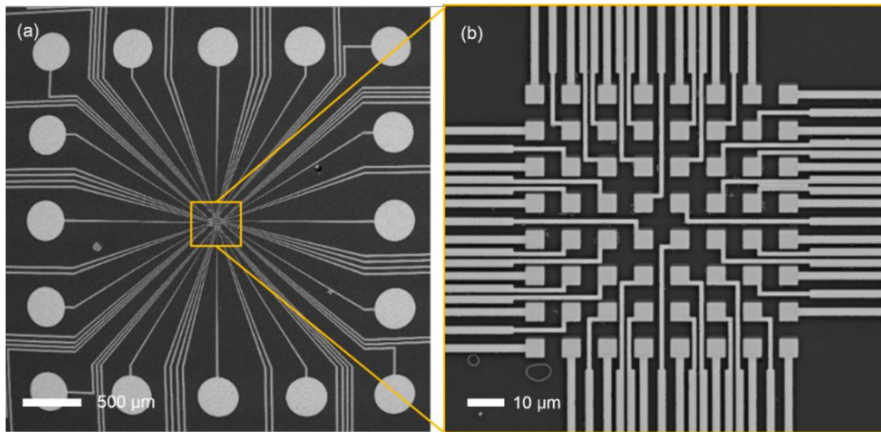
Algunes de les matrius de LEDs implementades es poden veure en les fotografies de la figura A.5.

A.3. Microscopia de Nano Il·luminació

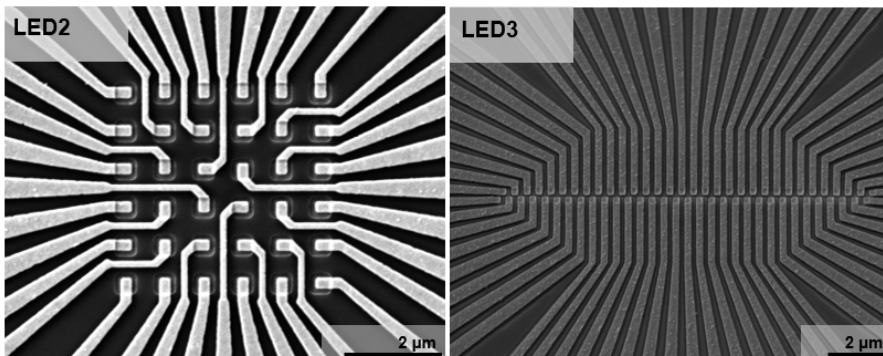
La MNI és una tècnica d'escaneig en el que el mostreig es fa de forma discreta, encenent i apagant consecutivament cadascun dels LEDs de la matriu per mesurar la llum que n'arriba al detector a través de la mostra. Un exemple d'aquest procés es mostra en la figura A.6, en el que es veu el procés d'adquisició d'una imatge MNI, per una sola fila de la matriu de LEDs. El procés es repeteix per cada fila de la matriu de LEDs, creant un mapa de la mostra segons la llum que n'arriba al sensor.

El camp de visió d'un microscopi de MNI és bàsicament la mida de la matriu de LEDs emprada per il·luminar la mostra. El poder de resolució depèn de la distància entre els LEDs: la seva distribució és l'equivalent al període de mostreig de la teoria de Nyquist, però un requisit fort perquè el microscopi funcioni correctament és que la mostra es trobi molt més a prop (idealment en contacte directe) del punt d'emissió de la llum que del sensor, ja que el contrari en redueix el contrast. Això es produeix perquè el con de llum del LED s'amplia a mesura que la mostra s'allunya, il·luminant-ne una àrea major que es projecta cap al detector, que integra la informació de tota l'àrea il·luminada.

Els microscopis MNI estan construïts seguint l'estructura general mostrada de forma esquemàtica en la figura A.7. En haver de posicionar la mostra tan propera com fos possible a la matriu de LEDs, el muntatge ja suggeria fer-se amb aquesta a la part inferior, ja que la gravetat juga a favor d'això. Tots els microscopis desen-



(a)



(b)

Figura A.5: a) A l'esquerra, microfotografia de la matriu de LEDs pel primer prototip: 64 píxels de 5 μm organitzats en 8 files i 8 columnes. La fotografia és un detall del xip que es mostra a l'esquerra, amb els contactes. b) Imatges SEM imatges de les matrius de (a) 6 × 6 LEDs de 400 nm i (b) la matriu de 2 × 32 LEDs de 200 nm.

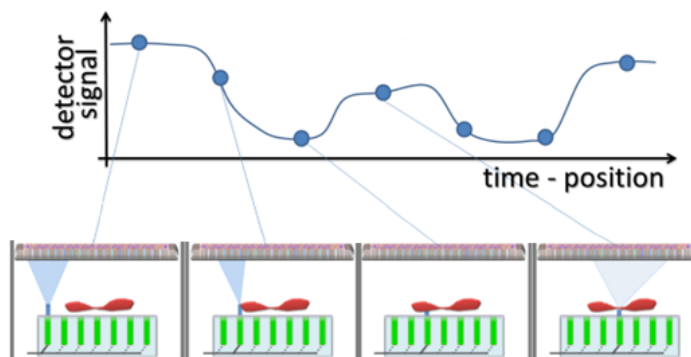


Figura A.6: Principi d'operació del microscopi: la mostra és escanejada il·luminant alternativament diferents LEDs, i el sensor recull la intensitat que n'arriba.

volupats incorporen també dispositius de posicionament per moure la mostra dins del camp de visió del microscopi i explorar-la.

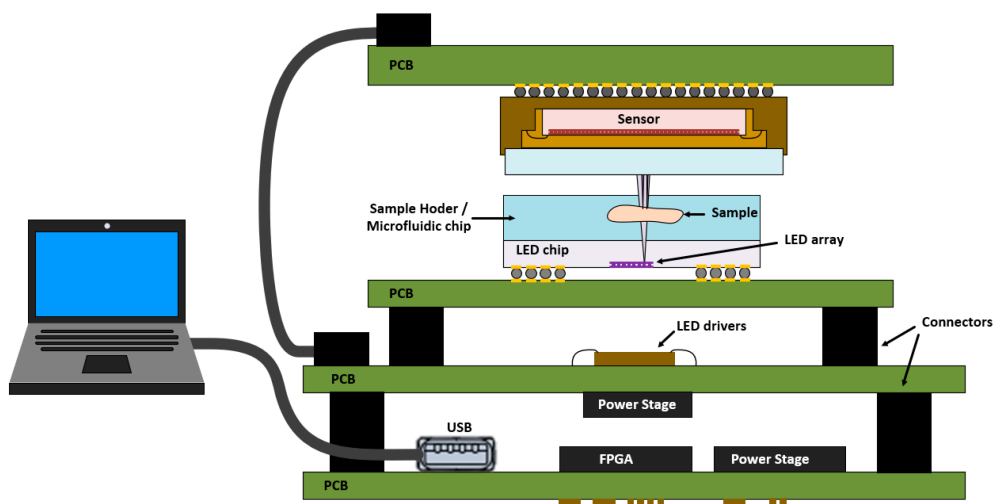


Figura A.7: Esquema general del muntatge dels components del microscopi. La matriu de LEDs es solda amb bola sobre la pila de PCB d'alimentació i control. La mostra es posiciona a sobre els LEDs, a la distància mínima possible. El sensor hi està en oposició, a la part superior.

Una FPGA basada en el SoC de Xilinx Zynq®-7020 s'encarrega de rebre les instruccions des d'un ordinador i controlar el microscopi. Vam escollir aquest dispositiu perquè inclou un processador ARM dual-core Cortex-A9 amb perifèrics directament connectat a nivell integrat amb una FPGA totalment configurable. Això proporciona gran flexibilitat al dispositiu, fins al punt que alguns dels prototips executen un sistema operatiu Linux de forma integrada. Addicionalment, la FPGA inclou un convertidor de temps a digital (TDC en anglès).

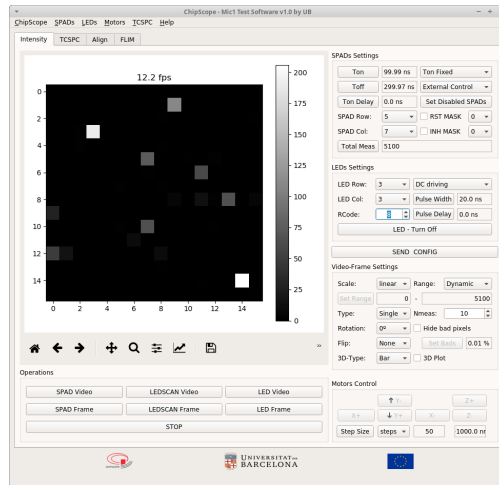


Figura A.8: Interfície gràfica d'usuari desenvolupada per a controlar els diferents microscopis.

El software de control dels microscopis a alt nivell s'ha desenvolupat amb Python3, amb una interfície gràfica pensada per facilitar-ne l'ús que es pot veure a la figura A.8. La part principal de la finestra (a l'esquerra) mostra la llum rebuda per cada píxel de la matriu de 16×16 sensors, amb la barra de color indicant el nombre d'intensitat. Sobre aquesta imatge es mostren els frames per segon que s'estan obtenint, i al marge inferior i esquerra hi ha les opcions de configuració i control de mesura.

Pel que fa al muntatge del primer prototip, es van fer diverses iteracions fins a arribar al que seria el primer prototip de microscopi pròpiament. Aquest microscopi utilitza la matriu de 8×8 $5 \mu\text{m}$ LEDs, els drivers corresponents, la càmera d'SPADs, un suport per la mostra dissenyat i imprès amb impressora 3D, l'electrònica de control i etapes de posicionament manual. Tot això està contingut en una caixa de $12 \times 21 \times 31 \text{ cm}^3$, dimensions condicionades bàsicament per la placa de la FPGA Zed-board i les etapes de posicionament, com es pot veure en la figura A.9. En la figura no es mostra la caixa de cobertura que tanca tot el muntatge i el converteix en una caixa fosca per tal d'eliminar interferències de la llum externa. En el muntatge, la mostra es col·loca en el suport que es recolza sobre el xip de LEDs i es pot moure en els 3 eixos de llibertat. Les peces es van fabricar en alumini tallat segons els patrons fets per nosaltres.

Per a la validació del microscopi es va dissenyar un conjunt de patrons amb figures de fins a $20 \mu\text{m}$, impreses en alumini mitjançant litografia per feix d'electrons. La taula A.2 mostra les imatges obtingudes de diferents patrons, comparant entre l'adquisició amb un microscopi òptic convencional (a l'esquerra, amb la zona d'interès ressaltada en vermell); i la imatge MNI obtinguda mesurant la llum en un sol sensor SPAD amb el muntatge anterior.

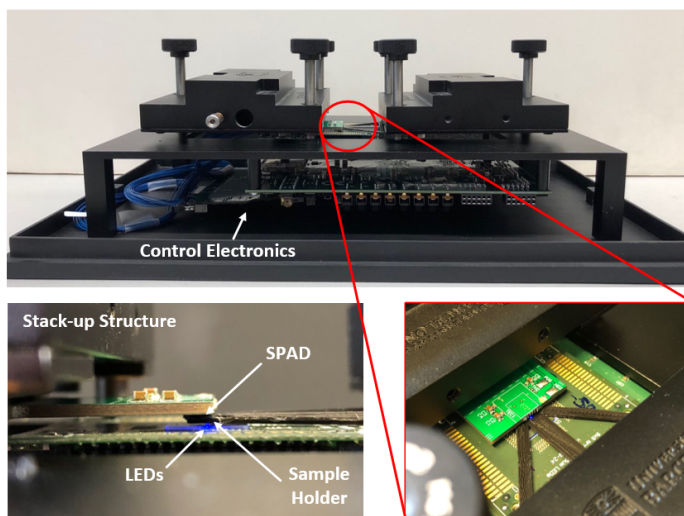


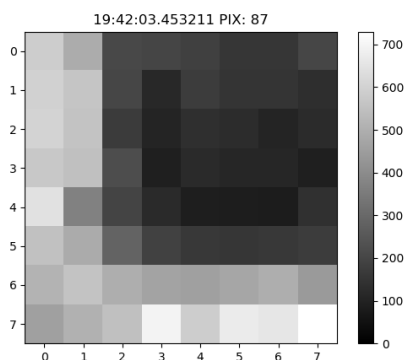
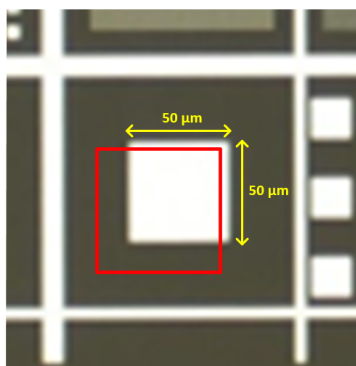
Figura A.9: Fotografia del primer microscopi de nano il·luminació, amb detall de l'estructura on hi ha el microscopi en si: on es superposen el xip del detector i de LEDs.

Com que la MNI és un mètode de transmissió, les parts metàl·liques bloquegen la llum i apareixen fosques en la imatge, al contrari que en l'òptic que reflecteix la llum. Com es pot veure, el nombre de píxels de les imatges es correspon al de la matriu de LEDs: 8×8 .

Taula A.2: Comparativa entre les mateixes regions de la mostra observades amb un microscopi òptic (esquerra) i el microscopi de Nano Il·luminació (dreta), amb les mides de les àrees d'interès indicades.

Imatge microscòpia òptica

Imatge MNI

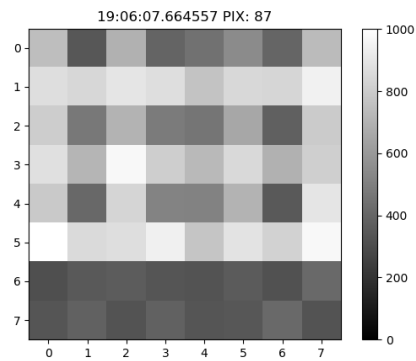
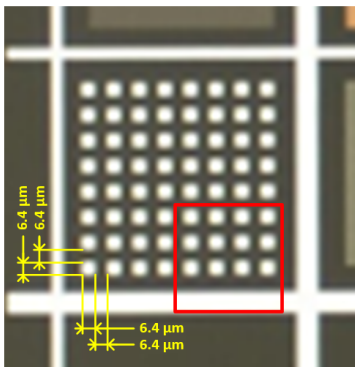
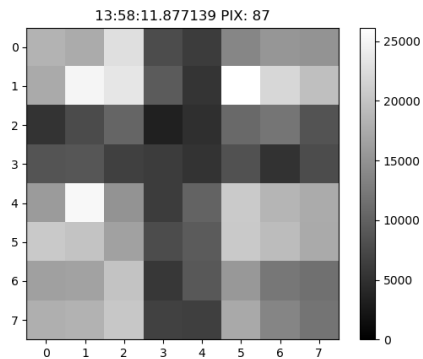
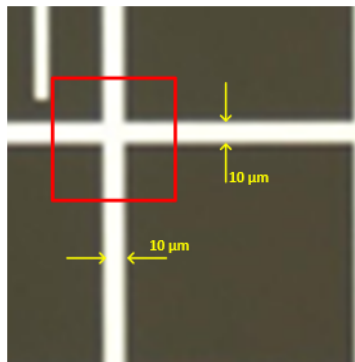
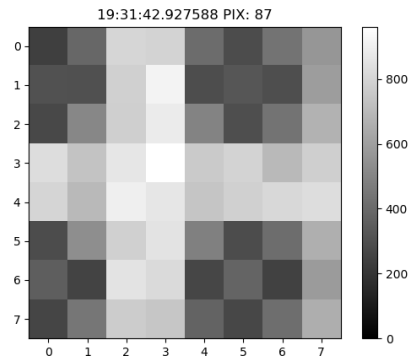
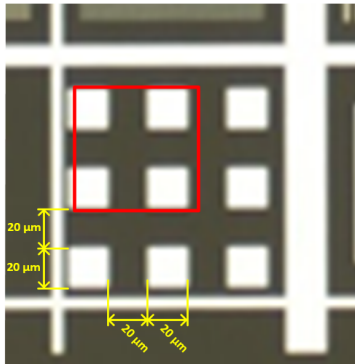


Continua a la següent pàgina

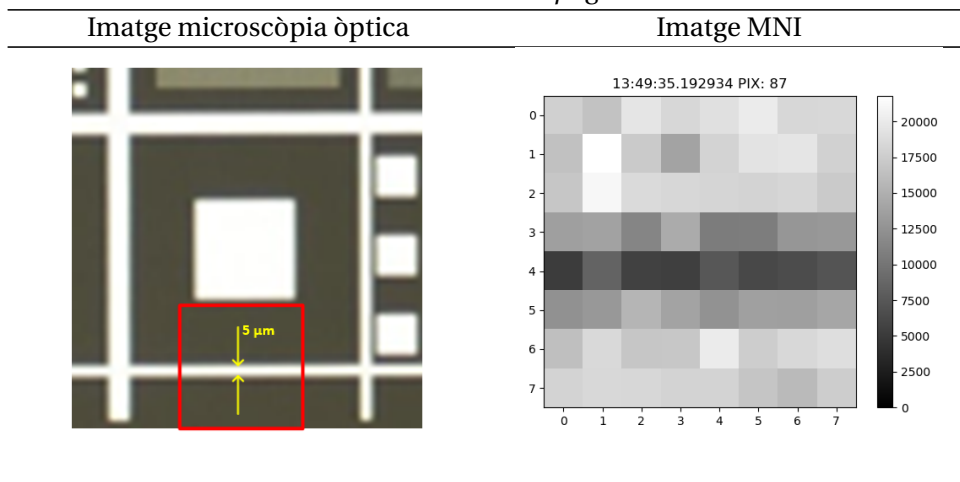
Taula A.2 – *Continua de la pàgina anterior*

Imatge microscòpia òptica

Imatge MNI



Continua a la següent pàgina

Taula A.2 – *Continua de la pàgina anterior*

El primer prototip ens va permetre veure com un factor clau per a la correcta operació del microscopi no seria fàcil de controlar en aplicacions reals: el de la distància entre mostra i LEDs. En els dispositius reals, el substrat protector de safir o el mateix gruix dels components força una petita distància que no es pot evitar. Serà vital, en un futur, buscar la manera de reduir aquesta distància per tal de millorar les capacitats del microscopi.

A.4. Perseguint els límits de la MNI amb matrius de LEDs

Un cop establert el mecanisme de funcionament bàsic de la nova tècnica de microscòpia i validat amb el primer prototip, passem la atenció als límits que presenta la tècnica.

En primer lloc va ser necessari un procés d'adaptació: l'equip de Braunschweig a càrrec de fabricar els dispositius LED va tenir molts problemes en fabricar matrius i reduir-ne la mida. En un intent d'aproximar-nos a un dispositiu ideal amb LEDs de la mínima mida possible, vam decidir incorporar lents per tal de reduir la mida de la matriu de LEDs emprada en el primer prototip.

En emprar una lent podem generar una imatge reduïda del punt de llum del LED directament a la mostra, aproximant les condicions ideals per al mètode. Aquest muntatge va permetre identificar problemes en l'estabilitat del muntatge, i també les dificultats de localitzar un punt concret d'una mostra explorant amb un punt de llum tant petit. Com que això darrer es fa obtenint una imatge de les ombres molt menys magnificada, el nombre limitat de píxels de la càmera SPAD desenvolupada i presentada prèviament ho fa més difícil. No obstant això, gràcies a la flexibilitat en el detector del mètode MNI vam poder substituir la càmera SPAD per una càmera

CMOS convencional amb una resolució molt més elevada, cosa que va facilitar el procés.

Aquest muntatge segueix el mateix concepte que el prototip anterior, però introdueix un objectiu muntat de forma invertida a 15 cm dels LEDs per generar la imatge a la seva distància focal. L'objectiu és de 60 augments amb una obertura de 0.85. El muntatge es pot veure en la figura A.10 a), i un esquemàtic del funcionament en la figura A.10 b).

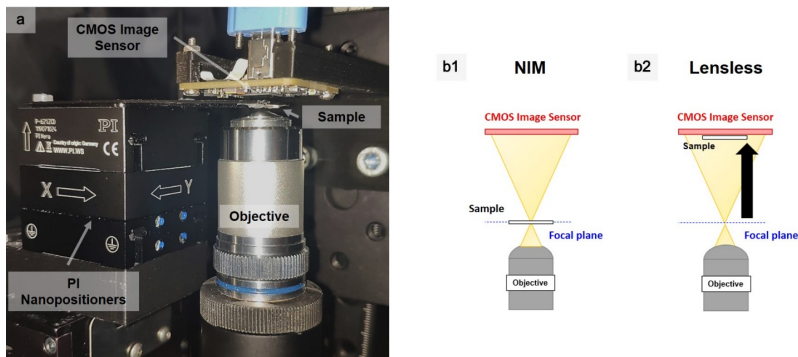


Figura A.10: Muntatge de reducció de punt de llum. a) Fotografia del muntatge experimental. b) Esquemàtic del muntatge i el seu funcionament: la figura b1 mostra el muntatge operant en mode MNI, la b2 en una distribució de microscòpia lensless convencional, amb major camp de visió per tal d'explorar la mostra.

Aquest muntatge de miniaturització del punt de llum ha obtingut les imatges amb més resolució dels presentats, 800 nm, com es mostra en la figura A.11. Les diferents imatges corresponen al mateix objecte, mostrejat amb diferents periodicitats. Els quadres de 800 nm es poden observar correctament a les imatges c) i d), corresponents a periodicitats menors a la meitat de la mida, tal i com és d'esperar per la teoria de mostreig.

No obstant la utilitat d'aquest muntatge que permet aproximar les condicions ideals del microscopi, les imatges formades a través de les lents mai podran ser més petites que el límit d'Abbe, i per tant la super-resolució queda descartada amb aquest muntatge.

La manera d'obtenir imatges amb super-resolució amb muntatges de MNI és mitjançant LEDs més petits que el límit d'Abbe. Per tal de validar si això era possible es va fabricar una matriu de LEDs al límit permès per la tecnologia, formada per dues línies de 32 LEDs de 200 nm emetent a una longitud d'ona de 525 nm.

Amb tot el coneixement acumulat, vam perfeccionar també el muntatge del microscopi. La placa de control de la FPGA utilitzada en muntatges anteriors va ser substituïda per una molt més compacta, que va permetre construir el muntatge de la figura A.12. El muntatge consisteix també en una estructura en "sandwich", amb la mostra sobre la matriu de LEDs i una càmera CMOS convencional just a sobre.

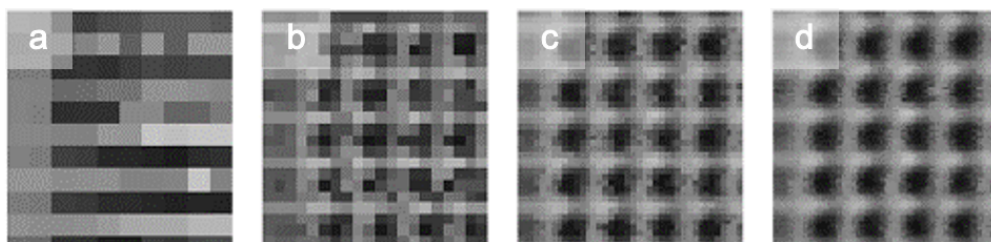


Figura A.11: Imatge MNI de quadres de 800 nm obtingudes amb el muntatge de reducció del punt de llum. Les imatges han estat adquirides amb passos d'escaneig de 750, 400, 200, i 100 nm respectivament per a) b) c) i d).

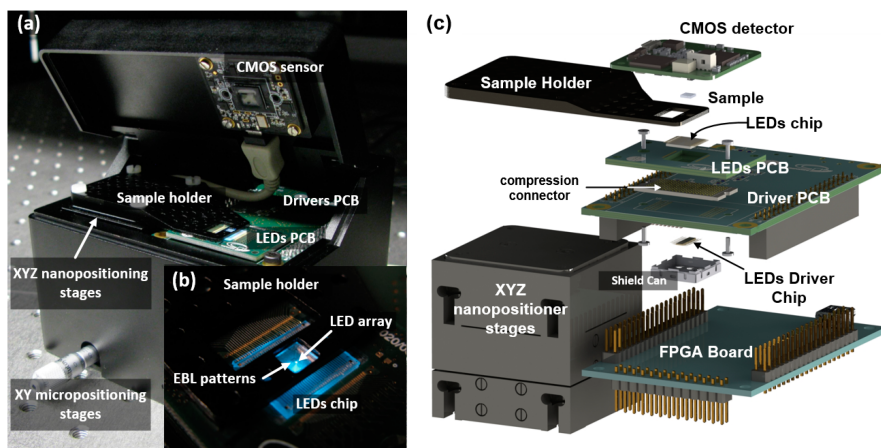


Figura A.12: Muntatge per als LEDs de 200 nm. a) mostra una fotografia del muntatge. b) mostra el detall dels LEDs operant i del posicionament de la mostra. c) mostra un esquemàtic desplegat dels components del microscopi.

Per tal de millorar la precisió en el posicionament, els suports de mostra es van tallar en alumini en comptes d'impressió 3D, així com la carcassa del dispositiu, que té unes dimensions finals de $110 \times 87 \times 74 \text{ mm}^3$.

La màxima resolució obtinguda amb aquesta matriu va ser de $1.56 \mu\text{m}$, molt pitjor de l'esperat i que el muntatge anterior amb lents, tal i com es mostra en la figura A.13, on apareix una part de la mateixa mostra d'alumini tallat amb EBL mostrat anteriorment. Els quadres petits a l'esquerra de l'imatge tenen $1.6 \mu\text{m}$, i la imatge obtinguda escanejant amb el MNI es troba sobre-imposta a la obtinguda amb microscopi òptic.

Entendre la discrepància entre la resolució teòrica i la obtinguda va requerir simulacions extensives dels camps elèctrics en les interfícies entre materials, per part de l'equip de Roma del projecte ChipScope, mostrant un altre cop com el contrast es degrada ràpidament amb la distància entre el punt d'emissió de la llum i la mostra, i a cada interfície de diferents materials.

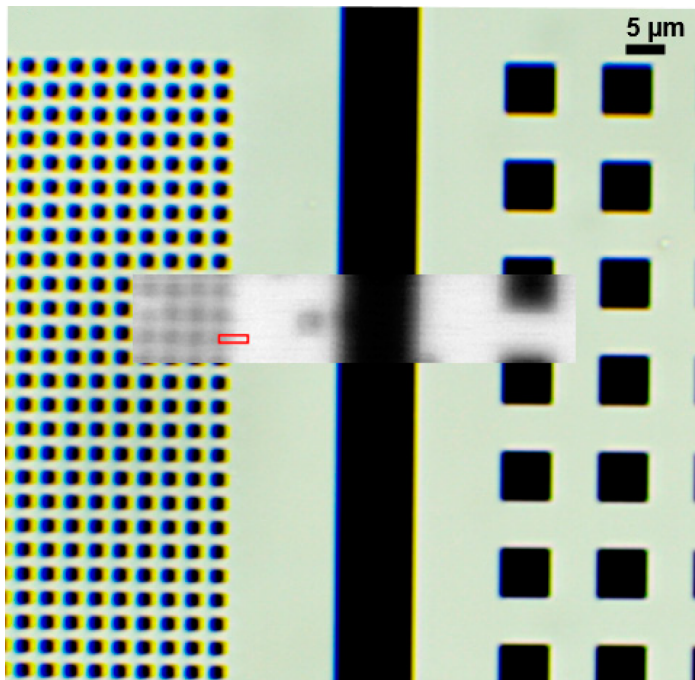


Figura A.13: Imatge amb microscopi òptic de patrons EBL de $1.6\ \mu\text{m}$ (esquerra) i $6.4\ \mu\text{m}$ (dreta), amb la imatge de MNI de la regió corresponent sobre-imposta.

Els prototips desenvolupats en aquesta tesi s'han centrat en obtenir millors resolucions, deixant de banda altres aspectes crítics per un microscopi que tot i així ja s'han detectat. Per exemple, el camp de visió del microscopi, que en un principi es troba limitat a la mida de la matriu de LEDs, es va estendre artificialment afegint microposicionadors d'alta precisió als muntatges, aprofitant que de fet els microscopis ja els havien de tenir de forma obligada per alinear els components. Això ha permès obtenir imatges de molts més píxels del que hagués estat possible només amb les matrius LED.

A.5. Conclusions

En resum, en aquesta tesi s'explica el procés de desenvolupament d'un microscopi sense lents que obté la resolució a partir d'il·luminar la mostra consecutivament amb diferents punts de llum de mida nanomètrica. Aquesta recerca s'ha dut a terme dins el projecte Europeu ChipScope, en el que participen grups de recerca de Braunschweig (Alemanya), Roma i Viena a més de la Universitat de Barcelona.

Hem explicat en aquesta tesi el muntatge dels microscopis, començant pels primers prototips, fent servir com a font de llum les matrius de nanoLEDs desenvolupades per TUBS. Els primers prototips de microscopis incloïen una càmera SPAD dissenyada també en el si d'aquesta tesi. Tot i que els muntatges de microscopis posteriors ja no la utilitzen, aquesta càmera es segueix fent servir al laboratori sobretot en experiments que requereixen cronometrar el temps d'arribada de fotons a la càmera.

Les imatges del primer microscopi tenen un format de forma de 8×8 píxels, ja que aquest és el factor de forma de la matriu de LEDs feta servir per il·luminar la mostra. Amb ella vam validar els principis teòrics, com que el microscopi es regeix per la teoria de mostreig i per tant el poder de resolució és el doble del pitch dels LEDs, $20 \mu\text{m}$ en aquest cas en tenir els LEDs un pitch de $10 \mu\text{m}$.

Per construir els microscopis es va haver de dissenyar tot un sistema de plaques de components electrònics així com els elements de control necessaris: una FPGA central per controlar i configurar els xips integrats fets servir, i per permetre comunicar-se amb l'exterior; també la distribució de les diferents tensions d'alimentació, així com la programació tant a baix nivell (en el processador) com a alt nivell (per mostrar els resultats i oferir un programa de control a l'usuari).

Les dificultats per obtenir LEDs més petits van motivar-nos a buscar maneres alternatives de buscar els límits de la tecnologia. Per un costat, vam fer un muntatge incorporant un objectiu de microscopi invertit per tal de fer més petits els punts de llum dels LEDs utilitzats en el primer microscopi, muntatge amb el que vam obtenir les imatges de més resolució.

Un altre muntatge aprofita els nanoLEDs més petits fabricats per TUBS, de 200 nm , juntament amb la possibilitat de desplaçar-los amb precisions de pocs nanòmetre mitjançant els posicionadors per intentar trencar el límit de resolució d'Abbe

i obtenir imatges amb super-resolució. Finalment, això no va ser possible degut a les distàncies entre el punt d'emissió de la llum i la mostra que introdueixen les pròpies capes necessàries per la fabricació del xip de LEDs o per sustentat i desplaçar la mostra.

El desenvolupament d'aquesta tècnica de microscòpia continua al grup de recerca, investigant com utilitzar matrius de més LEDs per obtenir imatges amb més píxels i de forma més ràpida, així com microscopis encara més compactes que poden ser útils per aplicacions tals com microscopis d'alta resolució de butxaca per especialistes responent a emergències en regions de difícil accés, per exemple.

B

List of Publications

Publications

- [1] Joan Canals et al. “A Novel Approach for a Chip-Sized Scanning Optical Microscope”. In: *Micromachines* 12.5 (May 2021), p. 527. ISSN: 2072-666X. DOI: 10.3390/mi12050527.
- [2] Sergio Moreno et al. “Pursuing the diffraction limit with nano-led scanning transmission optical microscopy”. In: *Sensors* 21.10 (2021). ISSN: 14248220. DOI: 10.3390/s21103305.
- [3] N. Franch et al. “Nano-Illumination Microscopy: a technique based on scanning with an array of individually addressable nanoLEDs”. In: *Optics Express* 28.13 (2020), pp. 19044–19057. ISSN: 1094-4087.
- [4] O. Alonso et al. “An internet of things-based intensity and time-resolved fluorescence reader for point-of-care testing”. In: *Biosensors and Bioelectronics* 154 (2020). ISSN: 18734235. DOI: 10.1016/j.bios.2020.112074.
- [5] Joan Canals et al. “A Point-of-Care Device for Molecular Diagnosis Based on CMOS SPAD Detectors with Integrated Microfluidics”. In: *Sensors (Basel, Switzerland)* 19.3 (Jan. 2019), p. 445. ISSN: 1424-8220. DOI: 10.3390/s19030445.
- [6] A. Dieguez et al. “A Compact Analog-Histogramming SPAD-based CMOS Chip for Time-Resolved Fluorescence”. In: *IEEE Transactions on Biomedical Circuits and Systems* 13.2 (2019), pp. 343–351. ISSN: 1932-4545.
- [7] N. Franch et al. “A low cost fluorescence lifetime measurement system based on SPAD detectors and FPGA processing”. In: *Journal of Instrumentation* 12.02 (Feb. 2017), pp. C02070–C02070. DOI: 10.1088/1748-0221/12/02/C02070.

Conferences

- [1] Sergio Moreno et al. "A nano-illumination microscope with 7 mm² extended field-of-view and resolution below 1 μ m". In: *Optical Diagnostics and Sensing XXI: Toward Point-of-Care Diagnostics*. Ed. by Gerard L. Coté. SPIE, Mar. 2021, p. 7. ISBN: 9781510641372. DOI: 10.1117/12.2578225.
- [2] Anna Vilà et al. "Ultra-compact and large field-of-view nano-illumination light microscope based on an array of organic light-emitting diodes". In: *Photonic Instrumentation Engineering VIII*. Ed. by Yakov Soskind and Lynda E. Busse. SPIE, Mar. 2021, p. 6. ISBN: 9781510642218. DOI: 10.1117/12.2576482.
- [3] J. Canals et al. "Instrumentation for Nano-Illumination Microscopy Based on InGaN/GaN NanoLED Arrays". In: *OSA Optical Sensors and Sensing / Imaging and Applied Optics Congresses 2020, OSA 2020*. 2020.
- [4] J. Canals et al. "A shadow image microscope based on an array of nanoLEDs". In: *SPIE Photonics Europe*. 2020.
- [5] S. Moreno et al. "Nano-Illumination Microscopy as a fast-low-cost chip-sized technique to face pandemics". In: *Biosensors For Pandemics*. 2020.
- [6] V. Moro et al. "A New high-resolution microscopy technique". In: *3rd Global Summit on Nanotechnology, Nanomedicine and Material science*. 2019.
- [7] O. Alonso et al. "Development of an IoT-based point-of-care: an application to malaria testing". In: *International conference on bio-sensing technology (BITE)*. 2019.
- [8] O. Alonso et al. "Readout electronics for LGAD sensors". In: *International Workshop on Semiconductor Pixel Detectors for Particles and Imaging (PIXEL 2016)*. 2016.
- [9] A. Diéguez et al. "Towards a compact lensless superresolution microscope based on nanoarrayed LEDs". In: *6th International conference on biosensing technology*. 2019.
- [10] N. Franch et al. "Towards a super-resolution structured illumination microscope based on an array of nanoLEDs". In: *SPIE Optics + Photonics: SPIE Optical Engineering + Applications 2019*. 2019.
- [11] A. Diéguez et al. "A miniaturized and low-cost sub-nanosecond fluorescence lifetime detector based on an array of CMOS SPAD detectors". In: *28th Anniversary World Congress on Biosensors*. 2018.
- [12] O. Alonso et al. "Diseño y síntesis de sistemas digitales' usando e-learning colaborativo, gamificación y aprendizaje basado en problemas". In: *III Congreso Nacional de Innovación Educativa y Docencia en Red (IN-RED 2017)*. 2017.
- [13] J. Canals et al. "A portable fluorescence lifetime spectroscopy detector for molecular diagnosis". In: *5th International Symposium on Sensor Science*. 2017.

-
- [14] A. Diéguez et al. “A compact lifetime fluorescence detector for clinical diagnosis”. In: *International Conference on Bio-Sensing Technology*. 2017.